IMPLEMENTATION OF FINITE-ELEMENT-WITH-DISCONTIGUOUS-SUPPORT MULTIGROUP METHOD

A Dissertation

by

JIJIE LOU

Submitted to the Office of Graduate and Professional Studies of
Texas A&M University
in partial fulfillment of the requirements for the degree of

DOCTOR OF PHILOSOPHY

Chair of Committee,	Jim E. Morel
Committee Members,	Marvin L. Adams
	Jean Ragusa
	Jean-Luc Guermond
Head of Department,	Michael Nastasi

May 2020

Major Subject: Nuclear Engineering

ABSTRACT

Simulations for obtaining quantities of interest of neutron transport problems need to be accurate and inexpensive. Discretization in energy has been a historical problem due to the resonances. There are two main approaches for discretization of the energy variables: multigroup (MG) and multiband(MB) methods. However, MG method only converges once resonances are resolved, which requires a large number of energy unknowns. The MB method is not applicable to problems with multiple resonant nuclides in different regions because the band structure becomes multiply defined. Finite-Element-with-Discontiguous-Support(FEDS) method was first proposed by Till[1], and is a novel energy discretization method that is able to capture resonance behavior in the reference solutions with a modest unknown count[1, 2]. The goal of this work is to further improve the FEDS method in order to yield better accuracy with fewer degrees of freedom.

Similar to MB method, FEDS has a discontiguous group structure. However instead of defining the group structure in terms of material total cross section, as in the MB method, the discontiguous group structure in FEDS method is determined by using the hierarchical clustering algorithm to solve a minimization problem on multiple reference solutions. In this way, FEDS method can be applied to problems with multiple resonant nuclides in different areas. In addition, FEDS cross sections have a form that can be accommodated by any standard MG solver.

In this work, the following modifications have been made and tested to the FEDS method: introducing the energy-dependent escape cross section from Monte Carlo (MC); introducing the analytical spatial-dependent escape cross section; implementing the FEDS discontiguous group structure in SERPENT for cross sections weighting.

We tested the NJOY-FEDS method with energy- and space-dependent escape cross sections on a 2D UO_2 pin cell problem. We also tested the SERPENT-FEDS method on a 2D UO_2 pin cell problem, a 2x2 MOX and UO_2 pin cell problem, CASL1B and CASL1E problems. The results are compared to that from a standard MG method and a continuous-energy MC method.

It is observed that introducing the energy-dependent escape cross section improves the NJOY-

FEDS performance when the number of energy unknowns is small. Introducing the spatial resolution for cross sections in the fuel dramatically improves the accuracy of NJOY-FEDS results. Implementation the FEDS discontiguous group structure in SERPENT for cross sections weighting greatly reduces the error in spatial absorption and fission rate compared to standard SERPENT-MG method. Overall, SERPENT-FEDS cross sections consistently give the best results for k_{eff} for all the test problems and always give better performance for power distribution.

DEDICATION

I dedicate this dissertation to my dear parents, husband and daughter.

ACKNOWLEDGMENTS

First, I would like to express my deep and warm appreciation to my advisor, Dr. Jim Morel. His expertise, assistance, mentorship, and patience led me through doors and down paths to the research world. I also would like to express special thanks to Profs. Marvin Adams, Jean Ragusa and Jean-Luc Guermond for their valuable time serving as my committee members and their suggestions and guidance for my research.

I am also grateful to the nuclear engineering faculties and staffs at Texas A&M University, who always are helpful and provide me their assistance through my graduate school. I am also thankful to several fellow students and enjoy working and becoming friends with them.

I greatly appreciate the financial support received from Battelle Energy Alliance, LLC, under contract No.166508 and Lawrence Livermore National Laboratory under contract DE-AC52-07NA27344. The latter supported research work unrelated to this dissertation.

I would like to say a heartfelt thank you to my family members, who endlessly support me.

CONTRIBUTORS AND FUNDING SOURCES

Contributors

This work was supported by a dissertation committee consisting of Professors Jim Morel, Marvin Adams and Jean Ragusa of the Department of Nuclear Engineering and Professor Jean-Luc Guermond of the Department of Math.

All work conducted for the dissertation was completed by the student independently.

Funding Sources

This work was sponsored in part by Battelle Energy Alliance, LLC, under contract No.166508.

NOMENCLATURE

MC	Monte Carlo
QOI	Quantities of Interest
PDE	Partial Differential Equation
MG	MultiGroup
MB	MultiBand
FEDS	Finite-Element-with-Discontiguous-Support
DOF	Degree of Freedom
GEM	Generalized Energy Mesh
RRR	Resolved Resonance Region
ER	Equal Radius
EV	Equal Volume
MCD	Multi Chord Length
OCD	One Chord Length
IFBA	Integral Fuel Burnable Absorber
NR	Narrow Resonance
WR	Wide Resonance
IR	Intermediate Resonance
XS	Cross Section
NSC	Nuclear Science Center

TABLE OF CONTENTS

Page

LIST OF FIGURES

FIGURE Page

LIST OF TABLES

TABLE Page

1. INTRODUCTION

The Boltzmann equation for neutron transport can be expressed as follows:

$$\begin{aligned}
&\frac{1}{v}\frac{\partial\psi(t,\boldsymbol{r},\boldsymbol{\Omega},E)}{\partial t}+\boldsymbol{\Omega}\cdot\overrightarrow{\nabla}\psi(t,\boldsymbol{r},\boldsymbol{\Omega},E)+\Sigma_t(\boldsymbol{r},E)\psi(t,\boldsymbol{r},\boldsymbol{\Omega},E)\\
&=\int_0^\infty\int_{4\pi}\Sigma_s(\boldsymbol{r},\boldsymbol{\Omega}'\cdot\boldsymbol{\Omega},E'\to E)\psi(t,\boldsymbol{r},\boldsymbol{\Omega}',E')d\Omega' dE'\\
&\quad+\frac{\chi(\boldsymbol{r},E)}{4\pi}\int_o^\infty\nu\Sigma_f(\boldsymbol{r},E')\phi(t,\boldsymbol{r},E')dE'+q(t,\boldsymbol{r},\boldsymbol{\Omega},E)\,,
\end{aligned}\tag{1.1}$$

where $\psi(t,\boldsymbol{r},\boldsymbol{\Omega},E)$ is the angular flux, $q(t,\boldsymbol{r},\boldsymbol{\Omega},E)$ is the external inhomogeneous source, $\Sigma_s(\boldsymbol{r},E'\to E,\boldsymbol{\Omega}'\cdot\boldsymbol{\Omega})$ is the scattering kernel expressed in terms of the differential macroscopic cross section, $\Sigma_t(\boldsymbol{r},E)$ is the total macroscopic cross section, ν is the average number of neutrons per fission, $\chi(E)$ is the normalized fission spectrum, and $\Sigma_f(\boldsymbol{r},E)$ is the macroscopic fission cross section. This equation involves seven dimensions, three in space, two in direction, one in time and energy, respectively. There are two fundamental ways to solve the above transport equation. One is known as Monte Carlo (MC), which simulates the individual particles and sums up the contribution from each particle to the quantities of interest (QOI). The other is known as the deterministic method, which discretizes the partial differential equation (PDE) and solves the resultant linear equation.

Simulations for obtaining QOIs of neutron transport need to be accurate and inexpensive. Discretization in energy has been a historical problem due to the resonances, where the probability of interacting with a particle changes many orders of magnitude for a very small change in incident energy due to quantum mechanical effects. The total and elastic scattering cross section of U-238 is plotted in Fig.1.1 obtained from JANIS software as an example.

Although these resonances may be well-characterized for the continuous energy domain, resolving them for deterministic schemes requires more memory than is currently affordable. There are two main approaches for discretization of the energy variable in order to generate smaller cross section data sets. One is called the multigroup (MG) method, which averages over continuous en-

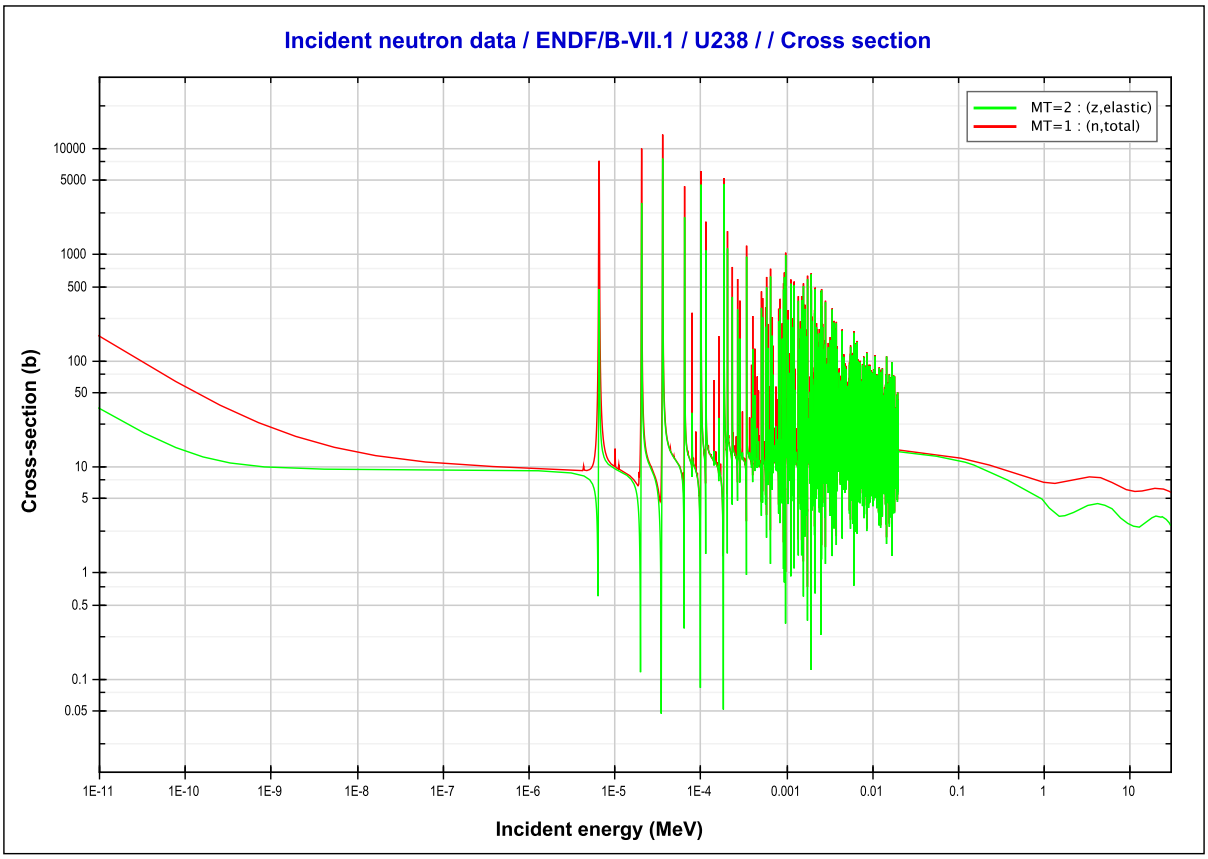

Figure 1.1: Total and elastic scattering cross section of U-238. Plot obtained from JANIS software.

ergy domains called groups, and the other is called the multiband (MB) method, which discretizes in cross section space instead of energy space. However, the MG method only converges once resonances are resolved, which requires a large number of energy unknowns. The MB method is not applicable to problems with different resonant nuclides in different regions because the band structure is multiply defined in each region, and mapping fluxes with different band structure across regions is problematic.

1.1 Multigroup Method

In the MG method, the entire energy domain is divided into G contiguous intervals called groups. There is one angular flux unknown per group, which is the integral of the angular flux over that group. The MG transport equation for group g is obtained by formally integrating the transport equation over group g. Specifically, for the case of isotropic scattering, we obtain:

$$\frac{1}{v_g}\frac{\partial \psi_g}{\partial t} + \mathbf{\Omega}\cdot\overrightarrow{\nabla}\psi_g + \Sigma_{t,g}\psi_g = \frac{1}{4\pi}\sum_{g'=1}^{G}[\Sigma_{s,g'\to g}\phi_{g'}] + \frac{\chi_g}{4\pi}\sum_{g'=1}^{G}[\nu\Sigma_{f,g'}\phi_{g'}] + q_g\,, \tag{1.2}$$

where

$$\psi_g = \int_{E_g}^{E_{g-1}} \psi(t,\boldsymbol{r},\mathbf{\Omega},E)dE\,, \tag{1.3a}$$

$$\phi_g = \int_{E_g}^{E_{g-1}} \phi(t,\boldsymbol{r},E)dE\,, \tag{1.3b}$$

$$\frac{1}{v_g} = \frac{\int_{E_g}^{E_{g-1}} \frac{1}{v}\psi(t,\boldsymbol{r},\mathbf{\Omega},E)dE}{\int_{E_g}^{E_{g-1}} \psi(t,\boldsymbol{r},\mathbf{\Omega},E)dE}\,, \tag{1.3c}$$

$$\Sigma_{t,g} = \frac{\int_{E_g}^{E_{g-1}} \Sigma_t(\boldsymbol{r},E)\psi(t,\boldsymbol{r},\mathbf{\Omega},E)dE}{\int_{E_g}^{E_{g-1}} \psi(t,\boldsymbol{r},\mathbf{\Omega},E)dE}\,, \tag{1.3d}$$

$$\Sigma_{s,g'\to g} = \frac{\int_{E_g}^{E_{g-1}}\int_{E_{g'}}^{E_{g'-1}} \Sigma_s(\boldsymbol{r},E'\to E)\phi(t,\boldsymbol{r},E')dE'dE}{\int_{E_{g'}}^{E_{g'-1}} \phi(t,\boldsymbol{r},E')dE'}\,, \tag{1.3e}$$

$$\chi_g = \int_{E_g}^{E_{g-1}} \chi(E)dE\,, \tag{1.3f}$$

$$\nu\Sigma_{f,g'} = \frac{\int_{E_{g'}}^{E_{g'-1}} \nu\Sigma_f(\boldsymbol{r},E')\phi(t,\boldsymbol{r},E')dE'}{\int_{E_{g'}}^{E_{g'-1}} \phi(t,\boldsymbol{r},E')dE'}\,, \tag{1.3g}$$

$$q_g = \int_{E_g}^{E_{g-1}} q(t,\boldsymbol{r},\mathbf{\Omega},E)dE\,. \tag{1.3h}$$

Note from Eq. (2.14) that all QOIs go from integrals over each group to sums over groups. The process of averaging the variables over energy groups is exact, however, two problems arise simultaneously. The first is that the weighting functions require knowledge of the angular flux

solution, which is unknown. Thus approximate solutions must be used. The second problem is that it gives physical quantities spatial and angular dependencies that they would not otherwise have. Thus approximate solutions, which are piecewise constant in space and isotropic in angle, are used. Moreover, the MG cross sections are also defined by lookup tables, which are built by computations for a variety of escape cross sections and material compositions. In addition, the background cross section, moderator ratios, etc. are also calculated and combined into the lookup table for later interpolation using the actual problem specification.

There are three main approximations associated with MG cross sections. The first comes from the approximate physics in the calculations for building the lookup table, which often uses intermediate resonance (IR) approximations. The second comes from using the shape function calculated from an approximate general geometry and material composition for a more specific problem. The third comes from the fact that MG cross sections in practice, have a crude spatial dependence and have no angular dependence at all. When it comes to preserving the reaction rate, MG can do a much better job for integrated reaction rates. This is largely due to error cancellation. A typical inaccuracy arises due to the difficulty of treating self-shielding in a reactor. Since self-shielding is often averaged over a material, this introduces errors in the spatial shape of the power distribution. The errors associated with MG cross sections from the above three approximations are significant when it comes to the resonance treatment. The resonances dramatically increase the required number of groups to resolve the energy dependences. Also the lack of resonance shielding and interface effects make the general shape function less applicable to specific problems.

1.2 Multiband Method

In the multiband (MB) method, the energy domain is initially divided into G contiguous coarse groups as in the MG method. Then each group g is further subdivided into B discontigous subgroups that span the group g. The B subgroups are defined by B total cross section bands, with each band corresponding to a contiguous range of total cross section values. The number of bands can vary per group, but for each group, the bands are non-overlapping and span the whole range of total cross section values for that group. Let band b in group g be defined by $(\Sigma_{t,g,b-1}, \Sigma_{t,g,b})$, then

E is an energy in subgroup gb if and only if $\Sigma_t(E) \in (\Sigma_{t,g,b-1}, \Sigma_{t,g,b})$. The cross section bands, the subgroups, and the total cross section dependence for group g are illustrated in Fig.1.2.

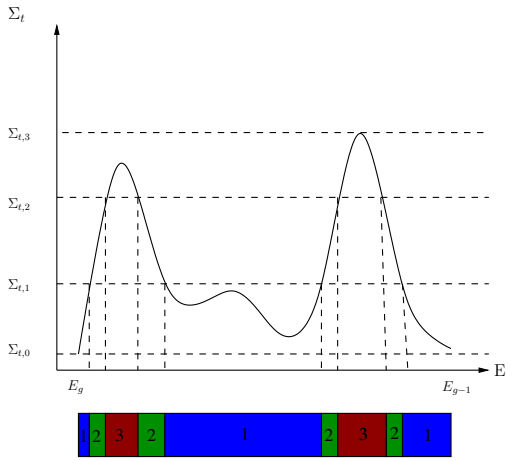

Figure 1.2: Example of MB group structure for group g.

The MB unknown for subgroup gb is the integral of angular flux over subgroup gb:

$$\psi_{gb} = \int_{\Delta E_{gb}} \psi dE \,. \tag{1.4}$$

We obtain the transport equation for ψ_{gb} by integrating Eq. (1.1) over discontiguous subgroup gb. For the case of isotropic scattering, we obtain:

$$\frac{1}{v_{gb}}\frac{\partial \psi_{gb}}{\partial t} + \mathbf{\Omega} \cdot \overrightarrow{\nabla} \psi_{gb} + \Sigma_{t,gb}\psi_{gb} = \frac{1}{4\pi}\sum_{g'=1}^{G}\sum_{b'=1}^{B}[\Sigma_{s,g'b'\to gb}\phi_{g'b'}] + \frac{\chi_{gb}}{4\pi}\sum_{g'=1}^{G}\sum_{b'=1}^{B}[\nu\Sigma_{f,g'b'}\phi_{g'b'}] + q_{gb}\,, \tag{1.5}$$

where

$$\psi_{gb} = \int_{\Delta E_{gb}} \psi(t, \boldsymbol{r}, \boldsymbol{\Omega}, E) dE \,, \tag{1.6a}$$

$$\phi_{gb} = \int_{\Delta E_{gb}} \phi(t, \boldsymbol{r}, E) dE \,, \tag{1.6b}$$

$$\frac{1}{v_{gb}} = \frac{\int_{\Delta E_{gb}} \frac{1}{v} \psi(t, \boldsymbol{r}, \boldsymbol{\Omega}, E) dE}{\int_{\Delta E_{gb}} \psi(t, \boldsymbol{r}, \boldsymbol{\Omega}, E)} \,, \tag{1.6c}$$

$$\Sigma_{t,gb} = \frac{\int_{\Delta E_{gb}} \Sigma_t(\boldsymbol{r}, E) \psi(t, \boldsymbol{r}, \boldsymbol{\Omega}, E) dE}{\int_{\Delta E_{gb}} \psi(t, \boldsymbol{r}, \boldsymbol{\Omega}, E) dE} \,, \tag{1.6d}$$

$$\Sigma_{s,g'b' \to gb} = \frac{\int_{\Delta E_{gb}} \int_{\Delta E_{g'b'}} \Sigma_s(\boldsymbol{r}, E' \to E) \phi(t, \boldsymbol{r}, E') dE' dE}{\int_{\Delta E_{g'b'}} \phi(t, \boldsymbol{r}, E') dE'} \,, \tag{1.6e}$$

$$\chi_{gb} = \int_{\Delta E_{gb}} \chi(E) dE \,, \tag{1.6f}$$

$$\nu\Sigma_{f,g'b'} = \frac{\int_{\Delta E_{gb}} \nu\Sigma_f(\boldsymbol{r}, E') \phi(t, \boldsymbol{r}, E') dE'}{\int_{\Delta E_{g'b'}} \phi(t, \boldsymbol{r}, E') dE'} \,, \tag{1.6g}$$

$$q_{gb} = \int_{\Delta E_{gb}} q(t, \boldsymbol{r}, \boldsymbol{\Omega}, E) dE \,. \tag{1.6h}$$

It can be seen from Eq. (1.5) that the MB equations and MG equations are identical in form, except that cross sections with only downscatter do not numerically lead to a lower diagonal coupling between MB fluxes. So algebraic upscatter can appear even thought there is no physical upscatter. Thus the MB equations can be solved by an MG solver al long as the solver can treat upscatters.

However, the discontiguous subgroup structures defined by the interval of the material total cross section vary over materials, which makes MB method fail to solve the problem with multiple resonant materials [4].

1.3 Finite-Element-with-Discontiguous-Support Multigroup Method

Finite-Element-with-Discontiguous-Support (FEDS) Multi-Group method, which uses finite elements with discontiguous support to treat the energy variable, is a method first proposed by Till [1, 2]. It was shown that FEDS-MG method can yield convergence with fewer degrees of freedom

(DOF) than the MG method and can be applied to multiple resonant materials [2]. Our goal is to further improve FEDS-MG method.

There are several similarities between FEDS-MG and MB methods:

- both of them usually have a contiguous coarse group structure,
- each coarse group contains discontiguous energy subgroups,
- they both introduce algebraic upscatters due to the discontiguous energy mesh,
- their transport equations have the same forms as the MG equations, thus, the cross sections can be directly used in a standard MG solver as long as it effectively treat upscatters.

The differences between FEDS-MG and MB methods are summarized as follows:

- The subgroup structures in the MB method are defined in term of the material total cross section, $\Sigma_t(E)$. Whereas in the FEDS-MG method, the subgroup structures are defined in terms of the approximate solutions, $\phi(E)$.
- In particular, the subgroup structures in the FEDS-MG method are to minimize the variance of the approximate solutions within each subgroup over all the whole problem domain.
- The resulting minimization problem is not practically solvable, thus the clustering algorithm is applied to approximately solve the minimization problem.
- Clustering algorithms are used to determine the discontiguous energy mesh in order to minimize the variance of the approximate solutions within each subgroup over all the resonant materials. In this way, FEDS-MG method can be applied to the problems with multiple resonant nuclides in different areas, and the same energy mesh will be applied to the whole domain.

The workflow for generating FEDS-MG cross sections is summarized as follows:

1. generate the discontiguous group structures:

- obtain problem-relevant approximate solutions from solving infinite-medium slowing-down calculation with an escape cross section,
- determine generalized energy mesh by using clustering algorithm to solve the minimization problem over the approximate solutions.

2. generate the FEDS-MG cross sections:
   - two concepts are introduced to described the discontiguous group structure: contiguous energy subelements and discontiguous energy elements. The contiguous energy subelements span the whole energy domain. Each discontiguous energy element contains several energy subelements, thus the summation of energy elements also span the whole energy domain.
   - generate the cross section on the contiguous energy subelement using standard MG processing system (e.g. NJOY),
   - condense the cross section on the subelement to generate the cross section on the discontiguous energy element.

We have made two main improvements to FEDS:

- in the process of generating the energy mesh, we are trying to improve our approximate solutions, therefore, energy- and space-dependent escape cross sections are introduced and calculated from pin cell calculation in MC , and applied to the calculation of the approximate solutions;
- in the process of generating the cross section, we are trying to improve the weighting functions, therefore, MC code SERPENT [5] is applied to flux weight the FEDS-MG cross sections rather than semi-analytic approximation in standard MG processing system.

The thesis is organized as follows. In section 2, a detailed description of the FEDS-MG method is presented. In section 3, the current study results are listed. In section 4, the conclusion and future work are summarized.

2.1 Generalized Energy Mesh Definition

The discontiguous group structure in the FEDS-MG method is referred to as the generalized energy mesh (GEM). This mesh is illustrated in Fig.2.1.

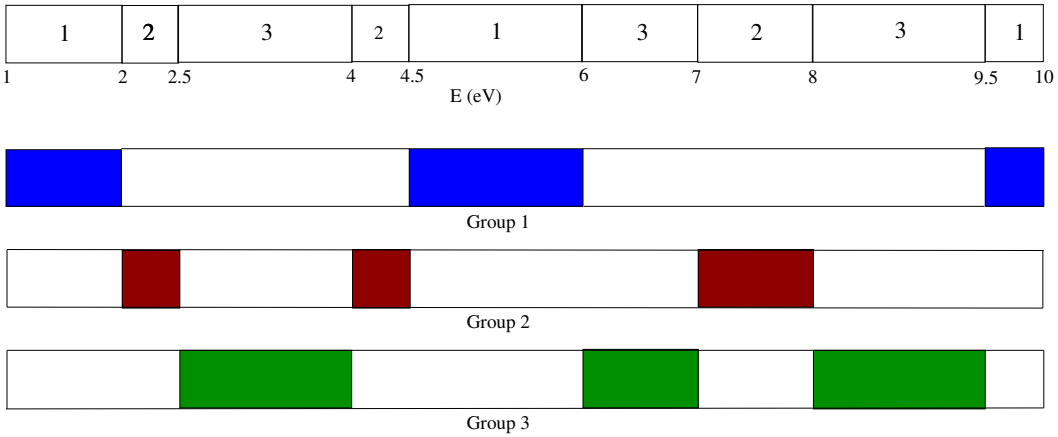

Figure 2.1: Example of generalized energy mesh in the FEDS-MG method.

There are several different components of energy groups used in the FEDS-MG method. In particular, there are contiguous coarse groups, contiguous fine groups, contiguous hyperfine groups and discontiguous groups. The discontiguous groups are the fundamental groups for which we define flux unknowns and cross sections. The various contiguous groups are simply used in the construction of the discontiguous groups as displayed in Fig. 2.2:

- The whole energy domain is divided into C non-overlapping contiguous coarse groups. The coarse groups span the whole energy domain.
- Each coarse group c is spanned by N_c non-overlapping discontiguous groups. Each discontiguous group can only belong to one coarse group.
- There are $N = N_1 + ...N_c + ...N_C$ discontiguous groups spanning the whole energy domain.

- Each discontiguous group e is spanned by n_e non-overlapping contiguous fine groups. Each contiguous fine group can only belong to one discontiguous group.
- There are $G = n_1 + ... + n_e + ... + n_N$ contiguous fine groups spanning the whole energy domain.
- Each contiguous fine group g is spanned by e_g non-overlapping contiguous hyperfine groups. Each hyperfine group can only belong to one contiguous fine group.
- There are $H = e_1 + ...e_g + ... + e_G$ contiguous hyperfine groups spanning the whole energy domain.

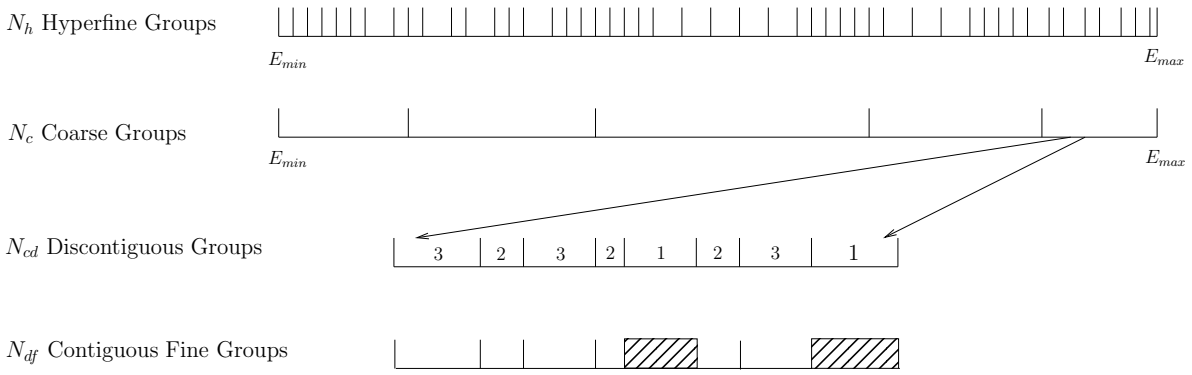

Figure 2.2: Generalized energy mesh in the FEDS-MG method.

We denote the fine group g by the energy domain

$$\Xi_g = (E_{g+1/2}, E_{g-1/2}), \quad g = 1, ..., G\,, \tag{2.1}$$

where $E_{g+1/2} < E_{g-1/2}$.

Each discontiguous group $\mathbb{E}_e$ is defined by a union of fine groups. The indices of these fine groups for discontiguous group e are given by $g_1(e)$, $g_2(e)$, ..., $g_{n_e}(e)$. Thus,

$$\mathbb{E}_e = \Xi_{g_1(e)} \cup \Xi_{g_2(e)} \cup ... \cup \Xi_{g_{n_e}(e)} \tag{2.2}$$

For example, with the energy domain range $[1, 10]$ eV, there is 9 contiguous fine groups and 3 discontiguous groups, as plotted in Fig.2.1.

$$N = 3, \quad G = 9. \tag{2.3}$$

The contiguous fine groups are listed as follows:

$$\begin{aligned}
\Xi_1 &= (9.5, 10) \text{ eV} \\
\Xi_2 &= (8, 9.5) \text{ eV} \\
\Xi_3 &= (7, 8) \text{ eV} \\
\Xi_4 &= (6, 7) \text{ eV} \\
\Xi_5 &= (4.5, 6) \text{ eV} \\
\Xi_6 &= (4, 4.5) \text{ eV} \\
\Xi_7 &= (2.5, 4) \text{ eV} \\
\Xi_8 &= (2, 2.5) \text{ eV} \\
\Xi_9 &= (1, 2) \text{ eV}
\end{aligned} \tag{2.4}$$

Then the discontiguous groups can be described as:

$$\begin{aligned}
&g_1(1) = 1, g_2(1) = 5, g_3(1) = 9, \quad \mathbb{E}_1 = (9.5, 10) \cup (4.5, 6) \cup (1, 2) \text{ eV}, \\
&g_1(2) = 3, g_2(2) = 6, g_3(2) = 8, \quad \mathbb{E}_2 = (7, 8) \cup (4, 4.5) \cup (2, 2.5) \text{ eV}, \\
&g_1(3) = 2, g_2(3) = 4, g_3(3) = 7, \quad \mathbb{E}_3 = (8, 9.5) \cup (6, 7) \cup (2.5, 4) \text{ eV}.
\end{aligned} \tag{2.5}$$

For FEDS-MG method, the number of discontiguous groups is usually much smaller than the number of fine groups, $N \ll G$.

In Fig.2.3, a simple example for the energy mesh in MG, MB and FEDS-MG for 5 unknowns is plotted. First, the energy domain is divided into three coarse group. In coarse group 2, more energy unknowns are needed in order to resolve the mesh. For MG method, consistent index is

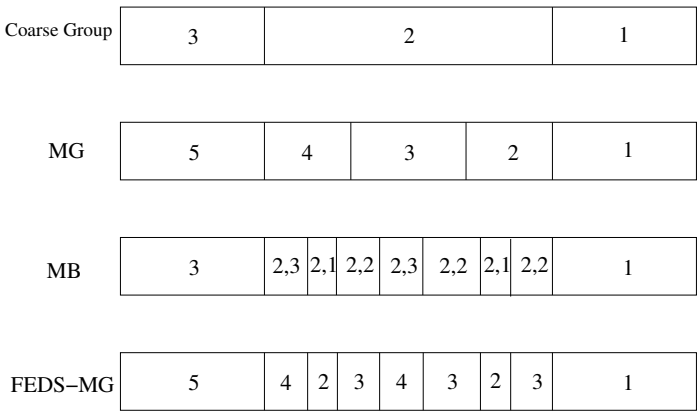

Figure 2.3: Comparison of energy mesh in MG, MB and FEDS-MG methods for 5 unknowns

used for group definition. For MB method, in coarse group 2, three discontiguous subgroups are defined and names as (g, b) as explained in the previous chapter. For FEDS-MG, we adopt the consistent index as used in the MG method.

2.2 Generalized Energy Mesh Determination

The generalized energy mesh is determined to minimize the variations of approximate solutions in each discontiguous group. The approximate solutions are called snapshots and are hyperfine flux solved from an infinite-medium slowing down calculations for each material of interests. There are three components needed for the determination of GEM:

- a hyperfine group structure, which resolves all desired resonances with a minimal number of points, such as $E_{h\pm1/2}, \quad h = 1, ..., H$ ($\mathbb{O}$ (10,000)). The generation of hyperfine group structure is documented in Appendix 2.1.

- P representative high-resolution snapshots of the solution on the hyperfine structure are obtained, $\phi_{p,h}$, $p = 1, ..., P$. The details of constructing approximate solutions are documented in Sec. 2.2.1.

- a final number of discontiguous groups, N.

2.2.1 Snapshot Generation

The snapshots are approximate solution from an infinite-medium equivalent, fixed source problem.

$$\big[\Sigma_e + \Sigma_t(E)\big]\phi(E) = q(E)\,. \tag{2.6}$$

For a thermal system, as explained in Appendix 1, the source is approximated by a watt fission spectrum in the high energy, $1/E$ in the resonance energy range and Maxwellian spectrum for thermal energy range.

$$\begin{aligned} q(E) = &[\frac{1}{E_{\text{thermal}}} + \frac{\chi(E_{\text{thermal}})}{E_{\text{fast}}\chi(E_{\text{fast}})}]\frac{M(E)}{M(E_{\text{thermal}})}(\text{if } E < E_{\text{thermal}}) \\ &\sum_{z_i>90}[\frac{N_i}{1-\alpha_i}\int_E^{E/\alpha_i} dE'\frac{\phi(E')\sigma_{s,i}(E')}{E'}] + [\frac{1}{E} + \frac{\chi(E)}{E_{\text{fast}}\chi(E_{\text{fast}})}](\text{if } E_{\text{thermal}} \le E \le E_{\text{high}}) \\ &[\frac{1}{E_{\text{high}}} + \frac{\chi(E)}{E_{\text{fast}}\chi(E_{\text{fast}})}](\text{if } E_{\text{high}} \le E) \end{aligned} \tag{2.7}$$

where $\alpha_i = [(A_i - 1)/(A_i + 1)]^2$.

2.2.2 Minimization Problem

2.2.2.1 Hierarchical Agglomerative Clustering Definition

The hierarchical agglomerative clustering is used for determination of GEM. The basic algorithm is plotted in Fig. 2.4 and described as follows:

- Start with each point in a cluster of its own.
- Iterate until there is only one cluster:
  - look for the closest pair of clusters
  - merge them to form a new cluster
- Return tree of cluster-mergers.

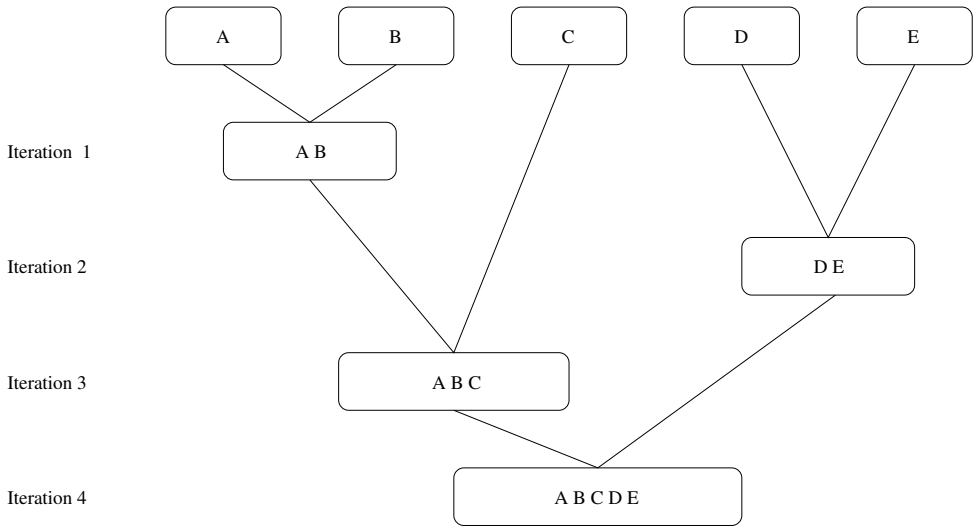

Figure 2.4: Example for hierarchical agglomerative clustering.

The hierarchical agglomerative clustering generates a nested partitioning structure, where in each level up two clusters are merged for the lower partition. In order to define how close two clusters are, Ward's method is employed. In Ward's method, the distance between two clusters, A and B, is calculated as the the sum of increased squares in case of merging two:

$$\Delta(A,B) = \sum_{i \in A \cup B} ||\overrightarrow{x}_i - \overrightarrow{m}_{A \cup B}||^2 - \sum_{i \in A} ||\overrightarrow{x}_i - \overrightarrow{m}_A||^2 - \sum_{i \in B} ||\overrightarrow{x}_i - \overrightarrow{m}_B||^2 \tag{2.8}$$

where $\overrightarrow{m}_j$ is the center of cluster j and Δ is the merging cost of combing clusters A and B.

2.2.2.2 Mapping Minimization Problem to Clustering

The energy mesh is determined by minimizing the variance between P snapshots and those within N disontiguous group. Minimizing the variance encounters a wide range of flux magnitudes, the normalization of the data points is described as follows:

- In the generation of snapshot, we used $q(E)$ as the source. Here we define $f(E) \simeq q(E)$ as:

$$\begin{aligned} f(E) = & [\frac{1}{E_{\text{thermal}}} + \frac{\chi(E_{\text{thermal}})}{E_{\text{fast}}\chi(E_{\text{fast}})}]\frac{M(E)}{M(E_{\text{thermal}})}(\text{if } E < E_{\text{thermal}}) \\ & + [\frac{1}{E} + \frac{\chi(E)}{E_{\text{fast}}\chi(E_{\text{fast}})}](\text{if } E_{\text{thermal}} \leq E \leq E_{\text{high}}) \\ & [\frac{1}{E_{\text{high}}} + \frac{\chi(E)}{E_{\text{fast}}\chi(E_{\text{fast}})}](\text{if } E_{\text{high}} \leq E)\,. \end{aligned} \tag{2.9}$$

  Then,

$$\phi_{p,h}^{\text{normalized 1}} = \frac{\phi_{p,h}}{f_{p,h}}\,. \tag{2.10}$$

- Instead of treating $\phi_{p,h}^{\text{normalized}}$ as an average over group h, we treat it as a point wise value, then

$$\phi_{p,h}^{\text{normalized 2}} = \frac{\phi_{p,h}^{\text{normalized 1}}}{\Delta E_h} \tag{2.11}$$

- We further normalize the variables in order to make their median datas with a value of 0.

$$\log_{10}\phi_{p,h}^{\text{normalized 3}} = \log_{10}\phi_{p,h}^{\text{normalized 2}} - \log_{10}\{\phi_{p,\text{median}}^{\text{normalized 2}}\} \tag{2.12}$$

- In order to reduce the magnitude of the variables, we apply the operator of $\log_{10}$ to the variables, and name as observation[1] $\overrightarrow{O}_h$. The p element of the vector $\overrightarrow{O}_h$ is:

$$\overrightarrow{O}_{h,p} = w_p \log_{10}\phi_{p,h}^{\text{normalized 3}}\,, \tag{2.13}$$

  where w_p is the weight of snapshot p.

Now, the minimization problem is simplified as clustering H vectors into N clusters.

2.2.3 Hierarchical Energy Mesh

Coarse group structures are also included in the GEM generation, making it as a hierarchical energy mesh method. The above level is to divide the whole energy domain into coarse groups.

The below level is to divide each course group into discontiguous groups. There are three main advantages associated with this nested partitioning. First, it is easier to check the reaction rate edits on certain energy range with coarse group structures. Second, it's easier to treat the termed explicitly depending on energy, such as $1/v$ streaming term. Third, it helps to bound the effective upscattering, which is the upper-diagonal terms in the scattering matrix and produced by using the discontiguous energy ranges. Suppose a MG scattering matrix, which is lower-triangular, it will be block low-triangular in FEDS-MG method. With coarse group, the upscattering block is bounded by the energy range of each coarse group.

There are two problems associate with the coarse groups: one is to determine the group boundaries, and the other is determine how many discontiguous groups to be used in each coarse group. The number of discontiguous groups in each coarse group should be equal or larger than 1 and be proportional to the relative standard deviation in the coarse group. The detailed process is documented in Appendix B.2.

2.3 Derivation of FEDS-MG Transport Equation

The FEDS-MG transport equation for discontiguous group e is obtained by formally integrating the transport equation over discontiguous group $\mathbb{E}_e$. Specifically, for the case of isotropic scattering, we obtain:

$$\frac{1}{v_e}\frac{\partial \psi_e}{\partial t} + \mathbf{\Omega}\cdot\overrightarrow{\nabla}\psi_e + \Sigma_{t,e}\psi_e = \frac{1}{4\pi}\sum_{e'=1}^{N_e}[\Sigma_{s,e'\to e}\phi_{e'}] + \frac{\chi_e}{4\pi}\sum_{e'=1}^{N_e}[\nu\Sigma_{f,e'}\phi_{e'}] + q_e\,, \tag{2.14}$$

where

$$\psi_e = \int_{\mathbb{E}_e} \psi(t, \boldsymbol{r}, \boldsymbol{\Omega}, E) dE \,, \tag{2.15a}$$

$$\phi_e = \int_{\mathbb{E}_e} \phi(t, \boldsymbol{r}, E) dE \,, \tag{2.15b}$$

$$\frac{1}{v_e} = \frac{\int_{\mathbb{E}_e} \frac{1}{v} \psi(t, \boldsymbol{r}, \boldsymbol{\Omega}, E) dE}{\int_{\mathbb{E}_e} \psi(t, \boldsymbol{r}, \boldsymbol{\Omega}, E) dE} \,, \tag{2.15c}$$

$$\Sigma_{t,e} = \frac{\int_{\mathbb{E}_e} \Sigma_t(\boldsymbol{r}, E) \psi(t, \boldsymbol{r}, \boldsymbol{\Omega}, E) dE}{\int_{\mathbb{E}_e} \psi(t, \boldsymbol{r}, \boldsymbol{\Omega}, E) dE} \,, \tag{2.15d}$$

$$\Sigma_{s,e' \to e} = \frac{\int_{\mathbb{E}_e} \int_{\mathbb{E}_{e'}} \Sigma_s(\boldsymbol{r}, E' \to E) \phi(t, \boldsymbol{r}, E') dE' dE}{\int_{\mathbb{E}_{e'}} \phi(t, \boldsymbol{r}, E') dE'} \,, \tag{2.15e}$$

$$\chi_g = \int_{\mathbb{E}_e} \chi(E) dE \,, \tag{2.15f}$$

$$\nu\Sigma_{f,g'} = \frac{\int_{\mathbb{E}_{e'}} \nu\Sigma_f(\boldsymbol{r}, E') \phi(t, \boldsymbol{r}, E') dE'}{\int_{\mathbb{E}_{e'}} \phi(t, \boldsymbol{r}, E') dE'} \,, \tag{2.15g}$$

$$q_g = \int_{\mathbb{E}_e} q(t, \boldsymbol{r}, \boldsymbol{\Omega}, E) dE \,. \tag{2.15h}$$

2.4 FEDS-MG Cross Section Generation

There are two main separate steps for generating FEDS-MG cross sections:

- Generate the generalized energy mesh (GEM):

    1. Generate PENDF tapes for all nuclides in the material, where all resonance parameters is converted into point-wise cross sections fitting for linear interpolation with certain accuracy. A hyperfine group structure is generated to resolve the resonances of all the relevant nuclides based on the energy grid from PENDF tapes.
    2. Select the material compositions and temperatures, which are either actual material compositions or approximate compositions that will occur in the later problem, such as a depletion calculation.
    3. Perform an infinite-medium slowing-down with analytical escape cross section calculation on the hyperfine group structure for each selected material to construct the library

of snapshots.

4. Determine the number of discontinuous groups in each coarse group.
5. Apply the hierarchical clustering algorithm to the library of snapshots to generate the energy mesh in each coarse group.

- Generate cross sections on GEM. There are two different ways for FEDS-MG cross section generation, one is to use the standard MG method and the other is use to use MC method.
  - Standard MG method:
    1. Generate standard MG cross sections and transfer matrix on the continuous energy subelements using NJOY or other standard MG cross section generation codes. One thing to noticed is that the basis function used in NOJY is approximated by containing a thermal Maxwellian at low energies, a $1/E$ function at intermediate energies and a fission spectrum at high energies. This approximate basis function has no information about resonances.
    2. Generate FEDS-MG cross section by combing cross sections on the subelements, where the basis functions are generated from an infinite-medium slowing-down with analytical escape cross section calculation.
  - MC method: Serpent, as a Monte Carlo particle transport code, can be used to generate few group constants. Here, the GME is applied in SERPENT for FEDS-MG cross section, in which a more accurate basis function is obtained.

3. COMPUTATIONAL RESULTS

3.1 Simple 2D Pin Cell Calculation

3.1.1 Problem Description

We did calculations using multiple versions of NJOY-FEDS cross section in comparison to the results from the continuous-energy MC method using the same ENDF/B-VII.1 library data. A set of runs are also performed using SERPENT-MG cross section with SHEM-361[6] group boundaries and FEDS GEM, respectively. We solved a k-eigenvalue problem for a 2D infinite lattice of a pin cell made of UO_2 fuel: 10.29769 g/cm^3, 96% U-238, 4% U-235, and H_2O moderator: 0.740582 g/cm^3 at room temperature. The radius of fuel is 0.39218 cm, the length of pitch is 1.25984 cm. Reflective boundary conditions are applied.

The fuel region is further divided into 4 regions (50%, 30%, 15%, 5% of volume) for QOIs comparisons. A resolution study in space/angle/scattering moment was performed in PDT to achieve a difference in k_{eff} and total absorption rate less than 1 pcm. P_3 scattering is used. The mesh is plotted in Fig. 3.1. There is 4, 2, 2, 3, 8 number of cells in radial direction and 12, 12, 16, 32, 32 number of cells in azimuthal direction. Gauss-Chebyshev product quadrature is used for angular quadrature with 16 polar angles and 32 azimuthal angles.

We created the energy mesh hierarchically. We first divided the whole energy range into 12 coarse group, listed in Table 3.1[3]. For the energy range outside the reserved resonance range (RRR), we applied the SHEM-361 group boundaries. Inside the RRR, from coarse group 3-10, we applied the FEDS method to determine the discontiguous group structure. We chose our 12 coarse groups to be hierarchical to the SHEM-361 group boundaries.

This problem was originally tested in previous work [3] using NJOY-FEDS cross sections, denoted as 1-FEDS-X where $X = 166, 195, 244, 361,$ or 417. The previous GEM was generated used two spectra, both for fuel pin of UO_2, one with U-238 only and another with 4% U-235. The results using the exact problem material composition for snapshot generation are listed, denoted as

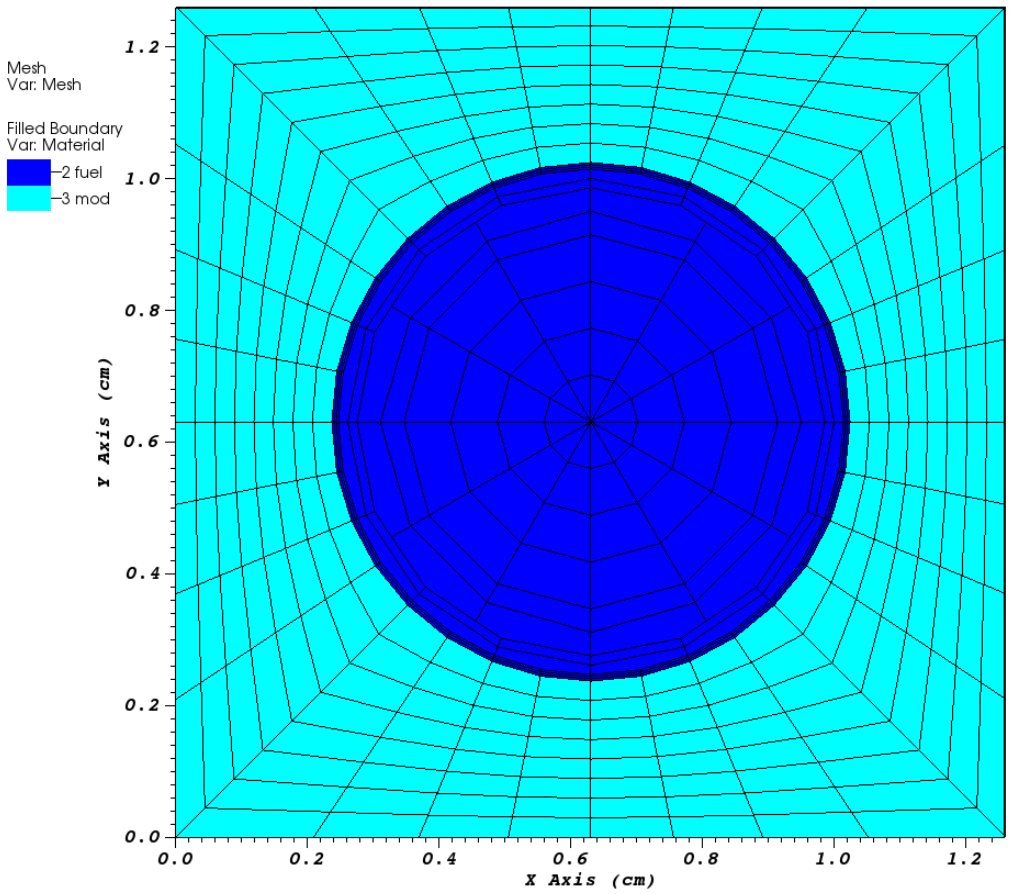

Figure 3.1: PDT mesh for 2D pin cell problem.

Table 3.1: Coarse group structure[3].

Coarse Group	Upper Energy (eV)	Uses Discontiguous Group Structure
I	2.00000×10^{7}	No
II	1.40000×10^{5}	No
III	2.26994×10^{4}	Yes
IV	9.11881×10^{3}	Yes
V	2.08410×10^{3}	Yes
VI	5.39204×10^{2}	Yes
VII	1.54176×10^{2}	Yes
VIII	5.17847×10^{1}	Yes
IX	2.78852×10^{1}	Yes
X	9.50002×10^{0}	Yes
XI	4.21983×10^{0}	No
XII	6.24999×10^{-1}	No

Table 3.2: Errors in k_{eff} for different types of cross section data (NJOY-FEDS, SERPENT-SHEM, NJOY-SHEM) for 2D pin cell problem.

Method	Unknowns (RRR)	K_{eff}	E_{pcm}	Efficiency $\frac{1}{\lvert\text{Error}\rvert \times \text{DOF}}$
1-FEDS-166	30	1.47075	417±1	8.0
1-FEDS-195	59	1.46837	254±1	6.7
1-FEDS-244	108	1.46680	147±1	6.3
1-FEDS-361	225	1.46545	55±1	8.1
1-FEDS-417	281	1.46529	44±1	8.1
2-FEDS-166	30	1.46951	332±1	10.0
2-FEDS-195	59	1.46656	130±1	13.0
2-FEDS-244	108	1.46630	112±1	8.2
2-FEDS-361	225	1.46564	68±1	6.6
2-FEDS-417	281	1.46537	49±1	7.3
NJOY-SHEM-166	30	1.46875	280±1	11.9
NJOY-SHEM-244	108	1.46875	207±1	4.5
NJOY-SHEM-361	225	1.46410	-38±1	11.8
SERPENT-SHEM-166	30	1.46057	-279±1	11.9
SERPENT-SHEM-244	108	1.46250	-147±1	6.3
SERPENT-SHEM-361	225	1.46366	-68±1	6.6

2-FEDS-X where $X = 166, 195, 244, 361,$ or 417. For comparison, the results using NJOY-SHEM cross sections and SERPENT-SHEM cross sections are also included.

The errors in k_{eff} decrease with increased number of groups in resolved resonance region (RRR) for each set of cross sections. It is also observed that using the spectra with exact problem material composition further reduces the error in NJOY-FEDS method, especially for the cases of 166 and 195 groups. It reduces approximately 85 and 124 pcm in the error for 166 and 195 groups, respectively. This indicates that more accurate reference solutions can improve the discontinuous group structure to better capture the resonance behavior. The NJOY-SHEM method gives the best result for the cases of 166 and 361 groups, which is perhaps expected since the SHEM group structure is highly hand-tuned. However, there is little difference between the NJOY-FEDS and NJOY-SHEM methods at the highest resolution. For SERPENT-SHEM cross sections, it only

gives better results than NJOY-FEDS method in the case of 166 groups.

The unit pcm is also used in the comparison for reaction rate errors as defined as :

$$\text{Error}_c = \frac{\text{Tally}_c^{\text{PDT}} - \text{Tally}_c^{\text{MCNP}}}{\sum_c \text{Tally}_c^{\text{MCNP}}} 10^5 \quad \text{pcm} \tag{3.1}$$

where c is the notation for coarse group. L1 Error is defined to avoid error cancellation as:

$$\text{L1 Error}_c = \frac{|\text{Tally}_c^{\text{PDT}} - \text{Tally}_c^{\text{MCNP}}|}{\sum_c \text{Tally}_c^{\text{MCNP}}} 10^5 \quad \text{pcm} \tag{3.2}$$

The errors in absorption and fission rates in 50%, 30%, 15%, 5% fuel regions for different types of cross sections for 166 groups are plotted in Figs.3.2-3.3, respectively. The errors in in absorption and fission rates for the whole fuel for different types of cross sections for 166 groups are plotted in Figs.3.4, and 3.5, respectively. Errors in absorption rates and fission rate for different types of cross section data for different unknown numbers are summarized in Tables 3.3-3.4, respectively . L1 errors in absorption rates and fission rates for different types of cross section data for different unknown numbers are summarized in Tables 3.5-3.6. Both the errors and L1 errors in reaction rates decrease with increased number of unknowns in RRR for each set of cross sections as observed in the results of k_{eff}. While it's not obvious from the comparison of errors in reaction rates for 1-FEDS and 2-FEDS methods, there is consistent reduction in L1 errors for 166 and 195 groups when using more accurate snapshots in NJOY-FEDS methods. It is also noticed that the absorption errors plotted in Fig.3.2 using SERPENT-SHEM and NJOY-SHEM show similar behavior: in the 50%, 30%, 15% fuel regions, the maximum coarse group absorption errors reach about 1000 pcm, and in the outer 5% fuel region, the maximum coarse group error can be a magnitude larger than that from NJOY-FEDS methods. The first largest resonance of U-238 occurs at energy 6.67 eV, which is among the energy range $[4.21983, 9.50002]$ eV corresponding to the maximum coarse group error. Although SERPENT-SHEM method uses a more accurate spectrum for cross section weighting while NJOY-SHEM uses an approximate solution with NR approximation, both of SERPENT-SHEM and NJOY-SHEM fail to resolve the resonance in RRR. Hence, the low errors for k_{eff} for

Table 3.3: Errors in integrated absorption rates for different types of cross section data (NJOY-FEDS, SERPENT-SHEM, NJOY-SHEM) for 2D pin cell problem.

Method	50% fuel	30% fuel	15% fuel	5% fuel	fuel
1-FEDS-166	255	-35	-174	-1684	-34
1-FEDS-195	113	-14	-126	-676	-18
1-FEDS-244	69	-10	-110	-314	-10
1-FEDS-361	41	-11	-66	-142	-5
1-FEDS-417	41	-7	-69	-137	-4
2-FEDS-166	279	33	-356	-1587	-26
2-FEDS-195	140	-20	-177	-625	-12
2-FEDS-244	81	-17	-128	-309	-9
2-FEDS-361	45	-10	-76	-153	-5
2-FEDS-417	40	-7	-65	-138	-4
SERPENT-SHEM-166	2755	1419	-2971	-20161	-138
SERPENT-SHEM-244	1360	732	-1423	-11392	-149
SERPENT-SHEM-361	533	-94	-979	-3141	-152
NJOY-SHEM-166	2833	1590	-2701	-19864	14
NJOY-SHEM-244	1487	893	-1166	-11080	22
NJOY-SHEM-361	734	95	-813	-2998	36

SERPENT-SHEM and NJOY-SHEM methods are due to the error cancellation.

3.1.2 Adding Energy-Dependent Escape Cross Sections

Equivalence theory treats leakage as an absorption term, then the escape cross section, $\Sigma_e(E)$, is defined as the ratio of the partial outgoing current to the total flux within a region:

$$\Sigma_e(E) = \frac{\int_{\partial D} dS \int_{\mathbf{\Omega}\cdot\boldsymbol{n}\geq 0} d\Omega |\mathbf{\Omega}\cdot\boldsymbol{n}| \psi(\boldsymbol{r},\mathbf{\Omega},E)}{\int_D dV \int_{4\pi} d\Omega \psi(\boldsymbol{r},\mathbf{\Omega},E)} \tag{3.3}$$

Then for steady state problem and lumping together all the local source into $q(\boldsymbol{r},\mathbf{\Omega},E)$, the

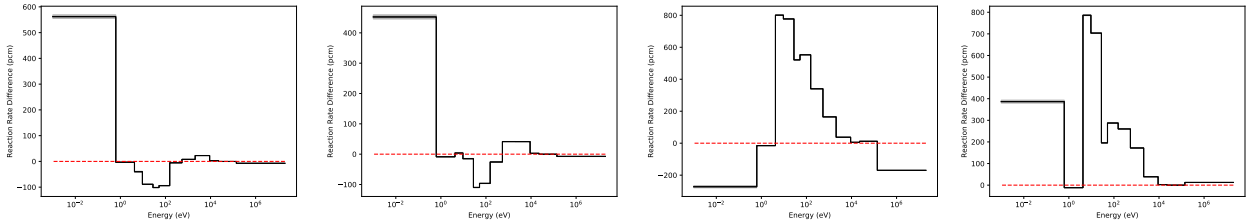

(a) 1-FEDS-50% fuel (b) 2-FEDS-50% fuel (c) SERPENT-SHEM-50% fuel (d) NJOY-SHEM-50% fuel

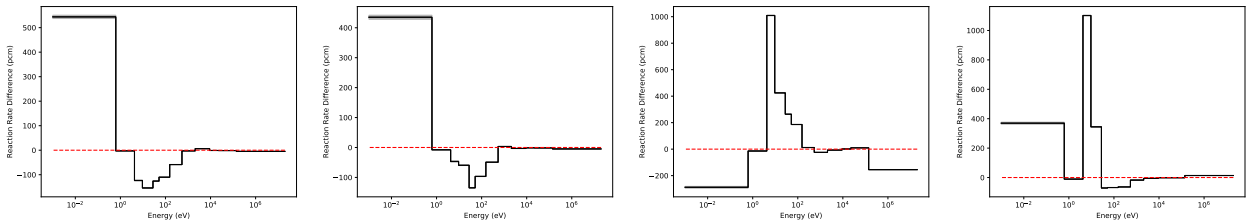

(e) 1-FEDS-30% fuel (f) 2-FEDS-30% fuel (g) SERPENT-SHEM-30% fuel (h) NJOY-SHEM-30% fuel

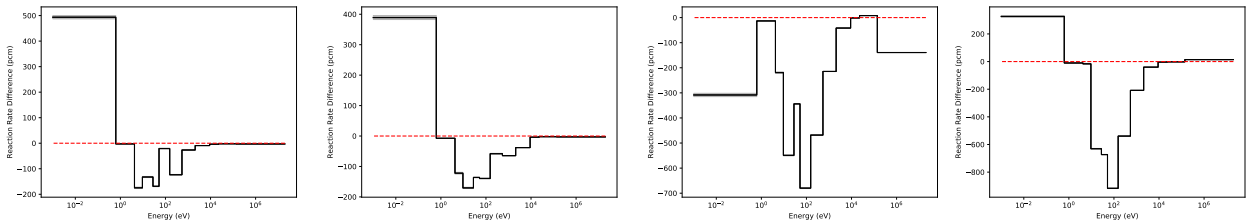

(i) 1-FEDS-15% fuel (j) 2-FEDS-15% fuel (k) SERPENT-SHEM-15% fuel (l) NJOY-SHEM-15% fuel

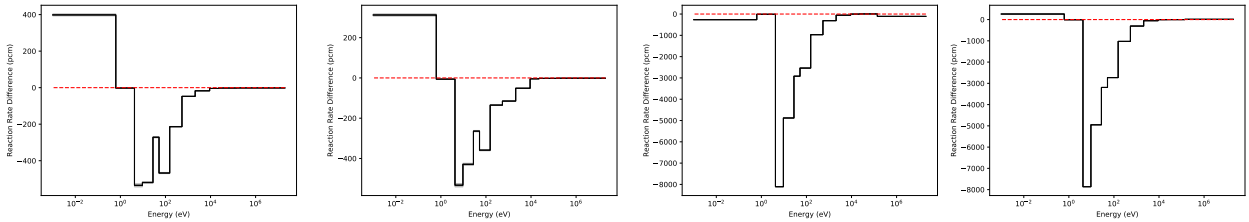

(m) 1-FEDS-5% fuel (n) 2-FEDS-5% fuel (o) SERPENT-SHEM-5% fuel (p) NJOY-SHEM-5% fuel

Figure 3.2: Absorption errors in multiple regions of the fuel between MCNP and PDT for different types of cross section data (1-FEDS-166, 2-FEDS-166, SERPENT-SHEM-166, NJOY-SHEM-166) for 2D pin cell problem (pcm in 95% condifence). Columns have the same cross sections. Rows have the same QOIs.

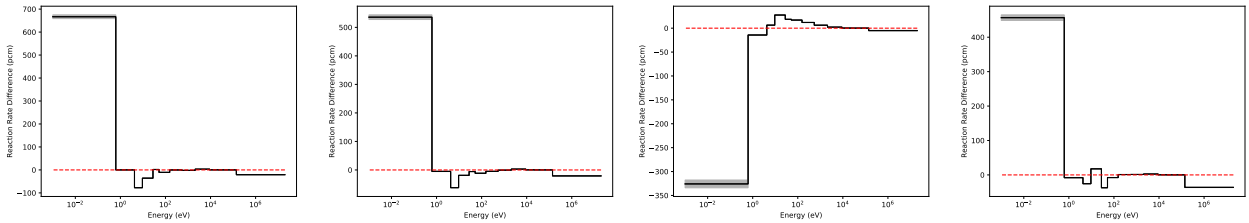

(a) 1-FEDS-50% fuel (b) 2-FEDS-50% fuel (c) SERPENT-SHEM-50% fuel (d) NJOY-SHEM-50% fuel

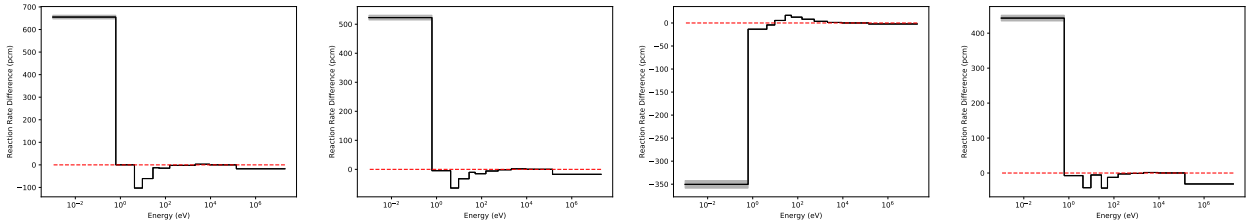

(e) 1-FEDS-30% fuel (f) 2-FEDS-30% fuel (g) SERPENT-SHEM-30% fuel (h) NJOY-SHEM-30% fuel

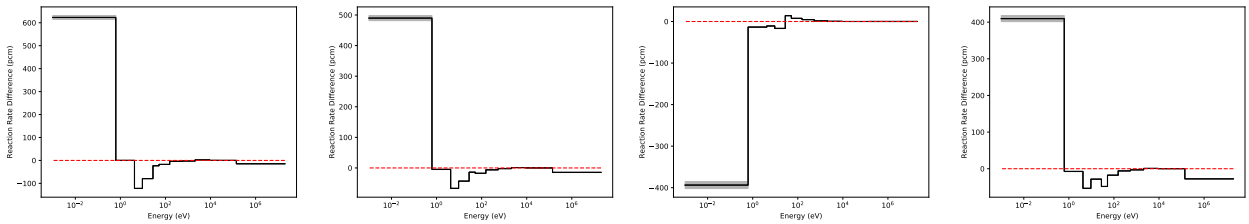

(i) 1-FEDS-15% fuel (j) 2-FEDS-15% fuel (k) SERPENT-SHEM-15% fuel (l) NJOY-SHEM-15% fuel

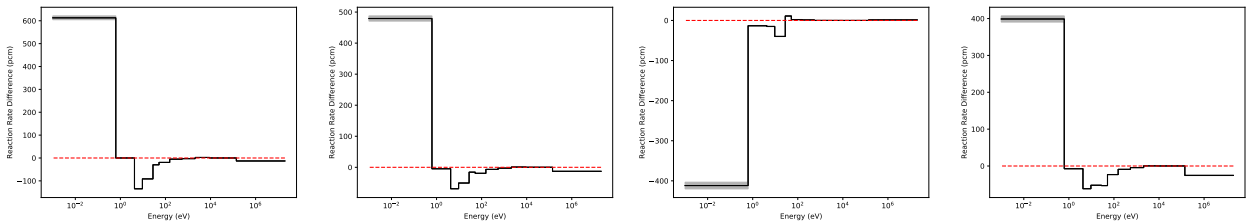

(m) 1-FEDS-5% fuel (n) 2-FEDS-5% fuel (o) SERPENT-SHEM-5% fuel (p) NJOY-SHEM-5% fuel

Figure 3.3: Fission errors in in multiple regions of the fuel between MCNP and PDT for different types of cross section data (1-FEDS-166, 2-FEDS-166, SERPENT-SHEM-166, NJOY-SHEM-166) for 2D pin cell problem (pcm in 95% condifence). Columns have the same cross sections. Rows have the same QOIs.

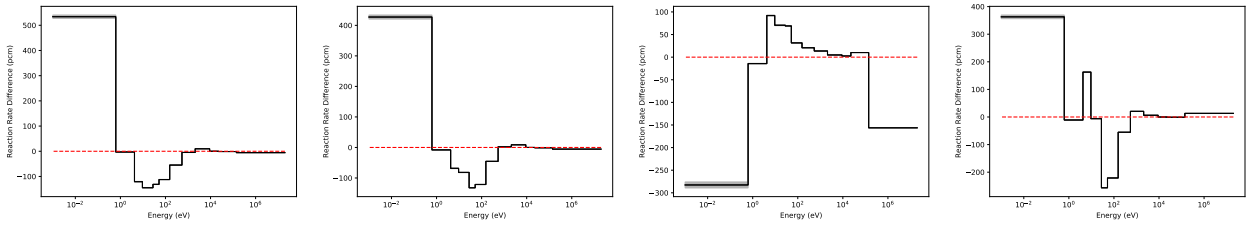

(a) 1-FEDS fuel (b) 2-FEDS fuel (c) SERPENT-SHEM fuel (d) NJOY-SHEM fuel

Figure 3.4: Absorption errors in the whole fuel between MCNP and PDT for different types of cross section data (1-FEDS-166, 2-FEDS-166, SERPENT-SHEM-166, NJOY-SHEM-166) for 2D pin cell problem (pcm in 95% condifence).

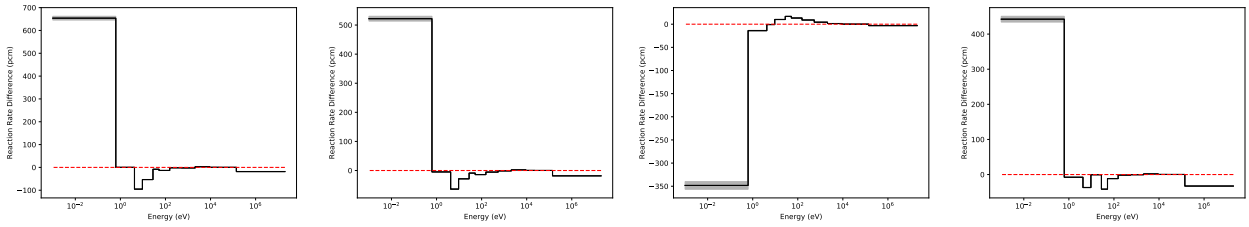

(a) 1-FEDS fuel (b) 2-FEDS fuel (c) SERPENT-SHEM fuel (d) NJOY-SHEM fuel

Figure 3.5: Fission errors in the whole fuel between MCNP and PDT for different types of cross section data (1-FEDS-166, 2-FEDS-166, SERPENT-SHEM-166, NJOY-SHEM-166) for 2D pin cell problem (pcm in 95% condifence).

Table 3.4: Errors in integrated fission rates for different types of cross section data (NJOY-FEDS, SERPENT-SHEM, NJOY-SHEM) for 2D pin cell problem.

Method	50% fuel	30% fuel	15% fuel	5% fuel	fuel
1-FEDS-166	526	446	363	320	465
1-FEDS-195	341	291	230	201	301
1-FEDS-244	221	188	140	119	193
1-FEDS-361	120	98	58	44	100
1-FEDS-417	107	88	50	36	89
2-FEDS-166	410	374	323	299	380
2-FEDS-195	201	172	127	111	176
2-FEDS-244	172	159	126	117	158
2-FEDS-361	126	114	82	74	113
2-FEDS-417	108	95	62	52	94
SERPENT-SHEM-166	-255	-323	-406	-464	-311
SERPENT-SHEM-244	-133	-183	-250	-294	-175
SERPENT-SHEM-361	-57	-100	-159	-188	-93
NJOY-SHEM-166	365	300	219	163	312
NJOY-SHEM-244	274	231	171	134	237
NJOY-SHEM-361	22	-12	-62	-84	-7

Table 3.5: L1 errors in absorption rates for different types of cross section data (NJOY-FEDS, SERPENT-SHEM, NJOY-SHEM) for 2D pin cell problem.

Method	50% fuel	30% fuel	15% fuel	5% fuel	fuel
1-FEDS-166	936	1135	1161	2480	1122
1-FEDS-195	633	704	726	1152	699
1-FEDS-244	470	485	506	623	481
1-FEDS-361	329	341	325	339	329
1-FEDS-417	300	310	302	313	302
2-FEDS-166	805	844	1134	2212	902
2-FEDS-195	455	548	624	976	532
2-FEDS-244	416	455	490	592	440
2-FEDS-361	331	345	340	355	334
2-FEDS-417	291	301	291	310	293
SERPENT-SHEM-166	3669	2396	2987	20173	768
SERPENT-SHEM-244	1995	1432	2196	11403	485
SERPENT-SHEM-361	1005	446	1125	3153	334
NJOY-SHEM-166	2857	2070	3382	20410	1116
NJOY-SHEM-244	1519	1180	2413	11482	624
NJOY-SHEM-361	883	310	1010	3120	268

Table 3.6: L1 errors in fission rates for different types of cross section data (NJOY-FEDS, SERPENT-SHEM, NJOY-SHEM) for 2D pin cell problem.

Method	50% fuel	30% fuel	15% fuel	5% fuel	fuel
1-FEDS-166	820	871	889	911	850
1-FEDS-195	501	520	513	519	509
1-FEDS-244	372	374	354	351	369
1-FEDS-361	300	289	259	250	288
1-FEDS-417	280	267	235	225	266
2-FEDS-166	669	676	660	662	670
2-FEDS-195	449	448	423	416	443
2-FEDS-244	379	361	324	309	361
2-FEDS-361	301	280	242	227	282
2-FEDS-417	270	252	215	202	253
SERPENT-SHEM-166	435	418	463	496	421
SERPENT-SHEM-244	226	229	272	301	228
SERPENT-SHEM-361	109	120	170	193	117
NJOY-SHEM-166	669	676	660	662	670
NJOY-SHEM-244	430	438	427	442	431
NJOY-SHEM-361	251	247	225	223	244

derivation can be described as follows for each material region:

$$\begin{aligned}
\boldsymbol{\Omega}\cdot\boldsymbol{\nabla}\psi(\boldsymbol{r},\boldsymbol{\Omega},E)+\Sigma_t(E)\psi(\boldsymbol{r},\boldsymbol{\Omega},E) &= q(\boldsymbol{r},\boldsymbol{\Omega},E)\,,\\
\int_D dV\int_{4\pi} d\Omega[\boldsymbol{\nabla}\cdot\boldsymbol{\Omega}+\Sigma_t(E)]\psi(\boldsymbol{r},\boldsymbol{\Omega},E) &= \int_D dV\int_{4\pi} d\Omega q(\boldsymbol{r},\boldsymbol{\Omega},E)\,,\\
\int_D dV[\Sigma_e(E)+\Sigma_t(E)]\phi(\boldsymbol{r},E) &= \int_D dV q(\boldsymbol{r},E)+\int_{\partial D} dS\int_{\boldsymbol{\Omega}\cdot\boldsymbol{n}\le 0} d\Omega|\boldsymbol{\Omega}\cdot\boldsymbol{n}|\psi(\boldsymbol{r},\boldsymbol{\Omega},E)\,.
\end{aligned}$$

The energy-dependent escape cross sections are obtained from MCNP for 12 coarse groups, listed in Table 3.7. In the previous calculations, the escape cross section is approximated by the average chord length $S/4V$, 1.27492 cm^{-1}. This approximation assumes that neutrons are created isotropically and are mono-energetic. From Table 3.7, it is observed that outgoing escape cross sections have larger values in high energy and smaller value in thermal energy, while the ingoing cross sections show the opposite behavior. The very high energy neutrons are mainly produced from fission in the fuel which accounts for the large value of outgoing escape cross sections in very high energy. Elastic scattering becomes dominant in the RRR range, and neutrons will lose most of their energy in the collision with small atomic nuclides in the moderator outside of the fuel. Hence, the incoming escape cross sections are larger in low energy range.

The results for k_{eff} using energy-dependent escape cross sections are listed in Table 3.8, denoted as 3-FEDS-X where $X = 166, 195, 244, 361,$ or 417. From Table 3.8, it is observed that introducing energy-dependent escape cross sections only reduces the error in k_{eff} for 166 groups. There is slight increase in the error for 195, 244 and 361 groups compared to 2-FEDS-X. However, the differences are below 17 pcm, which can be neglected.

The errors in absorption and fission rates in 50%, 30%, 15%, 5% fuel regions for NJOY-FEDS method with energy-dependent escape cross sections for 166 groups are plotted in Figs.3.6-3.7, respectively. The errors in in absorption and fission rates for the whole fuel region for NJOY-FEDS method with energy-dependent escape cross sections for 166 groups are plotted in Figs.3.8, and 3.9, respectively. Errors in absorption rates and fission rate for NJOY-FEDS method with energy-dependent escape cross sections for different unknown numbers are summarized in Tables

Table 3.7: Escape cross sections from MCNP for 12 coarse groups for 2D pin cell problem.

Coarse Group Upper Energy (eV)	Incoming Escape XS (cm^{-1})	Outgoing Escape XS (cm^{-1})
6.24999×10^{-1}	1.54077	1.14241
4.21983×10^{0}	1.30933	1.25631
9.50002×10^{0}	1.47026	1.20571
2.78852×10^{1}	1.37553	1.23578
5.17847×10^{1}	1.39364	1.23913
1.54176×10^{2}	1.34536	1.25519
5.39204×10^{2}	1.32090	1.26424
2.08410×10^{3}	1.30651	1.26994
9.11881×10^{3}	1.29184	1.27108
2.26994×10^{4}	1.28071	1.27275
1.40000×10^{5}	1.25357	1.28684
2.00000×10^{7}	1.17094	1.33863

Table 3.8: Errors in k_{eff} for NJOY-FEDS method with energy-dependent escape cross sections for 2D pin cell problem.

Method	Unknowns (RRR)	K_{eff}	E_{pcm}	Efficiency $\frac{1}{\lvert Error \rvert \times DOF}$
2-FEDS-166	30	1.46951	332±1	10.0
2-FEDS-195	59	1.46656	130±1	13.0
2-FEDS-244	108	1.46630	112±1	8.2
2-FEDS-361	225	1.46564	68±1	6.6
2-FEDS-417	281	1.46537	49±1	7.3
3-FEDS-166	30	1.46865	273±1	12.2
3-FEDS-195	59	1.46678	146±1	11.6
3-FEDS-244	108	1.46663	135±1	6.9
3-FEDS-361	225	1.46571	72±1	6.1
3-FEDS-417	281	1.46536	49±1	7.3
SERPENT-SHEM-166	30	1.46057	-279±1	11.9
SERPENT-SHEM-244	108	1.46250	-147±1	6.3
SERPENT-SHEM-361	225	1.46366	-68±1	6.6

3.9-3.10, respectively . L1 errors in absorption rates and fission rates for NJOY-FEDS method with energy-dependent escape cross sections for different unknown numbers are summarized in Tables 3.11-3.12. L1 errors in absorption and fission rates decreases after applying the energy-dependent escape cross sections in NJOY-FEDS method for 166 groups, which is also observed in the results of k_{eff}.

Table 3.9: Errors in integrated absorption rates for NJOY- FEDS method with energy-dependent escape cross sections for 2D pin cell problem.

Method	50% fuel	30% fuel	15% fuel	5% fuel	fuel
2-FEDS-166	279	33	-356	-1587	-26
2-FEDS-195	140	-20	-177	-625	-12
2-FEDS-244	81	-17	-128	-309	-9
2-FEDS-361	45	-10	-76	-153	-5
2-FEDS-417	40	-7	-65	-138	-4
3-FEDS-166	283	25	-323	-1612	-22
3-FEDS-195	158	-11	-206	-735	-13
3-FEDS-244	85	-11	-140	-336	-10
3-FEDS-361	45	-9	-76	-155	-5
3-FEDS-417	39	-6	-64	-141	-4
SERPENT-SHEM-166	2755	1419	-2971	-20161	-138
SERPENT-SHEM-244	1360	732	-1423	-11392	-149
SERPENT-SHEM-361	533	-94	-979	-3141	-152

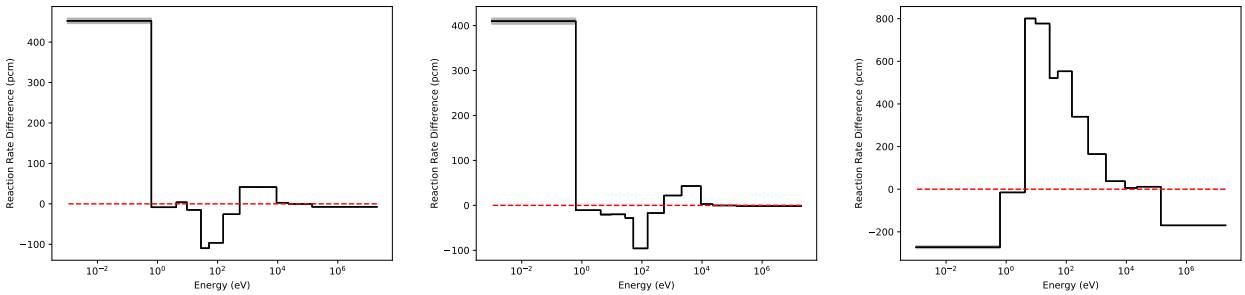

(a) 2-FEDS-50% fuel (b) 3-FEDS-50% fuel (c) SERPENT-SHEM-50% fuel

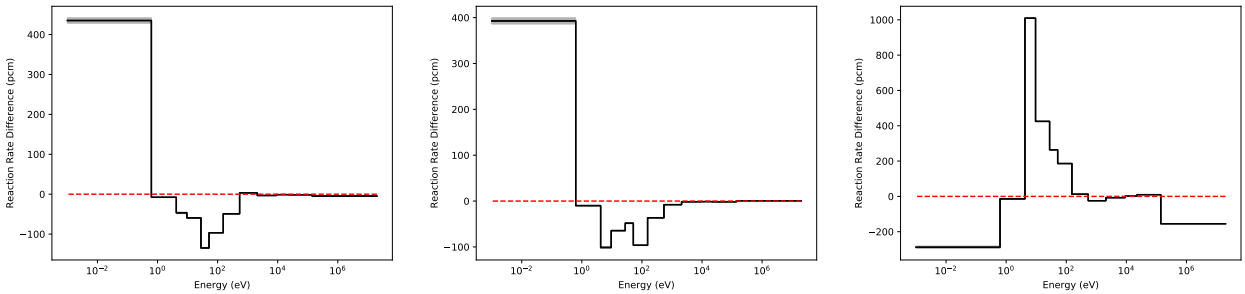

(d) 2-FEDS-30% fuel (e) 3-FEDS-30% fuel (f) SERPENT-SHEM-30% fuel

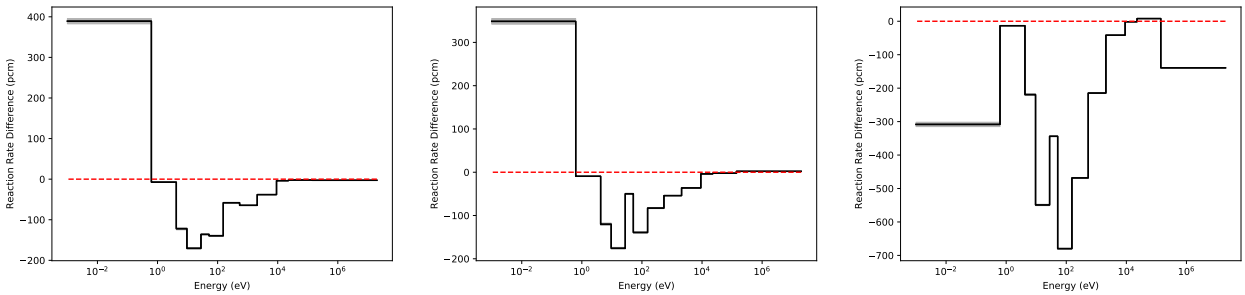

(g) 2-FEDS-15% fuel (h) 3-FEDS-15% fuel (i) SERPENT-FEDS-15% fuel

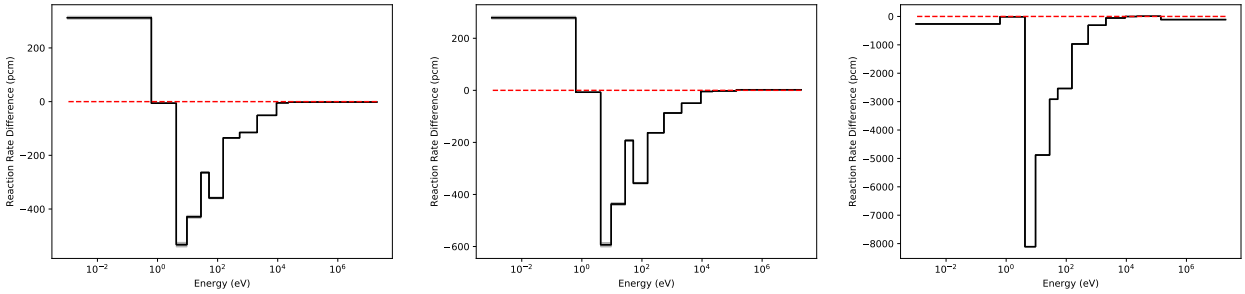

(j) 2-FEDS-5% fuel (k) 3-FEDS-5% fuel (l) SERPENT-SHEM-5% fuel

Figure 3.6: Absorption errors in multiple regions of the fuel between MCNP and PDT for different types of cross section data (2-FEDS-166, 3-FEDS-166, SERPENT-SHEM-166) for 2D pin cell problem (pcm in 95% condifence). Columns have the same cross sections. Rows have the same QOIs.

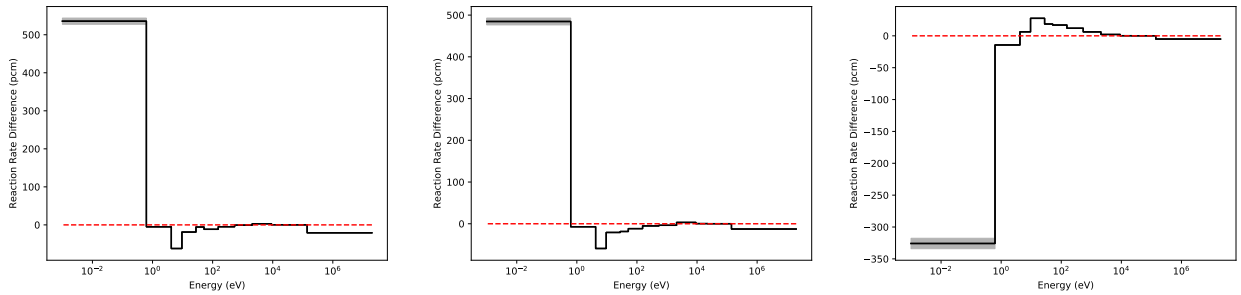

(a) 2-FEDS-50% fuel (b) 3-FEDS-50% fuel (c) SERPENT-SHEM-50% fuel

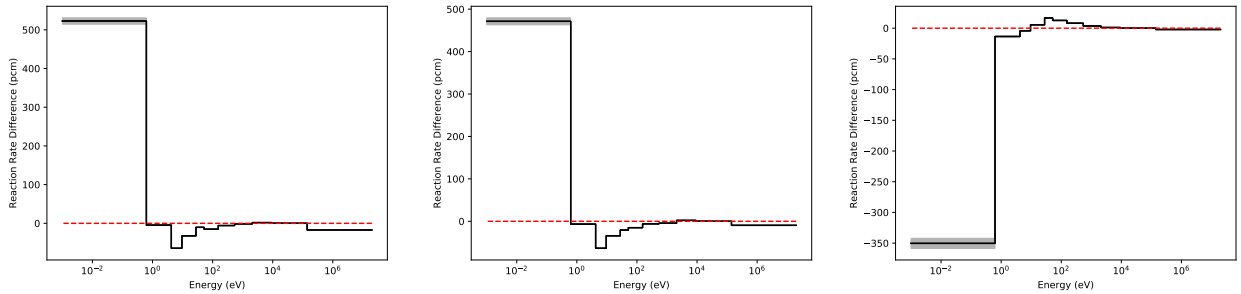

(d) 2-FEDS-30% fuel (e) 3-FEDS-30% fuel (f) SERPENT-SHEM-30% fuel

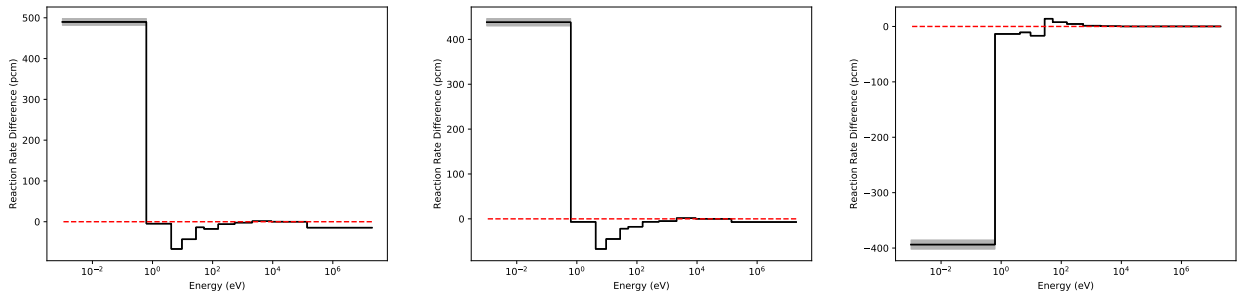

(g) 2-FEDS-15% fuel (h) 3-FEDS-15% fuel (i) SERPENT-SHEM-15% fuel

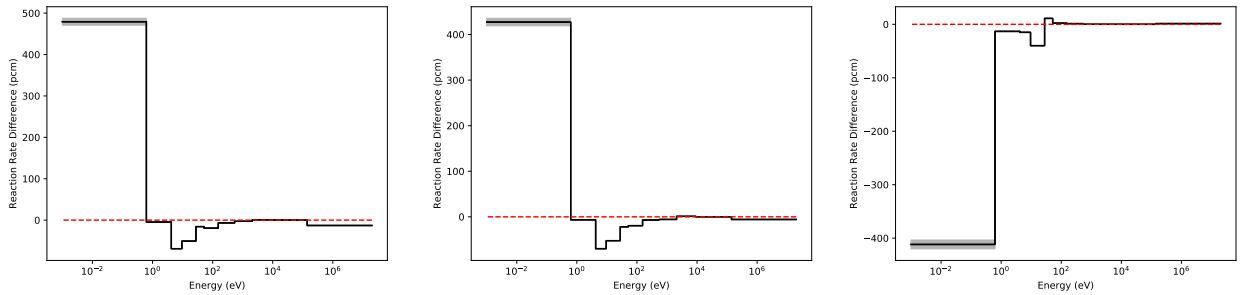

(j) 2-FEDS-5% fuel (k) 3-FEDS-5% fuel (l) SERPENT-SHEM-5% fuel

Figure 3.7: Fission errors in in multiple regions of the fuel between MCNP and PDT for different types of cross section data (2-FEDS-166, 3-FEDS-166, SERPENT-SHEM-166) for 2D pin cell problem (pcm in 95% condifence). Columns have the same cross sections. Rows have the same QOIs

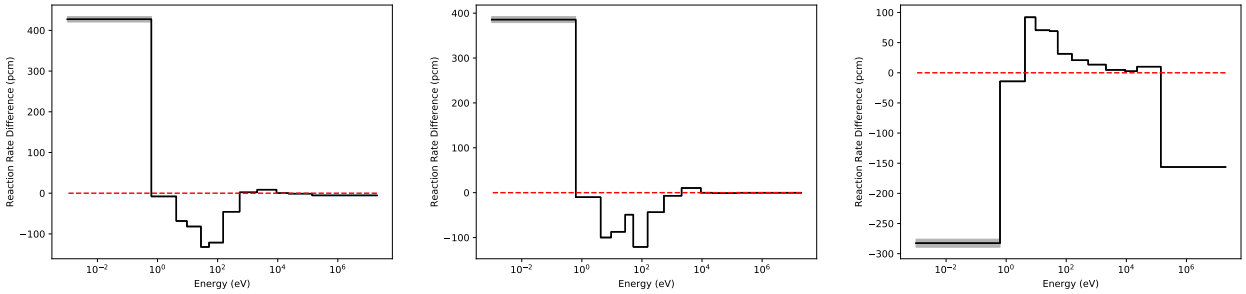

(a) 2-FEDS fuel (b) 3-FEDS fuel (c) SERPENT-SHEM fuel

Figure 3.8: Absorption errors in the whole fuel between MCNP and PDT for different types of cross section data (2-FEDS-166, 3-FEDS-166, SERPENT-SHEM-166) for 2D pin cell problem (pcm in 95% condifence).

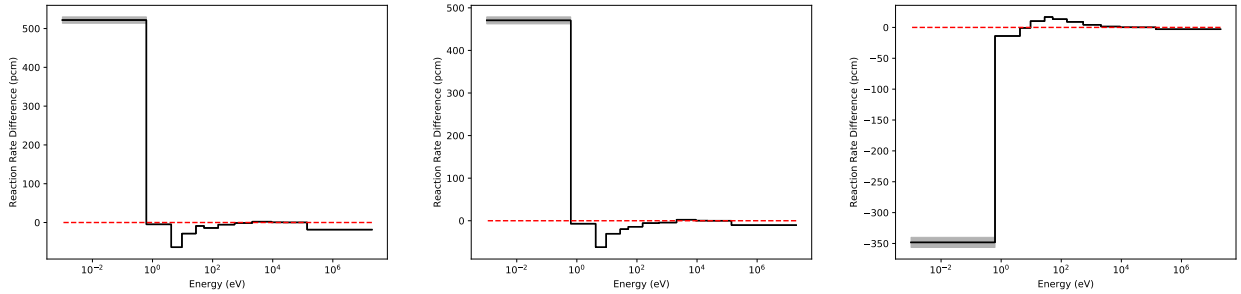

(a) 2-FEDS fuel (b) 3-FEDS fuel (c) SERPENT-SHEM fuel

Figure 3.9: Fission errors in the whole fuel between MCNP and PDT for different types of cross section data (2-FEDS-166, 3-FEDS-166, SERPENT-SHEM-166) for 2D pin cell problem (pcm in 95% condifence).

Table 3.10: Errors in integrated fission rates for NJOY- FEDS method with energy-dependent escape cross sections for 2D pin cell problem.

Method	50% fuel	30% fuel	15% fuel	5% fuel	fuel
2-FEDS-166	410	374	323	299	380
2-FEDS-195	201	172	127	111	176
2-FEDS-244	172	159	126	117	158
2-FEDS-361	126	114	82	74	113
2-FEDS-417	108	95	62	52	94
3-FEDS-166	350	314	263	240	320
3-FEDS-195	213	188	147	132	191
3-FEDS-244	195	180	147	138	180
3-FEDS-361	130	118	86	77	117
3-FEDS-417	113	99	66	56	98
SERPENT-SHEM-166	-255	-323	-406	-464	-311
SERPENT-SHEM-244	-133	-183	-250	-294	-175
SERPENT-SHEM-361	-57	-100	-159	-188	-93

Table 3.11: L1 errors in integrated absorption rates for NJOY- FEDS method with energy-dependent escape cross sections for 2D pin cell problem.

Method	50% fuel	30% fuel	15% fuel	5% fuel	fuel
2-FEDS-166	805	844	1134	2212	902
2-FEDS-195	455	548	624	976	532
2-FEDS-244	416	455	490	592	440
2-FEDS-361	331	345	340	355	334
2-FEDS-417	291	301	291	310	293
3-FEDS-166	672	762	1024	2175	814
3-FEDS-195	467	557	672	1103	556
3-FEDS-244	439	470	523	636	460
3-FEDS-361	330	341	340	358	329
3-FEDS-417	291	297	291	314	289
SERPENT-SHEM-166	3669	2396	2987	20173	768
SERPENT-SHEM-244	1995	1432	2196	11403	485
SERPENT-SHEM-361	1005	446	1125	3153	334

Table 3.12: L1 errors in integrated fission rates for NJOY- FEDS method with energy-dependent escape cross sections for 2D pin cell problem.

Method	50% fuel	30% fuel	15% fuel	5% fuel	fuel
2-FEDS-166	669	676	660	662	670
2-FEDS-195	449	448	423	416	443
2-FEDS-244	379	361	324	309	361
2-FEDS-361	301	280	242	227	282
2-FEDS-417	270	252	215	202	253
3-FEDS-166	627	634	617	617	627
3-FEDS-195	461	455	427	419	452
3-FEDS-244	375	359	323	309	359
3-FEDS-361	292	272	234	219	273
3-FEDS-417	262	243	207	193	244
SERPENT-SHEM-166	435	418	463	496	421
SERPENT-SHEM-244	226	229	272	301	228
SERPENT-SHEM-361	109	120	170	193	117

3.1.3 Testing Analytical Chord Length Models for Escape Cross Sections with Multiple Regions in Fuel

The effect of adding the spatial-resolution for cross sections generation in fuel material for NJOY-FEDS method is also invested. The fuel is further divided into two region, based on equal radius (ER) or equal volume (EV). Cross sections are generated for each region in the fuel. The escape cross sections in the hollow cylinder is approximated by the average chord length, given as

[7]

$$\bar{l}_{\text{MCD}} = d - d_i, \quad \bar{l}_{\text{OCD}} = \frac{d^2 - d_i^2}{d} \tag{3.4}$$

where l is the chord length, MCD is short for multichod distribution, and OCD is short for one-chord distribution.

The results for k_{eff} for NJOY-FEDS method with different chord length models with two regions in the fuel with equal radius and equal volume divisions are listed in Tables 3.13 and 3.18, respectively. Introducing the spatial resolutions greatly reduces the errors in k_{eff} for NJOY-FEDS method, while there is no accuracy improvement in the results for k_{eff} for SERPENT-SHEM method. The absolute errors in k_{eff} for NJOY-FEDS method with MCD model are all blow 45 pcm with equal volume division, while it reaches 81 pcm for equal radius division. For NJOY-FEDS method with OCD model, the errors in k_{eff} are both around 190 pcm for 166 groups with both equal radius and equal volume divisions.

The errors in absorption and fission rates in 25%, 25%, 30%, 15%, 5% fuel regions for NJOY-FEDS method with different chord length models with two divisions in the fuel for 166 groups are plotted in Figs.3.10, 3.11, 3.14 and 3.15. The errors in in absorption and fission rates for the whole fuel region for NJOY-FEDS method for 166 groups are plotted in Figs.3.12,3.13, 3.16 and 3.17, respectively. Errors in absorption rates and fission rate for NJOY-FEDS method with different chord length model for different unknown numbers are summarized in Tables 3.14,3.15, 3.19, and 3.20 respectively . L1 errors in absorption rates and fission rates for NJOY-FEDS method with different chord length models for different unknown numbers are summarized in Tables 3.16, 3.17, 3.21, and 3.22.

After introducing the spatial resolution in the fuel for cross section generation, there is reduction in absorption errors in thermal range in the multiple regions of the fuel for NJOY-FEDS method with both chord length models. With both division, the absorption errors slightly increase in the energy range $[2.08410 \times 10^3, 9.11881 \times 10^3]$ eV in 25%, 25%, 30% of fuel region for MCD model. There is minor improvement in the accuracy of absorption rate in the RRR range in the outer 5% of fuel regions for SERPENT-SHEM method with equal volume division. However, the

absorption error in the outer 5% fuel for SERPENT-SHEM method is one magnitude larger than that in NJOY-FEDS method. Comparing the L1 errors in absorption rates, NJOY-FEDS method with MCD model give better results than OCD model in every tested fuel region with the same number of unknowns for both divisions. In addition, the L1 errors in absorption rates are in generally smaller in equal volume division than that in equal radius division.

Table 3.13: Errors in k_{eff} for different types of cross section data (MCD-FEDS, OCD-FEDS, SERPENT-SHEM) with two regions in fuel with equal radius division for 2D pin cell problem.

Method	Unknowns (RRR)	K_{eff}	E_{pcm}	Efficiency $\frac{1}{\lvert Error \rvert \times DOF}$
MCD-FEDS-166	30	1.46494	19±1	170.9
MCD-FEDS-195	59	1.46399	-45±1	37.9
MCD-FEDS-244	108	1.46488	16±1	58.8
MCD-FEDS-361	225	1.46466	1±1	496.9
MCD-FEDS-417	281	1.46455	-7±1	51.2
OCD-FEDS-166	30	1.46747	193 ±1	17.3
OCD-FEDS-195	59	1.46556	62 ±1	27.2
OCD-FEDS-244	108	1.46543	53 ±1	17.4
OCD-FEDS-361	225	1.46516	35 ±1	12.9
OCD-FEDS-417	281	1.46486	14 ±1	25.2
SERPENT-SHEM-166	30	1.45928	-367 ±1	9.1
SERPENT-SHEM-244	108	1.46130	-229 ±1	4.0
SERPENT-SHEM-361	225	1.46262	-139 ±1	3.2

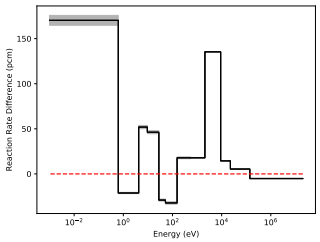

(a) MCD-FEDS-25% fuel

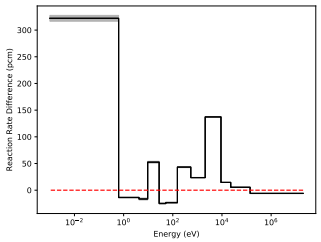

(b) OCD-FEDS-25% fuel

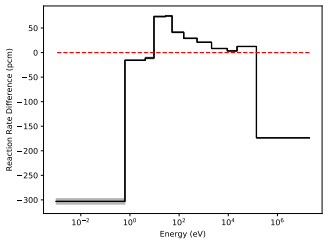

(c) SERPENT-SHEM-25% fuel

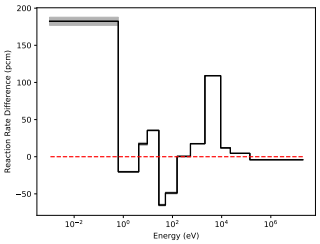

(d) MCD-FEDS-25% fuel

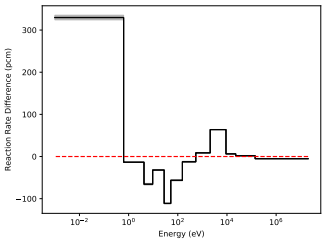

(e) OCD-FEDS-25% fuel

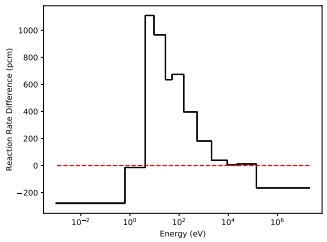

(f) SERPENT-SHEM-25% fuel

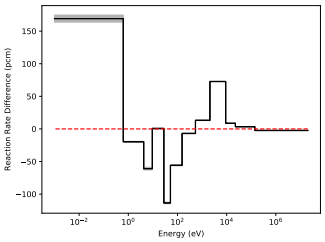

(g) MCD-FEDS-30% fuel

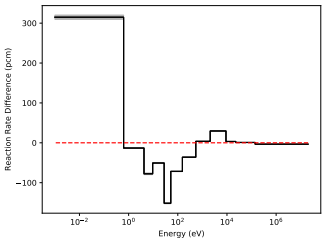

(h) OCD-FEDS-30% fuel

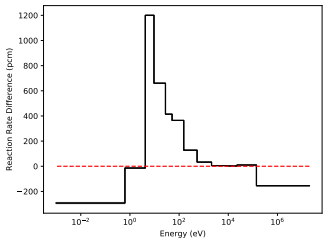

(i) SERPENT-FEDS-30% fuel

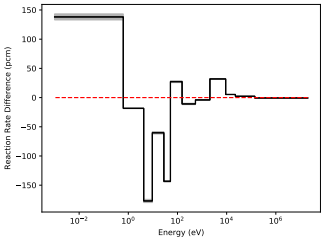

(j) MCD-FEDS-15% fuel

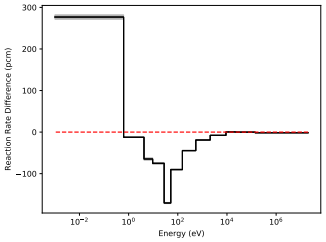

(k) OCD-FEDS-15% fuel

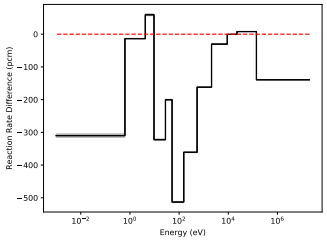

(l) SERPENT-SHEM-15% fuel

Figure 3.10: Absorption errors in multiple regions of the fuel between MCNP and PDT for different types of cross section data (MCD-FEDS-166, OCD-FEDS-166, SERPENT-SHEM-166) with two regions in fuel with equal radius division for 2D pin cell problem (pcm in 95% condifence). Columns have the same cross sections. Rows have the same QOIs.

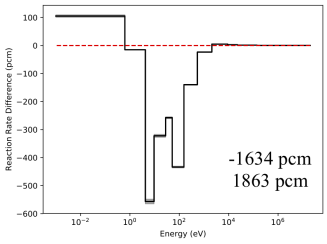

(m) MCD-FEDS-5% fuel

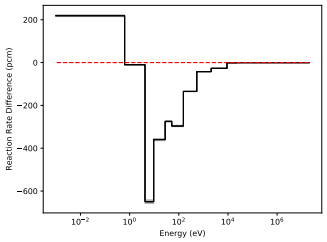

(n) OCD-FEDS-5% fuel

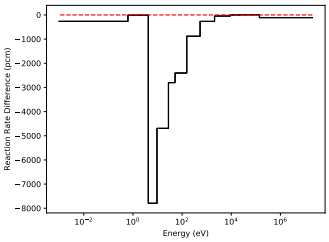

(o) SERPENT-SHEM-5% fuel

Figure 3.10: Continued.

Table 3.14: Errors in integrated absorption rates for different types of cross section data (MCD-FEDS, OCD-FEDS, SERPENT-SHEM) with two regions in fuel with equal radius division for 2D pin cell problem.

Method	25% fuel	25% fuel	30% fuel	15% fuel	5% fuel	fuel
MCD-FEDS-166	372	240	9	-210	-1634	0
MCD-FEDS-195	153	112	7	-143	-509	6
MCD-FEDS-244	86	68	1	-84	-281	4
MCD-FEDS-361	56	49	4	-63	-156	5
MCD-FEDS-417	46	45	7	-55	-136	5
OCD-FEDS-166	514	114	-52	-209	-1578	-11
OCD-FEDS-195	293	81	-38	-227	-584	-1
OCD-FEDS-244	163	45	-25	-123	-291	1
OCD-FEDS-361	97	34	-14	-83	-160	2
OCD-FEDS-417	83	34	-8	-75	-138	3
SERPENT-SHEM-166	-240	3559	2355	-1985	-19271	-133
SERPENT-SHEM-244	-343	1827	1224	-833	-10784	-144
SERPENT-SHEM-361	-181	681	154	-716	-2904	-147

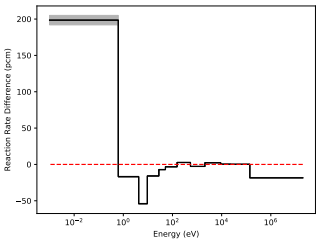

(a) MCD-FEDS-25% fuel

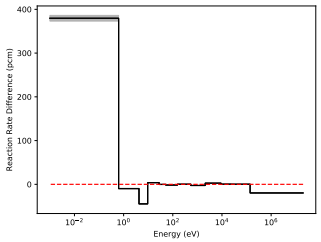

(b) OCD-FEDS-25% fuel

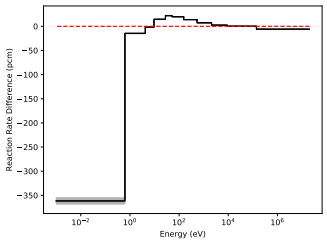

(c) SERPENT-SHEM-25% fuel

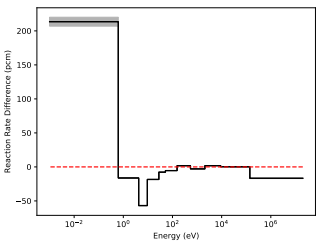

(d) MCD-FEDS-25% fuel

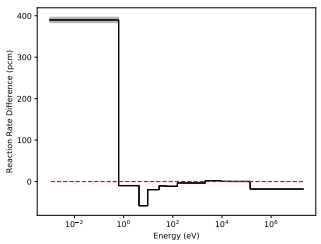

(e) OCD-FEDS-25% fuel

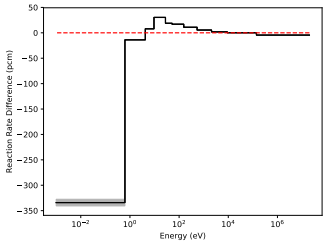

(f) SERPENT-SHEM-25% fuel

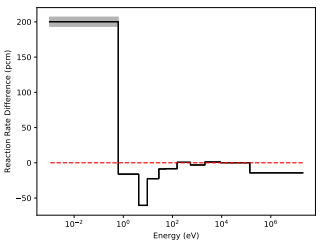

(g) MCD-FEDS-30% fuel

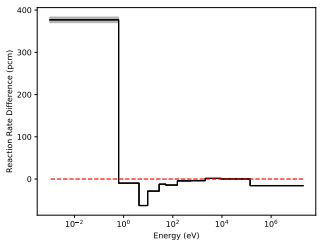

(h) OCD-FEDS-30% fuel

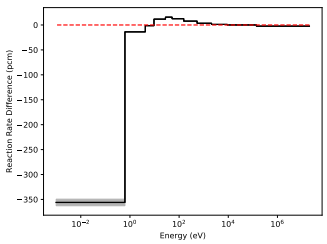

(i) SERPENT-SHEM-30% fuel

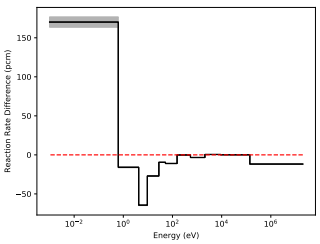

(j) MCD-FEDS-15% fuel

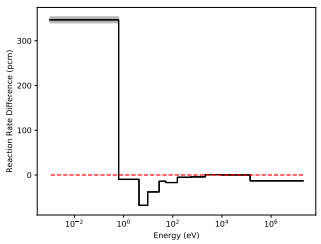

(k) OCD-FEDS-15% fuel

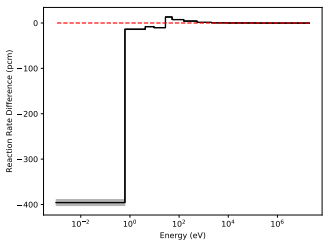

(l) SERPENT-SHEM-15% fuel

Figure 3.11: Fission errors in multiple regions of the fuel between MCNP and PDT for different types of cross section data (MCD-FEDS-166, OCD-FEDS-166, SERPENT-SHEM-166) with two regions in fuel with equal radius division for 2D pin cell problem (pcm in 95% condifence). Columns have the same cross sections. Rows have the same QOIs.

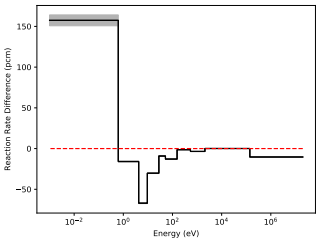

(m) MCD-FEDS-5% fuel

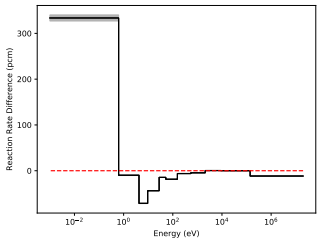

(n) OCD-FEDS-5% fuel

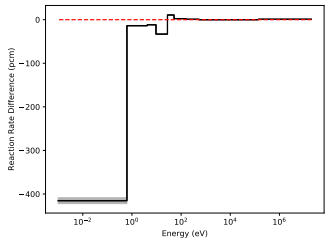

(o) SERPENT-SHEM-5% fuel

Figure 3.11: Continued.

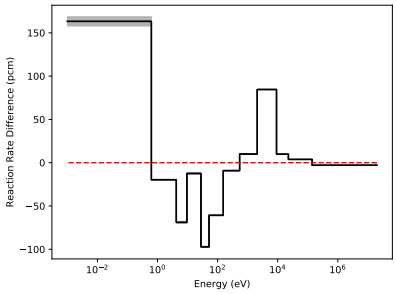

(a) MCD-FEDS fuel

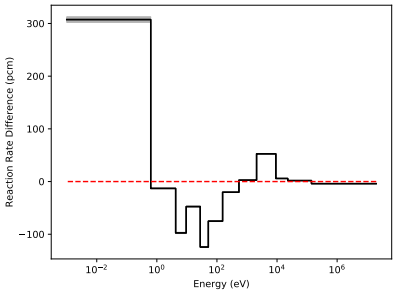

(b) OCD-FEDS fuel

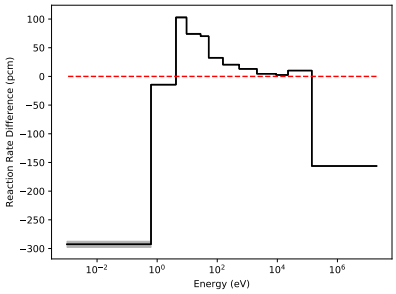

(c) SERPENT-SHEM fuel

Figure 3.12: Absorption errors in the whole fuel between MCNP and PDT for different types of cross section data (MCD-FEDS-166, OCD-FEDS-166, SERPENT-SHEM-166) with two regions in fuel with equal radius division for 2D pin cell problem (pcm in 95% condifence).

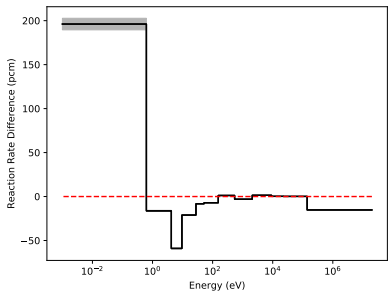

(a) MCD-FEDS fuel

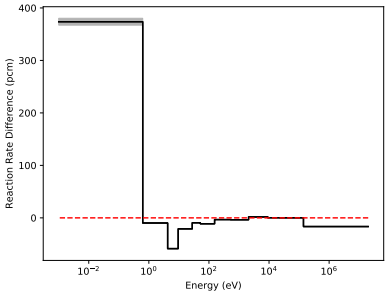

(b) OCD-FEDS fuel

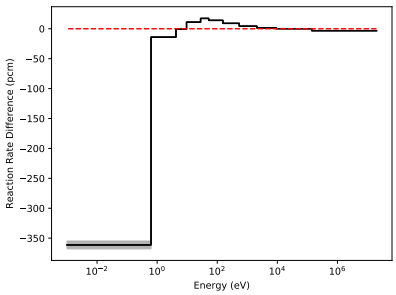

(c) SERPENT-SHEM fuel

Figure 3.13: Fission errors in the whole fuel between MCNP and PDT for different types of cross section data (MCD-FEDS-166, OCD-FEDS-166, SERPENT-SHEM-166) with two regions in fuel with equal radius division for 2D pin cell problem (pcm in 95% condifence).

Table 3.15: Errors in integrated fission rates for different types of cross section data (MCD-FEDS, OCD-FEDS, SERPENT-SHEM) with two regions in fuel with equal radius division for 2D pin cell problem.

Method	25% fuel	25% fuel	30% fuel	15% fuel	5% fuel	fuel
MCD-FEDS-166	86	93	69	28	7	69
MCD-FEDS-195	13	24	6	-28	-40	4
MCD-FEDS-244	68	83	68	39	28	65
MCD-FEDS-361	49	67	55	27	16	50
MCD-FEDS-417	42	59	47	18	7	42
OCD-FEDS-166	308	258	227	179	154	243
OCD-FEDS-195	134	122	108	79	68	111
OCD-FEDS-244	123	115	100	70	58	102
OCD-FEDS-361	97	97	84	55	43	83
OCD-FEDS-417	75	77	64	34	23	63
SERPENT-SHEM-166	-303	-260	-321	-401	-459	-322
SERPENT-SHEM-244	-178	-135	-178	-241	-285	-183
SERPENT-SHEM-361	-89	-50	-87	-143	-173	-92

Table 3.16: L1 errors in integrated absorption rates for different types of cross section data (MCD-FEDS, OCD-FEDS, SERPENT-SHEM) with two regions in fuel with equal radius division for 2D pin cell problem.

Method	25% fuel	25% fuel	30% fuel	15% fuel	5% fuel	fuel
MCD-FEDS-166	547	517	527	619	1863	542
MCD-FEDS-195	236	236	280	318	620	270
MCD-FEDS-244	273	295	312	302	433	302
MCD-FEDS-361	226	242	249	240	279	240
MCD-FEDS-417	214	226	228	217	248	222
OCD-FEDS-166	683	707	757	763	2016	752
OCD-FEDS-195	391	390	455	547	828	421
OCD-FEDS-244	317	342	363	381	483	343
OCD-FEDS-361	271	302	308	306	324	291
OCD-FEDS-417	236	254	259	258	270	247
SERPENT-SHEM-166	767	4477	3279	2120	19283	794
SERPENT-SHEM-244	621	2456	1861	1962	10795	501
SERPENT-SHEM-361	356	1132	615	926	2916	334

Table 3.17: L1 errors in integrated fission rates for different types of cross section data (MCD-FEDS, OCD-FEDS, SERPENT-SHEM) with two regions in fuel with equal radius division for 2D pin cell problem.

Method	25% fuel	25% fuel	30% fuel	15% fuel	5% fuel	fuel
MCD-FEDS-166	322	342	336	314	308	329
MCD-FEDS-195	211	226	213	183	169	209
MCD-FEDS-244	230	244	231	200	184	227
MCD-FEDS-361	204	215	199	166	150	196
MCD-FEDS-417	196	208	192	160	144	189
OCD-FEDS-166	465	527	530	517	515	509
OCD-FEDS-195	322	349	334	301	284	326
OCD-FEDS-244	264	291	276	244	228	269
OCD-FEDS-361	247	266	249	215	199	245
OCD-FEDS-417	220	237	220	187	173	216
SERPENT-SHEM-166	464	445	426	455	489	437
SERPENT-SHEM-244	256	226	226	262	290	236
SERPENT-SHEM-361	130	100	107	152	176	116

Table 3.18: Errors in k_{eff} for different types of cross section data (MCD-FEDS, OCD-FEDS, SERPENT-SHEM) with two regions in fuel with equal volume division for 2D pin cell problem.

Method	Unknowns (RRR)	K_{eff}	E_{pcm}	Efficiency $\frac{1}{\lvert Error \rvert \times DOF}$
MCD-FEDS-166	30	1.46347	-81 $\pm$1	41.2
MCD-FEDS-195	59	1.46446	-13 $\pm$1	127.8
MCD-FEDS-244	108	1.46530	44 $\pm$1	20.8
MCD-FEDS-361	225	1.46456	-6 $\pm$1	71.0
MCD-FEDS-417	281	1.46451	-10 $\pm$1	36.7
OCD-FEDS-166	30	1.46749	194 $\pm$1	17.2
OCD-FEDS-195	59	1.46455	-7 $\pm$1	252.5
OCD-FEDS-244	108	1.46491	18 $\pm$1	51.3
OCD-FEDS-361	225	1.46489	16 $\pm$1	27.4
OCD-FEDS-417	281	1.46465	0 $\pm$1	1628.8
SERPENT-SHEM-166	30	1.45915	-376 $\pm$1	8.9
SERPENT-SHEM-244	108	1.46116	-238 $\pm$1	3.9
SERPENT-SHEM-361	225	1.46256	-142 $\pm$1	3.1

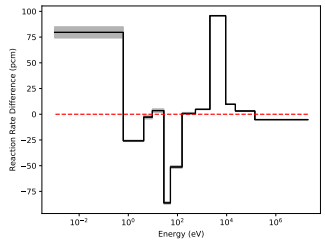

(a) MCD-FEDS-25% fuel

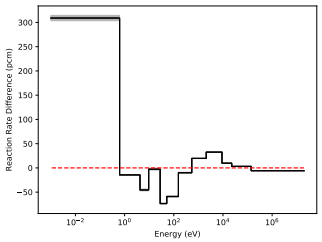

(b) OCD-FEDS-25% fuel

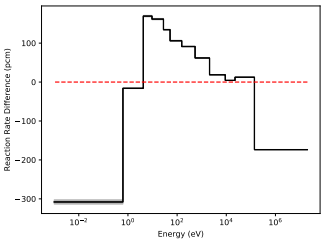

(c) SERPENT-SHEM-25% fuel

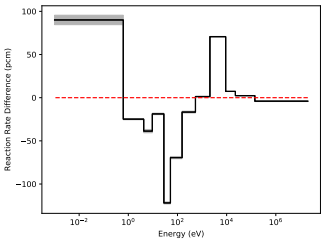

(d) MCD-FEDS-25% fuel

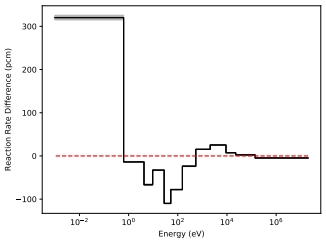

(e) OCD-FEDS-25% fuel

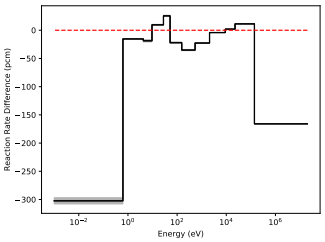

(f) SERPENT-SHEM-25% fuel

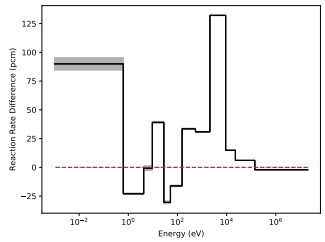

(g) MCD-FEDS-30% fuel

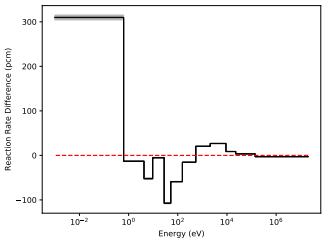

(h) OCD-FEDS-30% fuel

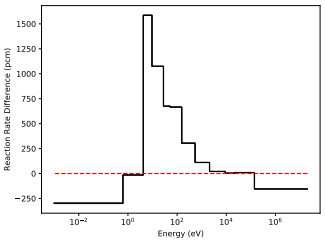

(i) SERPENT-FEDS-30% fuel

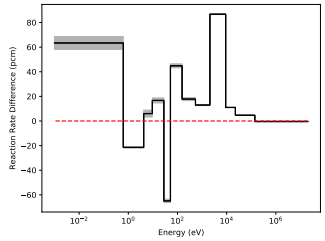

(j) MCD-FEDS-15% fuel

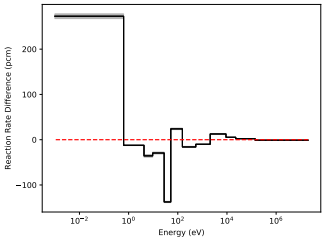

(k) OCD-FEDS-15% fuel

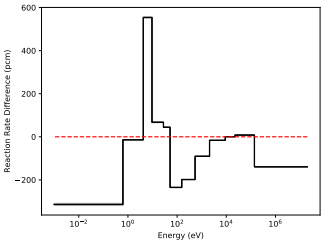

(l) SERPENT-SHEM-15% fuel

Figure 3.14: Absorption errors in multiple regions of the fuel between MCNP and PDT for different types of cross section data (MCD-FEDS-166, OCD-FEDS-166, SERPENT- SHEM-166) with two regions in fuel with equal volume division for 2D pin cell problem (pcm in 95% condifence). Columns have the same cross sections. Rows have the same QOIs.

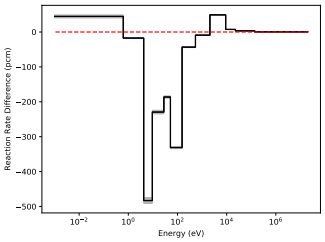

(m) MCD-FEDS-5% fuel

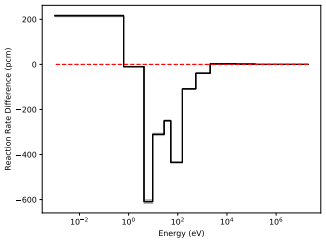

(n) OCD-FEDS-5% fuel

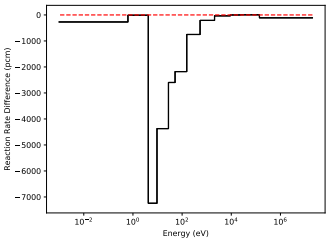

(o) SERPENT-SHEM-5% fuel

Figure 3.14: Continued.

Table 3.19: Errors in integrated absorption rates for different types of cross section data (MCD-FEDS, OCD-FEDS, SERPENT-SHEM) with two regions in fuel with equal volume division for 2D pin cell problem.

Method	25% fuel	25% fuel	30% fuel	15% fuel	5% fuel	fuel
MCD-FEDS-166	26	-123	274	177	-1195	7
MCD-FEDS-195	-10	-68	153	39	-410	6
MCD-FEDS-244	-17	-43	100	13	-225	3
MCD-FEDS-361	-1	-10	63	-12	-126	6
MCD-FEDS-417	-1	-4	54	-10	-111	6
OCD-FEDS-166	163	41	114	75	-1540	-11
OCD-FEDS-195	95	47	67	-113	-472	3
OCD-FEDS-244	56	28	38	-69	-244	3
OCD-FEDS-361	32	24	23	-47	-133	3
OCD-FEDS-417	30	27	22	-44	-122	5
SERPENT-SHEM-166	263	-538	3983	-333	-17771	-132
SERPENT-SHEM-244	44	-515	2061	105	-9787	-141
SERPENT-SHEM-361	17	-324	515	-348	-2558	-149

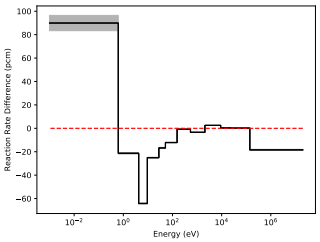

(a) MCD-FEDS-25% fuel

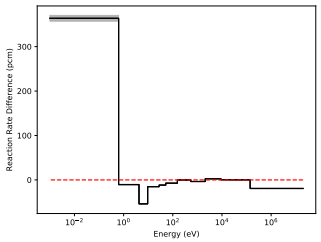

(b) OCD-FEDS-25% fuel

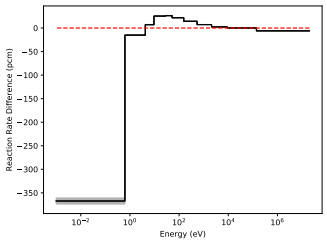

(c) SERPENT-SHEM-25% fuel

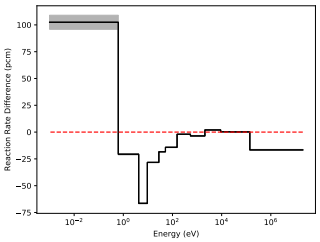

(d) MCD-FEDS-25% fuel

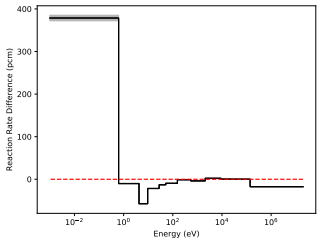

(e) OCD-FEDS-25% fuel

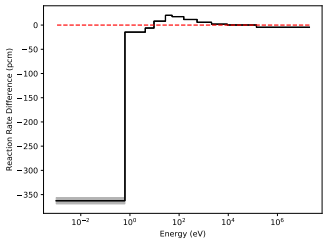

(f) SERPENT-SHEM-25% fuel

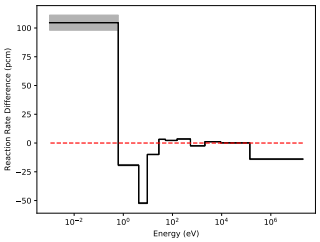

(g) MCD-FEDS-30% fuel

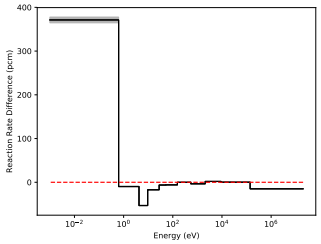

(h) OCD-FEDS-30% fuel

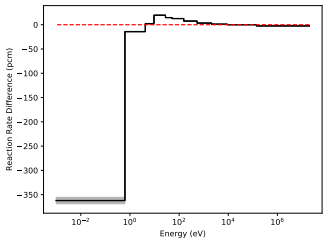

(i) SERPENT-FEDS-30% fuel

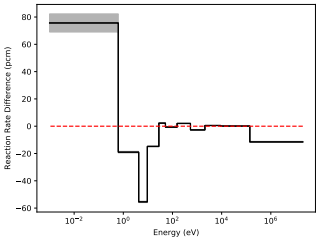

(j) MCD-FEDS-15% fuel

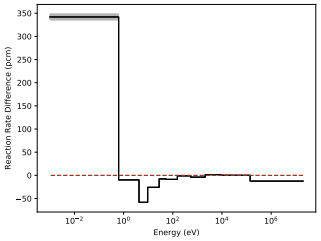

(k) OCD-FEDS-15% fuel

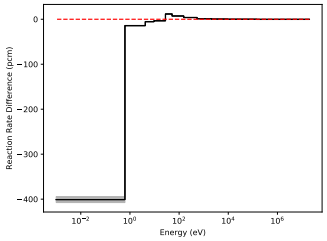

(l) SERPENT-SHEM-15% fuel

Figure 3.15: Fission errors in multiple regions of the fuel between MCNP and PDT for different types of cross section data (MCD-FEDS-166, OCD-FEDS-166, SERPENT- SHEM-166) with two regions in fuel with equal volume division for 2D pin cell problem (pcm in 95% condifence). Columns have the same cross sections. Rows have the same QOIs.

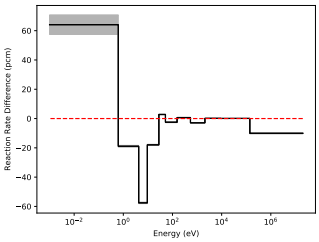

(m) MCD-FEDS-5% fuel

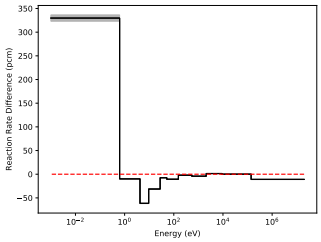

(n) OCD-FEDS-5% fuel

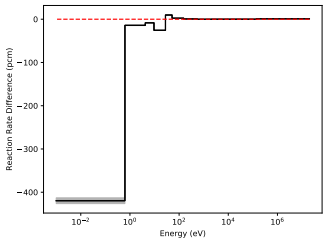

(o) SERPENT-SHEM-5% fuel

Figure 3.15: Continued.

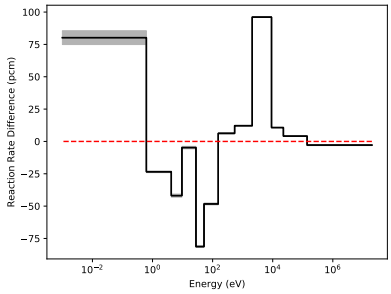

(a) MCD-FEDS fuel

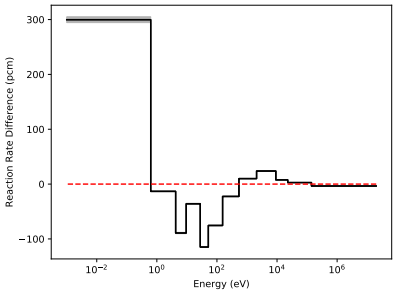

(b) OCD-FEDS fuel

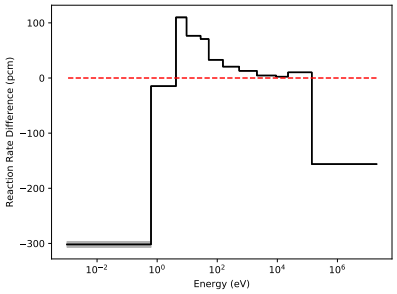

(c) SERPENT-SHEM fuel

Figure 3.16: Absorption errors in the whole fuel between MCNP and PDT for different types of cross section data (MCD-FEDS-166, OCD-FEDS-166, SERPENT- SHEM-166) with two regions in fuel with equal volume division for 2D pin cell problem (pcm in 95% condifence).

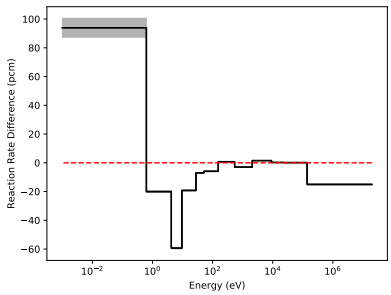

(a) MCD-FEDS fuel

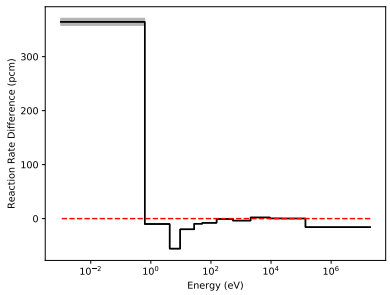

(b) OCD-FEDS fuel

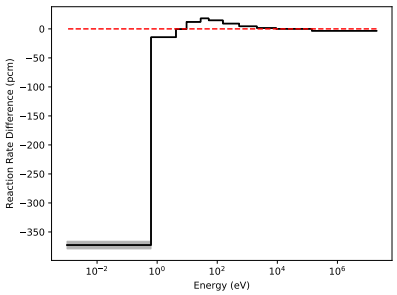

(c) SERPENT-SHEM fuel

Figure 3.17: Fission errors in the whole fuel between MCNP and PDT for different types of cross section data (MCD-FEDS-166, OCD-FEDS-166, SERPENT- SHEM-166) with two regions in fuel with equal volume division for 2D pin cell problem (pcm in 95% condifence).

Table 3.20: Errors in integrated fission rates for different types of cross section data (MCD- FEDS, OCD-FEDS, SERPENT-SHEM) with two regions in fuel with equal volume division for 2D pin cell problem.

Method	25% fuel	25% fuel	30% fuel	15% fuel	5% fuel	fuel
MCD-FEDS-166	-69	-65	17	-24	-42	-33
MCD-FEDS-195	3	13	75	43	31	35
MCD-FEDS-244	65	78	126	97	87	93
MCD-FEDS-361	20	35	68	41	31	42
MCD-FEDS-417	19	34	62	34	24	39
OCD-FEDS-166	245	247	263	216	193	244
OCD-FEDS-195	32	47	56	27	18	42
OCD-FEDS-244	60	74	80	50	39	67
OCD-FEDS-361	58	74	76	48	37	65
OCD-FEDS-417	43	59	59	31	20	49
SERPENT-SHEM-166	-283	-323	-317	-399	-454	-331
SERPENT-SHEM-244	-168	-186	-176	-238	-279	-192
SERPENT-SHEM-361	-82	-88	-80	-135	-164	-96

Table 3.21: L1 errors in integrated absorption rates for different types of cross section data (MCD-FEDS, OCD-FEDS, SERPENT-SHEM) with two regions in fuel with equal volume division for 2D pin cell problem.

Method	25% fuel	25% fuel	30% fuel	15% fuel	5% fuel	fuel
MCD-FEDS-166	369	466	419	351	1404	412
MCD-FEDS-195	277	335	268	229	576	277
MCD-FEDS-244	345	375	296	287	437	333
MCD-FEDS-361	227	247	235	214	259	230
MCD-FEDS-417	206	222	217	192	232	205
OCD-FEDS-166	585	700	624	559	1985	699
OCD-FEDS-195	297	338	312	362	643	341
OCD-FEDS-244	279	310	292	299	407	301
OCD-FEDS-361	258	278	270	259	284	268
OCD-FEDS-417	220	238	232	223	247	229
SERPENT-SHEM-166	1258	635	4918	1682	17783	814
SERPENT-SHEM-244	784	542	2705	1825	9798	520
SERPENT-SHEM-361	533	351	974	663	2569	338

Table 3.22: L1 errors in integrated fission rates for different types of cross section data (MCD-FEDS, OCD-FEDS, SERPENT-SHEM) with two regions in fuel with equal volume division for 2D pin cell problem.

Method	25% fuel	25% fuel	30% fuel	15% fuel	5% fuel	fuel
MCD-FEDS-166	255	275	213	185	178	226
MCD-FEDS-195	211	224	188	153	140	189
MCD-FEDS-244	244	257	231	195	178	224
MCD-FEDS-361	197	207	177	147	134	182
MCD-FEDS-417	187	198	173	143	130	176
OCD-FEDS-166	488	515	484	471	469	490
OCD-FEDS-195	279	291	263	230	213	266
OCD-FEDS-244	244	257	233	201	186	234
OCD-FEDS-361	231	242	222	188	173	221
OCD-FEDS-417	206	217	198	166	153	197
SERPENT-SHEM-166	494	453	440	449	482	451
SERPENT-SHEM-244	263	252	232	260	284	247
SERPENT-SHEM-361	130	120	105	143	167	121

Investigation is also performed for three regions in the fuel for cross section generation for NJOY-FEDS method using MCD model compared to SERPENT-SHEM method with EV and ER division.

The results for k_{eff} for NJOY-FEDS method with MCD model with three regions in the fuel are listed in Tables 3.23 and 3.28. However, the errors in k_{eff} increase for NJOY-FEDS method with MCD model after further increasing the spatial resolution from two regions to three regions in the fuel. In addition, NJOY-FEDS method show better results in k_{eff} in ER division than EV division,

which is not the case in two regions calculation. There is no difference in k_{eff} for SERPENT-SHEM method for adding spatial resolution.

The errors in absorption and fission rates in 11%, 22%, 11%, 22%, 19%, 15%, 5% fuel regions for NJOY-FEDS method with MCD model with two divisions in the fuel for 166 groups are plotted in Figs.3.18, 3.19, 3.22 and 3.23. The errors in in absorption and fission rates for the whole fuel region for NJOY-FEDS method for 166 groups are plotted in Figs.3.20, 3.21, 3.24 and 3.25, respectively. Errors in absorption rates and fission rate for NJOY-FEDS method with MCD model for different unknown numbers are summarized in Tables 3.24, 3.25, 3.29 and 3.30 respectively . L1 errors in absorption rates and fission rates for NJOY-FEDS method with different chord length models for different unknown numbers are summarized in Tables 3.26, 3.27, 3.31, and 3.32.

Further increasing the spatial resolution in the fuel for cross section generation, there is reduction in absorption errors in thermal range in 11%, 22%, 11%, 22%, 19%, 15%, 5% fuel regions for NJOY-FEDS method with MCD model with both division, as is observed in two region calculations. The absorption errors slightly increase in the energy range $[2.08410 \times 10^3, 9.11881 \times 10^3]$ eV in 11%, 22%, 11%, 22%, 19%, 15%, of fuel region for NJOY-FEDS method with MCD method with both division. For SERPENT-SHEM method, with ER division, the maximum absorption errors in RRR are all below 100 pcm in the inner 11%, 22%, 11% fuel regions. There is minor improvement in the accuracy of absorption rate in the RRR range in the outer 5% of fuel regions for SERPENT-SHEM method with equal volume division. However, the absorption error in the outer 5% fuel for SERPENT-SHEM method is one magnitude larger than that in NJOY-FEDS method. The L1 errors in absorption rates are in generally smaller in equal volume division that that in equal radius division for both methods. While no obvious improvement is observed in the results in k_{eff}, the L1 errors in absorption rates for the outer 5% fuel region decrease after further increasing the spatial resolutions in the cross section generation.

Table 3.23: Errors in k_{eff} for different types of cross section data (MCD-FEDS, SERPENT-SHEM) with three regions in fuel with equal radius division for 2D pin cell problem.

Method	Unknowns (RRR)	K_{eff}	E_{pcm}	Efficiency $\frac{1}{\lvert Error \rvert \times DOF}$
MCD-FEDS-166	30	1.46161	-208 $\pm$1	16.1
MCD-FEDS-195	59	1.46329	-93 $\pm$1	18.2
MCD-FEDS-244	108	1.46404	-41 $\pm$1	22.4
MCD-FEDS-361	225	1.46446	-13 $\pm$1	33.6
MCD-FEDS-417	281	1.46433	-22 $\pm$1	16.2
SERPENT-SHEM-166	30	1.45911	-378 $\pm$1	8.8
SERPENT-SHEM-244	108	1.46109	-243 $\pm$1	3.8
SERPENT-SHEM-361	225	1.46254	-144 $\pm$1	3.1

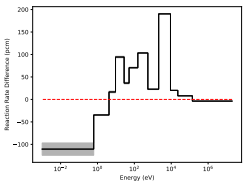

(a) M-11% fuel

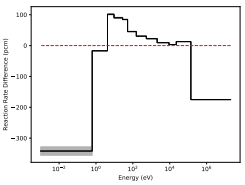

(b) S-11% fuel

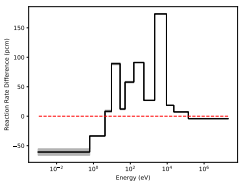

(c) M-22% fuel

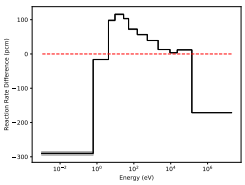

(d) S-22% fuel

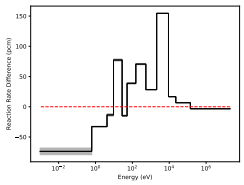

(e) M-11% fuel

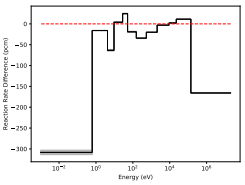

(f) S-11% fuel

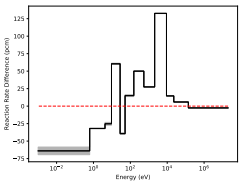

(g) M-22% fuel

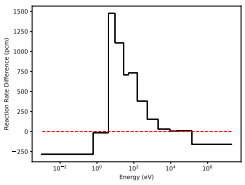

(h) S-22% fuel

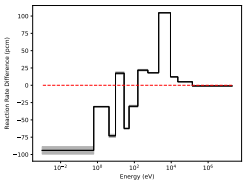

(i) M-19% fuel

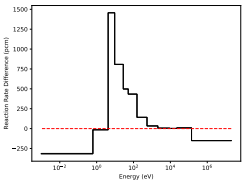

(j) S-19% fuel

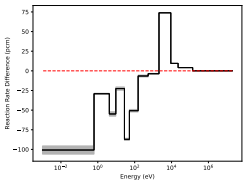

(k) M-15% fuel

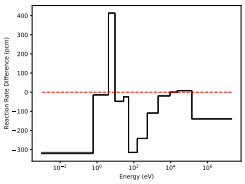

(l) S-15% fuel

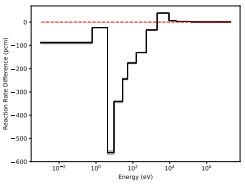

(m) M-5% fuel

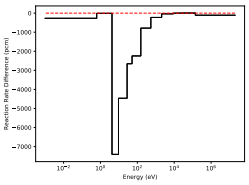

(n) S-5% fuel

Figure 3.18: Absorption errors in multiple regions of the fuel between MCNP and PDT for different types of cross section data (MCD-FEDS-166, SERPENT-SHEM-166) with three regions in fuel with equal radius division for 2D pin cell problem (pcm in 95% condifence). Columns have the same cross sections. Rows have the same QOIs.

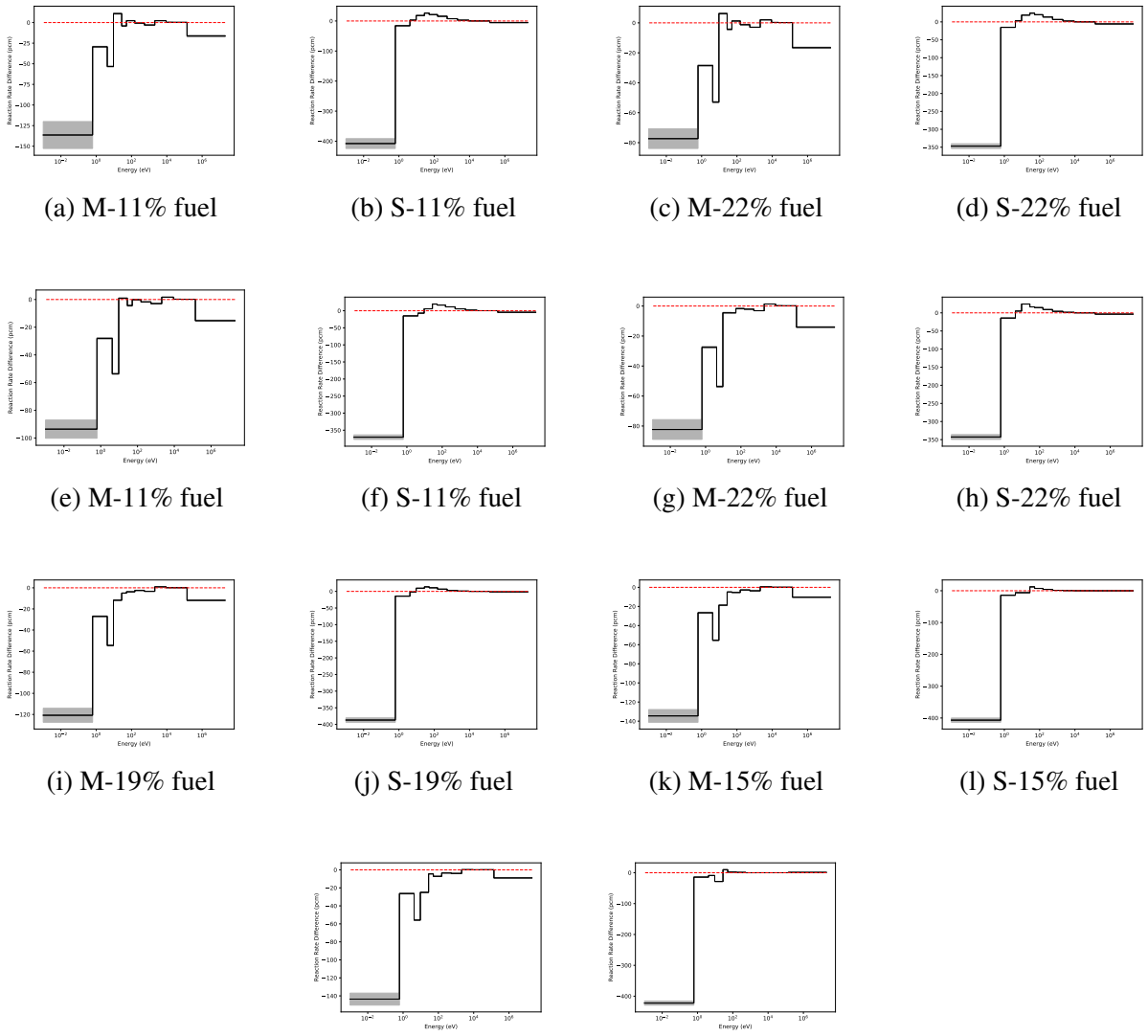

(a) M-11% fuel (b) S-11% fuel (c) M-22% fuel (d) S-22% fuel

(e) M-11% fuel (f) S-11% fuel (g) M-22% fuel (h) S-22% fuel

(i) M-19% fuel (j) S-19% fuel (k) M-15% fuel (l) S-15% fuel

(m) M-5% fuel (n) S-5% fuel

Figure 3.19: Fission errors in multiple regions of the fuel between MCNP and PDT for different types of cross section data (MCD-FEDS-166, SERPENT-SHEM-166) with three regions in fuel with equal radius division for 2D pin cell problem (pcm in 95% condifence). Columns have the same cross sections. Rows have the same QOIs.

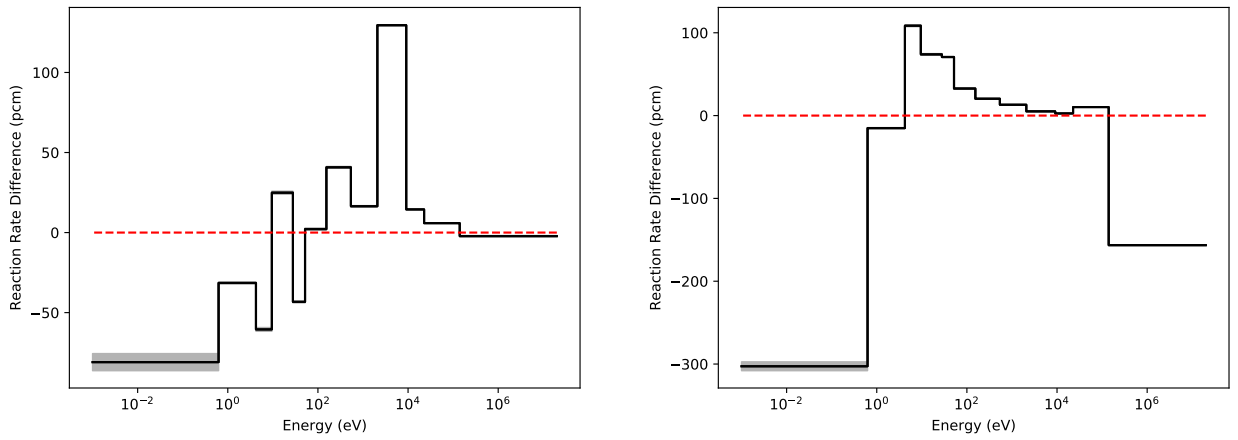

(a) MCD-FEDS fuel

(b) OCD-FEDS fuel

Figure 3.20: Absorption errors in the whole fuel between MCNP and PDT for different types of cross section data (MCD-FEDS-166, SERPENT-SHEM-166) with three regions in fuel with equal radius division for 2D pin cell problem (pcm in 95% condifence).

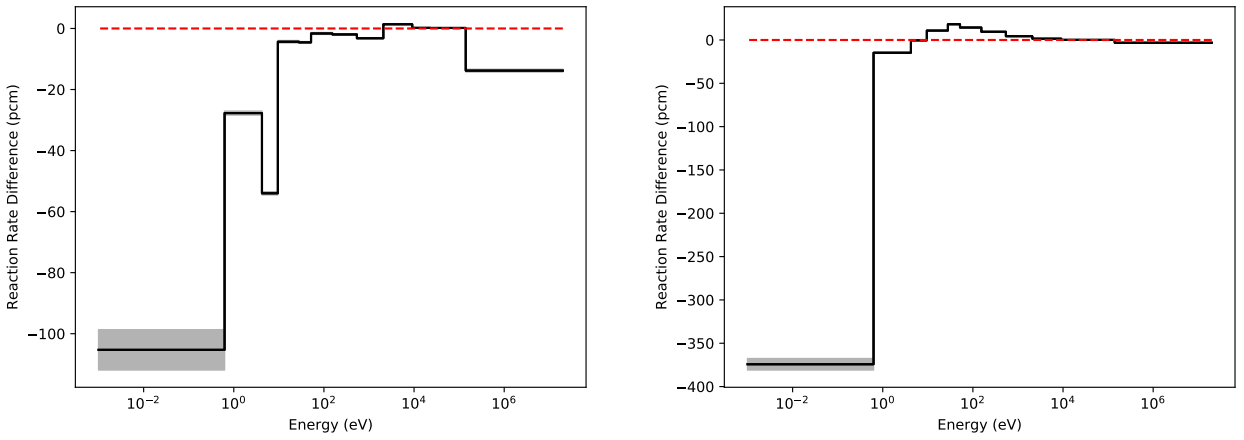

(a) MCD-FEDS fuel

(b) OCD-FEDS fuel

Figure 3.21: Fission errors in the whole fuel between MCNP and PDT for different types of cross section data (MCD-FEDS-166, SERPENT-SHEM- 166) with three regions in fuel with equal radius division for 2D pin cell problem (pcm in 95% condifence).

Table 3.24: Errors in integrated absorption rates for different types of cross section data (MCD-FEDS, SERPENT-SHEM) with three regions in fuel with equal radius division for 2D pin cell problem.

Method	11% fuel	22% fuel	11% fuel	22% fuel	14% fuel	15% fuel	5% fuel	fuel
MCD-FEDS-166	413	386	254	143	-112	-268	-1551	16
MCD-FEDS-195	141	175	114	94	-51	-150	-602	11
MCD-FEDS-244	58	106	60	63	-44	-102	-298	5
MCD-FEDS-361	18	74	38	54	-34	-71	-189	4
MCD-FEDS-417	11	68	34	51	-32	-68	-161	3
SERPENT-SHEM-166	-133	36	-588	4143	2907	-806	-18205	-137
SERPENT-SHEM-244	-254	-114	-575	2159	1490	-165	-10077	-148
SERPENT-SHEM-361	-179	-62	-346	674	174	-454	-2663	-152

Table 3.25: Errors in integrated fission rates for different types of cross section data (MCD-FEDS, SERPENT-SHEM) with three regions in fuel with equal radius division for 2D pin cell problem.

Method	11% fuel	22% fuel	11% fuel	22% fuel	14% fuel	15% fuel	5% fuel	fuel
MCD-FEDS-166	-227	-174	-197	-192	-239	-261	-279	-215
MCD-FEDS-195	-172	-112	-127	-114	-152	-163	-167	-137
MCD-FEDS-244	-53	8	-8	6	-31	-41	-45	-17
MCD-FEDS-361	-21	40	26	40	3	-8	-14	16
MCD-FEDS-417	-19	42	28	42	6	-4	-10	19
SERPENT-SHEM-166	-334	-278	-336	-285	-360	-408	-459	-334
SERPENT-SHEM-244	-213	-155	-196	-149	-210	-245	-283	-193
SERPENT-SHEM-361	-125	-64	-97	-56	-112	-142	-168	-97

Table 3.26: L1 errors in absorption rates for different types of cross section data (MCD-FEDS, SERPENT-SHEM) with three regions in fuel with equal radius division for 2D pin cell problem.

Method	11% fuel	22% fuel	11% fuel	22% fuel	14% fuel	15% fuel	5% fuel	fuel
MCD-FEDS-166	711	583	531	469	471	443	1648	453
MCD-FEDS-195	332	266	246	207	210	230	652	206
MCD-FEDS-244	201	242	215	212	224	225	365	209
MCD-FEDS-361	179	220	207	207	202	196	270	197
MCD-FEDS-417	174	216	203	203	197	193	245	197
SERPENT-SHEM-166	934	991	672	5060	3870	1649	18217	811
SERPENT-SHEM-244	612	639	602	2784	2164	1852	10089	515
SERPENT-SHEM-361	430	418	372	1112	675	733	2675	344

Table 3.27: L1 errors in fission rates for different types of cross section data (MCD-FEDS, SERPENT-SHEM) with three regions in fuel with equal radius division for 2D pin cell problem.

Method	11% fuel	22% fuel	11% fuel	22% fuel	14% fuel	15% fuel	5% fuel	fuel
MCD-FEDS-166	259	194	203	195	242	263	279	218
MCD-FEDS-195	192	128	140	123	156	167	171	146
MCD-FEDS-244	128	184	164	171	128	112	99	148
MCD-FEDS-361	114	172	156	167	129	115	105	144
MCD-FEDS-417	116	174	158	168	130	117	107	145
SERPENT-SHEM-166	524	457	458	436	449	459	488	452
SERPENT-SHEM-244	302	236	260	222	253	267	289	249
SERPENT-SHEM-361	172	107	128	93	127	151	172	123

Table 3.28: Errors in k_{eff} for different types of cross section data (MCD-FEDS, SERPENT- SHEM) with three regions in fuel with equal volume division for 2D pin cell problem.

Method	Unknowns (RRR)	K_{eff}	E_{pcm}	Efficiency $\frac{1}{\lvert Error \rvert \times DOF}$
MCD-FEDS-166	30	1.46086	-259 $\pm$1	12.9
MCD-FEDS-195	59	1.46198	-182 $\pm$1	9.3
MCD-FEDS-244	108	1.46373	-63 $\pm$1	14.8
MCD-FEDS-361	225	1.46421	-30 $\pm$1	14.8
MCD-FEDS-417	281	1.46425	-27 $\pm$1	13.0
SERPENT-SHEM-166	30	1.45913	-377 $\pm$1	8.8
SERPENT-SHEM-244	108	1.46117	-237 $\pm$1	3.9
SERPENT-SHEM-361	225	1.46257	-142 $\pm$1	3.1

3.1.4 Weighting FEDS Cross Sections with SERPENT

The FEDS discontiguous group structure is also applied in SERPENT for cross sections weighting. The results for k_{eff} for SERPENT-FEDS method for 2D pin cell problem is listed in Table 3.33. It is observed that SERPENT-FEDS method gives the best results for k_{eff} even with smallest number of unknowns.

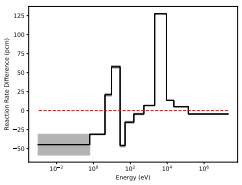

(a) M-11% fuel

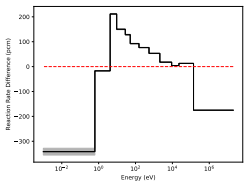

(b) S-11% fuel

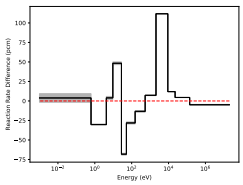

(c) M-22% fuel

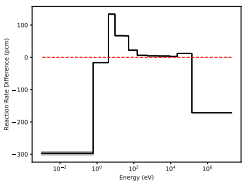

(d) S-22% fuel

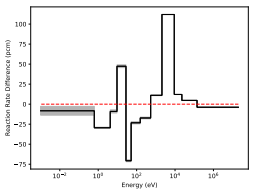

(e) M-11% fuel

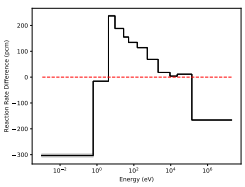

(f) S-11% fuel

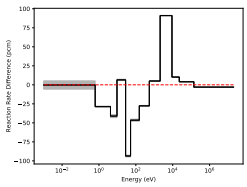

(g) M-22% fuel

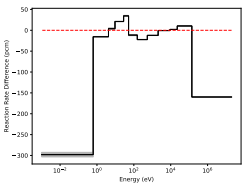

(h) S-22% fuel

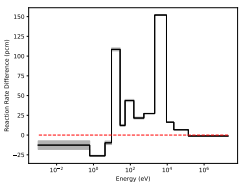

(i) M-19% fuel

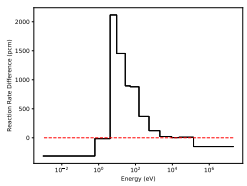

(j) S-19% fuel

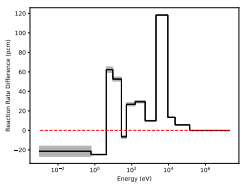

(k) M-15% fuel

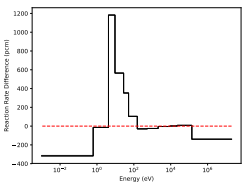

(l) S-15% fuel

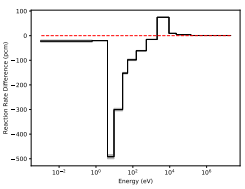

(m) M-5% fuel

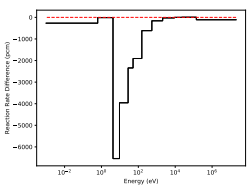

(n) S-5% fuel

Figure 3.22: Absorption errors in multiple regions of the fuel between MCNP and PDT for different types of cross section data (MCD-FEDS-166, SERPENT-SHEM-166) with three regions in fuel with equal volume division for 2D pin cell problem (pcm in 95% condifence). Columns have the same cross sections. Rows have the same QOIs.

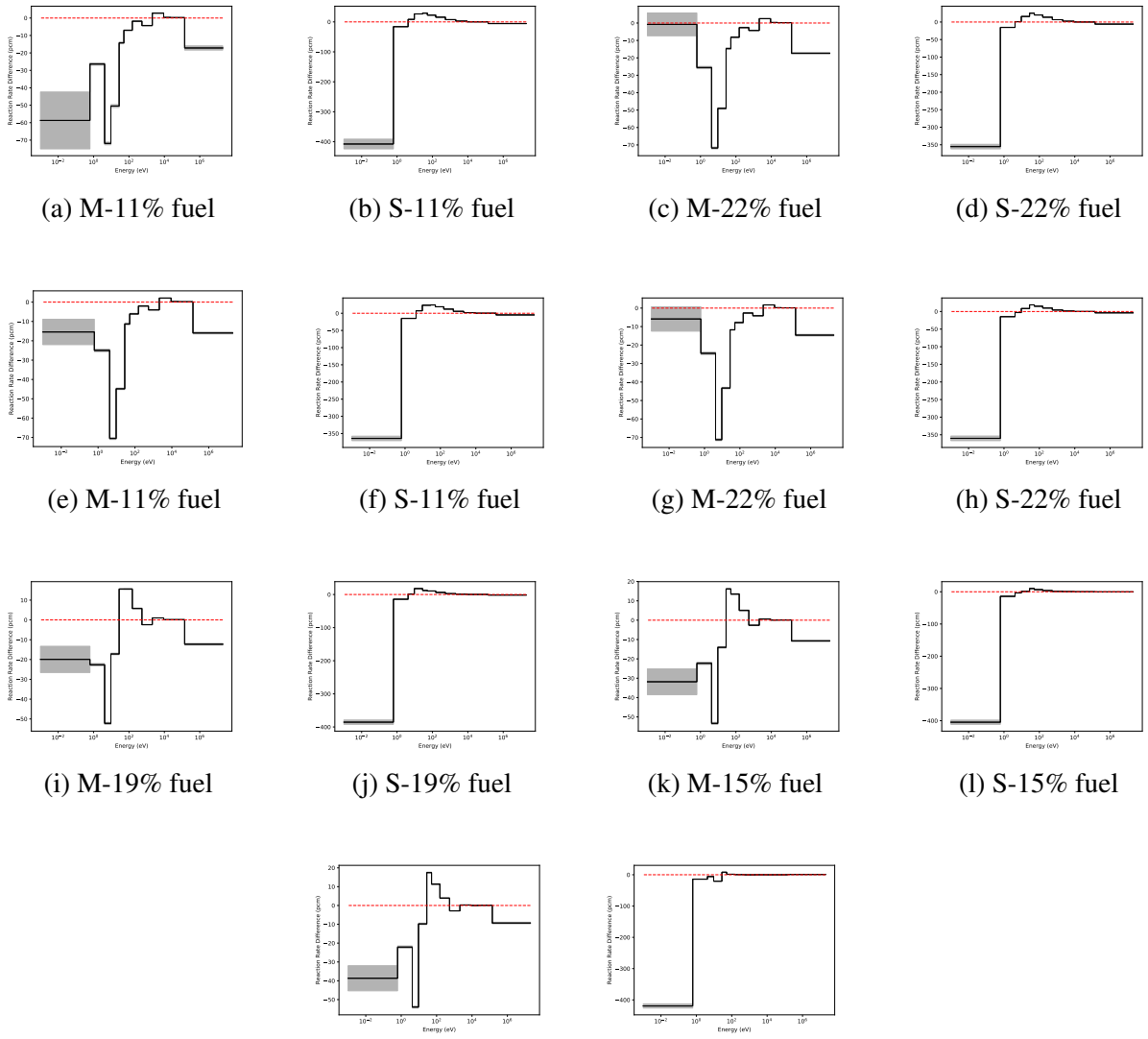

(a) M-11% fuel (b) S-11% fuel (c) M-22% fuel (d) S-22% fuel

(e) M-11% fuel (f) S-11% fuel (g) M-22% fuel (h) S-22% fuel

(i) M-19% fuel (j) S-19% fuel (k) M-15% fuel (l) S-15% fuel

(m) M-5% fuel (n) S-5% fuel

Figure 3.23: Fission errors in multiple regions of the fuel between MCNP and PDT for different types of cross section data (MCD-FEDS-166, SERPENT-SHEM-166) with three regions in fuel with equal volume division for 2D pin cell problem (pcm in 95% condifence). Columns have the same cross sections. Rows have the same QOIs.

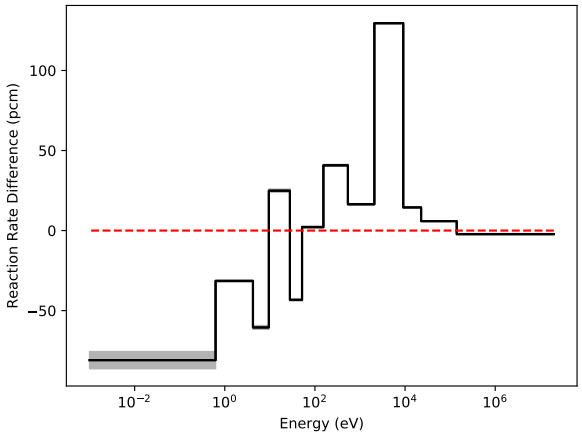

(a) MCD-FEDS fuel

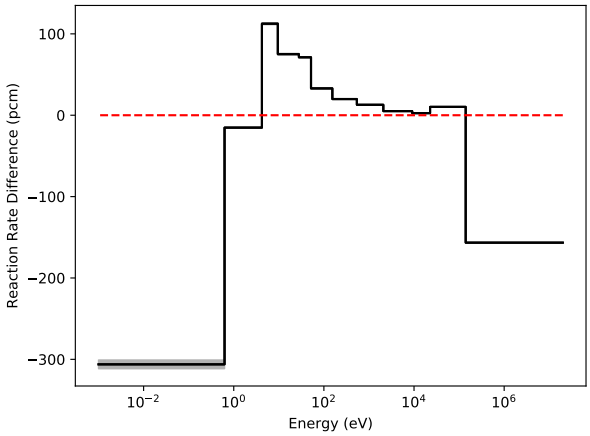

(b) OCD-FEDS fuel

Figure 3.24: Absorption errors in the whole fuel between MCNP and PDT for different types of cross section data (MCD-FEDS-166, SERPENT-SHEM-166) with three regions in fuel with equal volume division for 2D pin cell problem (pcm in 95% condifence).

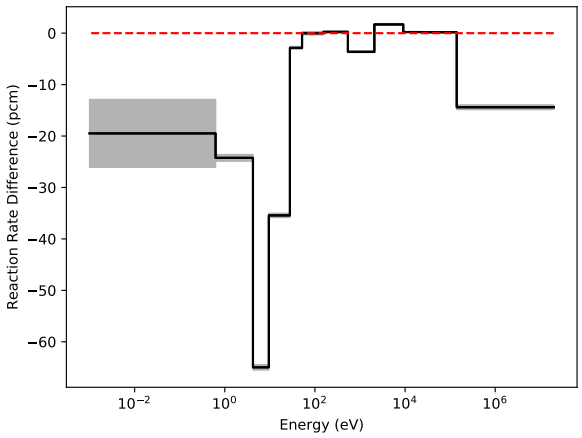

(a) MCD-FEDS fuel

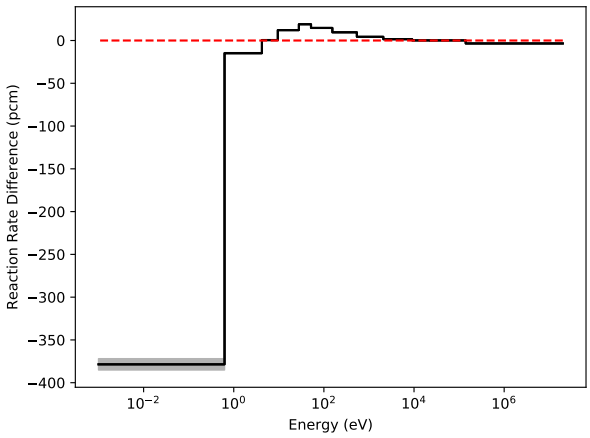

(b) OCD-FEDS fuel

Figure 3.25: Fission errors in the whole fuel between MCNP and PDT for different types of cross section data (MCD-FEDS-166, SERPENT-SHEM-166) with three regions in fuel with equal volume division for 2D pin cell problem (pcm in 95% condifence).

Table 3.29: Errors in absorption rates for different types of cross section data (MCD- FEDS, SERPENT-SHEM) with three regions in fuel with equal volume division for 2D pin cell problem.

Method	11% fuel	22% fuel	11% fuel	22% fuel	14% fuel	15% fuel	5% fuel	fuel
MCD-FEDS-166	85	47	25	-124	338	265	-1072	10
MCD-FEDS-195	-13	3	-12	-55	175	114	-317	7
MCD-FEDS-244	-32	9	-4	-13	95	36	-150	4
MCD-FEDS-361	-35	18	1	12	43	9	-111	3
MCD-FEDS-417	-35	20	3	17	38	2	-101	3
SERPENT-SHEM-166	213	-166	446	-448	5391	1685	-15929	-136
SERPENT-SHEM-244	-6	-230	216	-431	2720	1160	-8619	-145
SERPENT-SHEM-361	-49	-172	76	-272	632	11	-2182	-152

Table 3.30: Errors in fission rates for different types of cross section data (MCD- FEDS, SERPENT-SHEM) with three regions in fuel with equal volume division for 2D pin cell problem.

Method	11% fuel	22% fuel	11% fuel	22% fuel	14% fuel	15% fuel	5% fuel	fuel
MCD-FEDS-166	-249	-191	-193	-184	-88	-99	-104	-163
MCD-FEDS-195	-123	-69	-73	-68	23	6	-4	-47
MCD-FEDS-244	-65	-5	-12	0	48	38	34	5
MCD-FEDS-361	-27	33	24	36	60	50	45	33
MCD-FEDS-417	-34	26	17	29	48	38	33	24
SERPENT-SHEM-166	-316	-291	-290	-323	-349	-400	-449	-335
SERPENT-SHEM-244	-207	-169	-170	-185	-205	-240	-275	-199
SERPENT-SHEM-361	-119	-74	-78	-83	-103	-133	-158	-99

Table 3.31: L1 errors in absorption rates for different types of cross section data (MCD- FEDS, SERPENT-SHEM) with three regions in fuel with equal volume division for 2D pin cell problem.

Method	11% fuel	22% fuel	11% fuel	22% fuel	14% fuel	15% fuel	5% fuel	fuel
MCD-FEDS-166	378	336	349	358	438	371	1250	318
MCD-FEDS-195	161	214	209	240	250	195	388	187
MCD-FEDS-244	187	238	228	239	223	191	274	212
MCD-FEDS-361	189	230	224	221	222	207	255	214
MCD-FEDS-417	169	210	204	198	212	195	226	195
SERPENT-SHEM-166	1280	804	1416	592	6352	2742	15942	820
SERPENT-SHEM-244	791	459	896	456	3395	1938	8631	529
SERPENT-SHEM-361	546	321	566	297	1119	576	2194	346

Table 3.32: L1 errors in fission rates for different types of cross section data (MCD- FEDS, SERPENT-SHEM) with three regions in fuel with equal volume division for 2D pin cell problem.

Method	11% fuel	22% fuel	11% fuel	22% fuel	14% fuel	15% fuel	5% fuel	fuel
MCD-FEDS-166	255	197	198	188	165	170	170	167
MCD-FEDS-195	130	172	146	160	105	95	92	122
MCD-FEDS-244	147	204	182	190	149	132	123	162
MCD-FEDS-361	137	193	173	182	147	133	124	159
MCD-FEDS-417	125	182	162	170	137	124	114	148
SERPENT-SHEM-166	542	462	478	440	453	446	471	459
SERPENT-SHEM-244	309	248	253	242	251	264	280	257
SERPENT-SHEM-361	173	115	118	108	124	141	161	125

Table 3.33: Errors in k_{eff} for SERPENT-FEDS method for 2D pin cell problem.

Method	Unknowns (RRR)	K_{eff}	E_{pcm}	Efficiency $\frac{1}{\lvert Error \rvert \times DOF}$
NJOY-FEDS-166	30	1.46865	273±1	12.2
NJOY-FEDS-244	108	1.46663	135±1	6.9
NJOY-FEDS-361	225	1.46571	72±1	6.1
NJOY-SHEM-166	30	1.46875	280±1	11.9
NJOY-SHEM-244	108	1.46875	207±1	4.5
NJOY-SHEM-361	225	1.46410	-38±1	11.8
SERPENT-SHEM-166	30	1.46057	-279±1	11.9
SERPENT-SHEM-244	108	1.46250	-147±1	6.3
SERPENT-SHEM-361	225	1.46366	-68±1	6.6
SERPENT-FEDS-166	30	1.46394	-48±1	68.8
SERPENT-FEDS-244	108	1.46401	-42±1	22.0
SERPENT-FEDS-361	225	1.46398	-39±1	11.4

The errors in absorption and fission rates in 50%, 30%, 15%, 5% fuel regions for different types of cross sections for 166 groups are plotted in Figs.3.26-3.27, respectively. The errors in in absorption and fission rates for the whole fuel region for different types of cross sections for 166 groups are plotted in Figs.3.28, and 3.29, respectively. Errors in absorption rates and fission rate for different types of cross section data for different unknown numbers are summarized in Tables 3.34-3.35, respectively . L1 errors in absorption rates and fission rates for different types of cross section data for different unknown numbers are summarized in Tables 3.36-3.37.

After applying the FEDS discontiguous group structure in SERPENT, it greatly reduce the

absorption errors in the RRR region: the maximum absorption error in RRR for 166 groups drops from about 8000 pcm to 400 pcm in the outer 5% fuel region. And there is also reduction in the absorption and fission errors in the thermal range. It is also observed that SERPENT-FEDS method give the smallest L1 errors in the absorption and fission rate for the whole fuel.

Table 3.34: Errors in integrated absorption rate for SERPENT-FEDS method for 2D pin cell problem.

Method	50% fuel	30% fuel	15% fuel	5% fuel	fuel
NJOY-FEDS-166	283	25	-323	-1612	-22
NJOY-FEDS-244	85	-11	-140	-336	-10
NJOY-FEDS-361	45	-9	-76	-155	-5
NJOY-SHEM-166	2833	1590	-2701	-19864	14
NJOY-SHEM-244	1487	893	-1166	-11080	22
NJOY-SHEM-361	734	95	-813	-2998	36
SERPENT-SHEM-166	2755	1419	-2971	-20161	-138
SERPENT-SHEM-244	1360	732	-1423	-11392	-149
SERPENT-SHEM-361	533	-94	-979	-3141	-152
SERPENT-FEDS-166	143	-110	-483	-1600	-154
SERPENT-FEDS-244	128	-91	-412	-1087	-155
SERPENT-FEDS-361	117	-77	-358	-996	-157

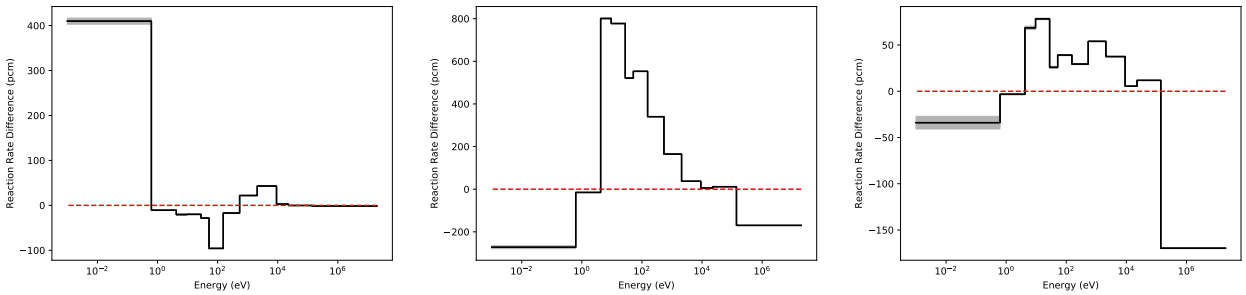

(a) NJOY-FEDS-50% fuel (b) SERPENT-SHEM-50% fuel (c) SERPENT-FEDS-50% fuel

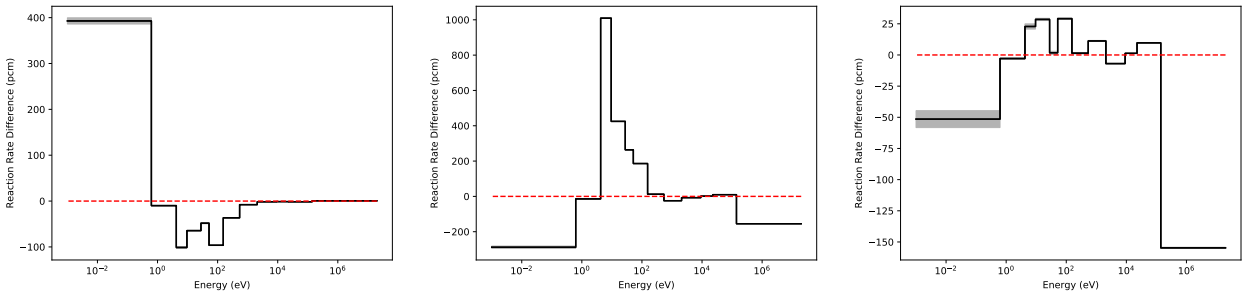

(d) NJOY-FEDS-30% fuel (e) SERPENT-SHEM-30% fuel (f) SERPENT-FEDS-30% fuel

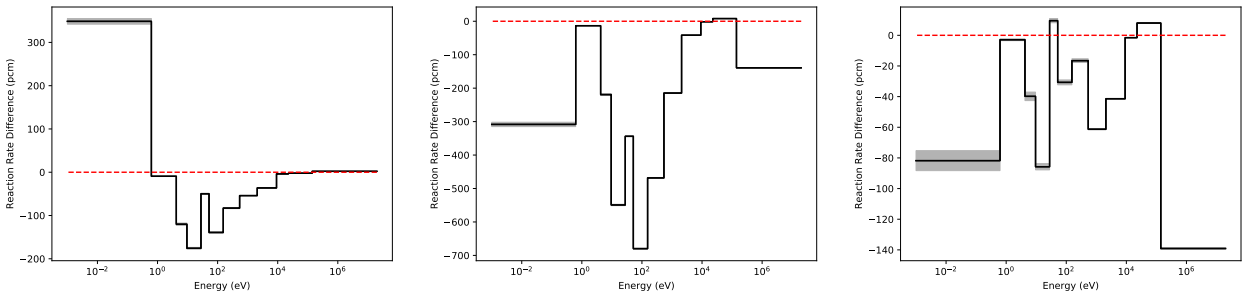

(g) NJOY-FEDS-15% fuel (h) SERPENT-SHEM-15% fuel (i) SERPENT-FEDS-15% fuel

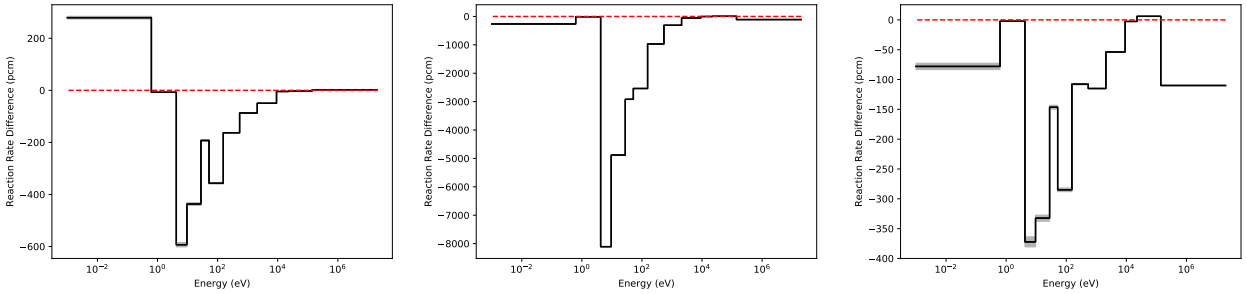

(j) NJOY-FEDS-5% fuel (k) SERPENT-SHEM-5% fuel (l) SERPENT-FEDS-5% fuel

Figure 3.26: Absorption errors in multiple regions of the fuel between MCNP and PDT for different types of cross section data (NJOY-FEDS-166, SERPENT-SHEM-166, SERPENT-FEDS-166) for 2D pin cell problem (pcm in 95% condifence). Columns have the same cross sections. Rows have the same QOIs.

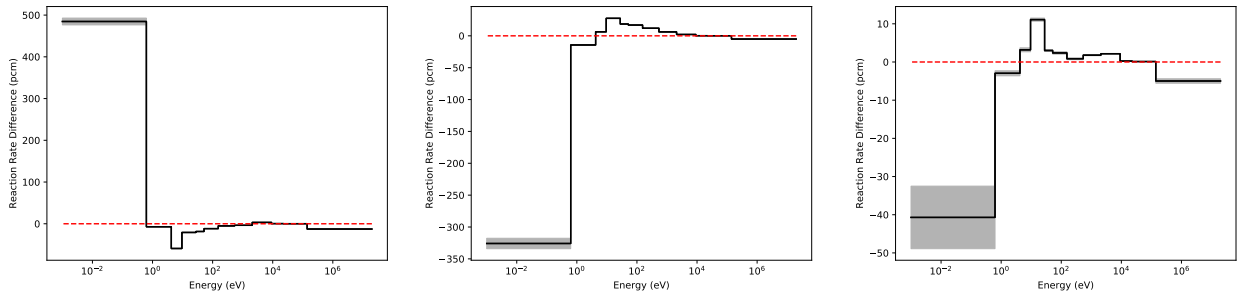

(a) NJOY-FEDS-50% fuel (b) SERPENT-SHEM-50% fuel (c) SERPENT-FEDS-50% fuel

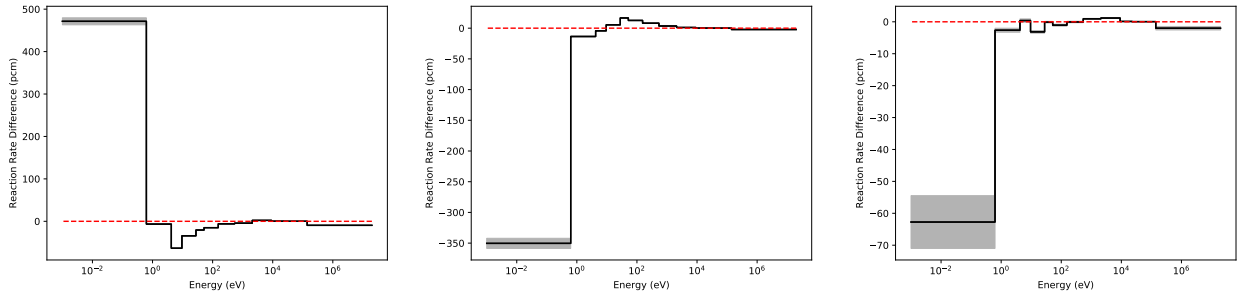

(d) NJOY-FEDS-30% fuel (e) SERPENT-SHEM-30% fuel (f) SERPENT-FEDS-30% fuel

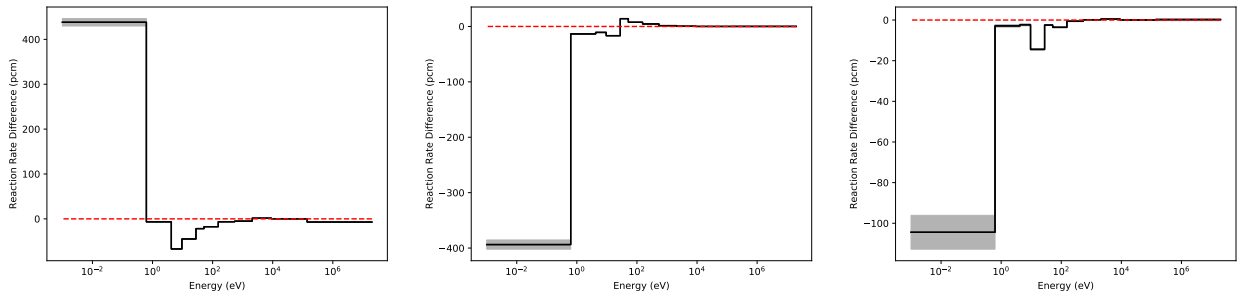

(g) NJOY-FEDS-15% fuel (h) SERPENT-SHEM-15% fuel (i) SERPENT-FEDS-15% fuel

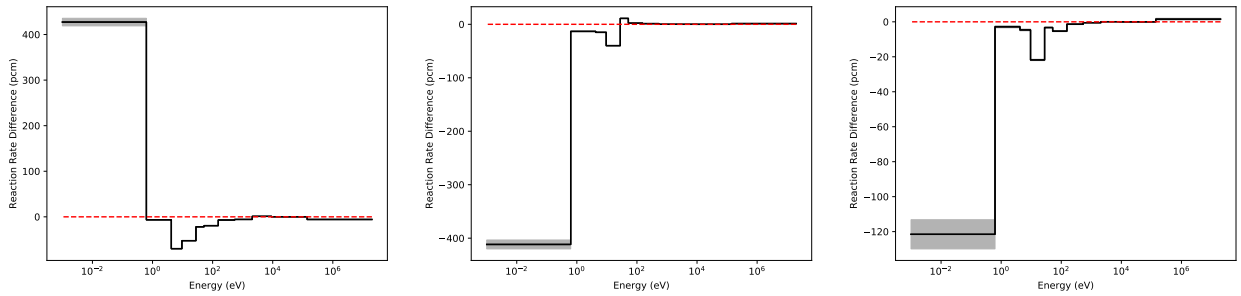

(j) NJOY-FEDS-5% fuel (k) SERPENT-SHEM-5% fuel (l) SERPENT-FEDS-5% fuel

Figure 3.27: Fission errors in multiple regions of the fuel between MCNP and PDT for different types of cross section data (NJOY-FEDS-166, SERPENT-SHEM-166, SERPENT-FEDS-166) for 2D pin cell problem (pcm in 95% condifence). Columns have the same cross sections. Rows have the same QOIs.

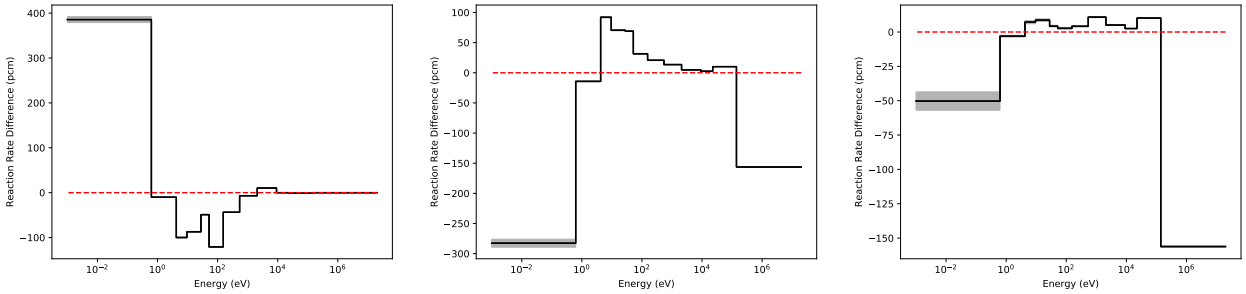

(a) NJOY-FEDS fuel (b) SERPENT-SHEM fuel (c) SERPENT-FEDS fuel

Figure 3.28: Absorption errors in the whole fuel between MCNP and PDT for different types of cross section data (NJOY-FEDS-166, SERPENT-SHEM-166, SERPENT-FEDS-166) for 2D pin cell problem (pcm in 95% condifence).

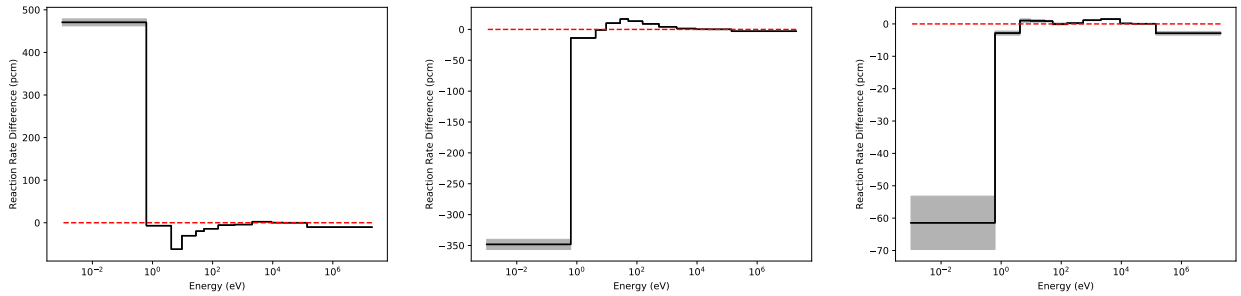

(a) NJOY-FEDS fuel (b) SERPENT-SHEM fuel (c) SERPENT-FEDS fuel

Figure 3.29: Fission errors in the whole fuel between MCNP and PDT for different types of cross section data (NJOY-FEDS-166, SERPENT-SHEM-166, SERPENT-FEDS-166) for 2D pin cell problem (pcm in 95% condifence).

Table 3.35: Errors in integrated fission rate for SERPENT-FEDS method for 2D pin cell problem.

Method	50% fuel	30% fuel	15% fuel	5% fuel	fuel
NJOY-FEDS-166	350	314	263	240	320
NJOY-FEDS-244	195	180	147	138	180
NJOY-FEDS-361	130	118	86	77	117
NJOY-SHEM-166	365	300	219	163	312
NJOY-SHEM-244	274	231	171	134	237
NJOY-SHEM-361	22	-12	-62	-84	-7
SERPENT-SHEM-166	-255	-323	-406	-464	-311
SERPENT-SHEM-244	-133	-183	-250	-294	-175
SERPENT-SHEM-361	-57	-100	-159	-188	-93
SERPENT-FEDS-166	-24	-69	-130	-160	-61
SERPENT-FEDS-244	-23	-72	-126	-166	-64
SERPENT-FEDS-361	-25	-67	-134	-156	-64

Table 3.36: L1 errors in absorption rate for SERPENT-FEDS method for 2D pin cell problem.

Method	50% fuel	30% fuel	15% fuel	5% fuel	fuel
NJOY-FEDS-166	672	762	1024	2175	814
NJOY-FEDS-244	439	470	523	636	460
NJOY-FEDS-361	330	341	340	358	329
NJOY-SHEM-166	2857	2070	3382	20410	1116
NJOY-SHEM-244	1519	1180	2413	11482	624
NJOY-SHEM-361	883	310	1010	3120	268
SERPENT-SHEM-166	3669	2396	2987	20173	768
SERPENT-SHEM-244	1995	1432	2196	11403	485
SERPENT-SHEM-361	1005	446	1125	3153	334
SERPENT-FEDS-166	557	322	518	1612	265
SERPENT-FEDS-244	438	220	390	1126	246
SERPENT-FEDS-361	403	220	367	1088	221

Table 3.37: L1 errors in fission rate for SERPENT-FEDS method for 2D pin cell problem.

Method	50% fuel	30% fuel	15% fuel	5% fuel	fuel
NJOY-FEDS-166	627	634	617	617	627
NJOY-FEDS-244	375	359	323	309	359
NJOY-FEDS-361	292	272	234	219	273
NJOY-SHEM-166	669	676	660	662	670
NJOY-SHEM-244	430	438	427	442	431
NJOY-SHEM-361	251	247	225	223	244
SERPENT-SHEM-166	435	418	463	496	421
SERPENT-SHEM-244	226	229	272	301	228
SERPENT-SHEM-361	109	120	170	193	117
SERPENT-FEDS-166	73	74	132	163	73
SERPENT-FEDS-244	72	78	128	169	76
SERPENT-FEDS-361	76	73	135	159	76

We also tested the SERPENT-FEDS method for two regions in the fuel for cross section generation for 166 groups. The errors in absorption and fission rates in 50%, 30%, 15%, 5% fuel regions for different types of cross sections for 166 groups are plotted in Figs.**??**, 3.34, 3.31 and 3.35, respectively. The errors in in absorption and fission rates for the whole fuel region for different types of cross sections for 166 groups are plotted in Figs.3.32, 3.36, 3.33 and 3.37, respectively. Errors in absorption rates and fission rate for different types of cross section data are summarized in Tables 3.38-3.39, respectively . L1 errors in absorption rates and fission rates for different types of cross section data for are summarized in Tables 3.40-3.41, respectively. Similar results are observed in this two region calculation: SERPENT-FEDS method performs better in EV division than in ER

division. In addition, SERPENT-FEDS give the smallest value in L1 errors in absorption rates in the outer 5% fuel region and gives the best results for the absorption and fission rate in the whole fuel regions.

Table 3.38: Errors in integrated absorption rates for different types of cross section data (MCD-FEDS, OCD-FEDS, SERPENT-SHEM, SERPENT-FEDS) with two regions in fuel for 2D pin cell problem.

Method	25% fuel	25% fuel	30% fuel	15% fuel	5% fuel	fuel
ER-MCD-FEDS-166	372	240	9	-210	-1634	0
EV-MCD-FEDS-166	26	-123	274	177	-1195	7
ER-OCD-FEDS-166	514	114	-52	-209	-1578	-11
EV-OCD-FEDS-166	163	41	114	75	-1540	-11
ER-SERPENT-SHEM-166	-240	3559	2355	-1985	-19271	-133
EV-SERPENT-SHEM-166	263	-538	3983	-333	-17771	-132
ER-SERPENT-FEDS-166	-184	216	-12	-357	-1465	-152
EV-SERPENT-FEDS-166	-44	-255	125	-196	-1282	-152

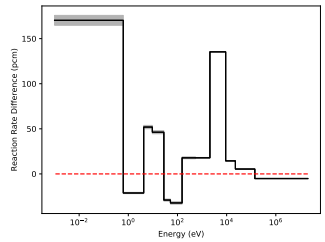

(a) MCD-FEDS-25% fuel

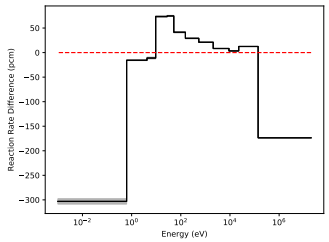

(b) SERPENT-SHEM-25% fuel

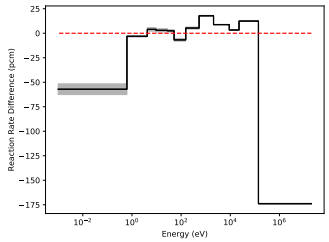

(c) SERPENT-FEDS-25% fuel

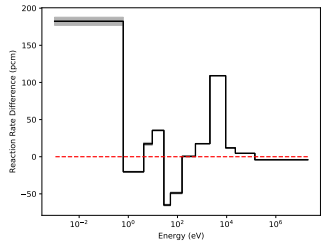

(d) MCD-FEDS-25% fuel

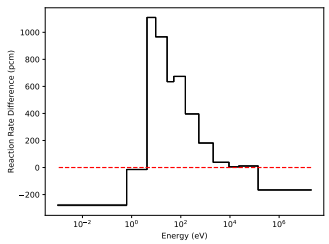

(e) SERPENT-SHEM-25% fuel

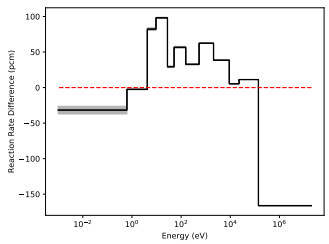

(f) SERPENT-FEDS-25% fuel

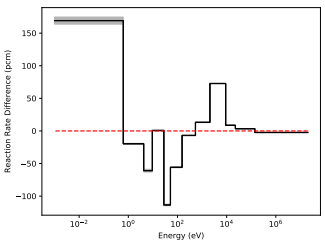

(g) MCD-FEDS-30% fuel

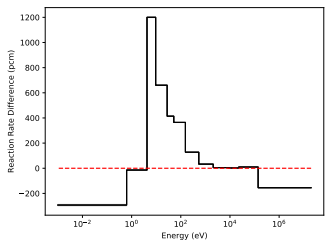

(h) SERPENT-SHEM-30% fuel

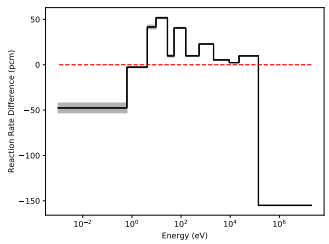

(i) SERPENT-FEDS-30% fuel

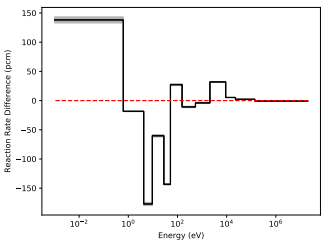

(j) MCD-FEDS-15% fuel

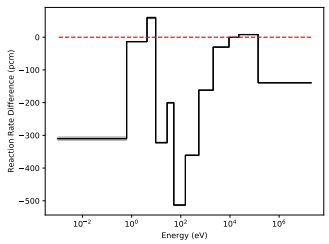

(k) SERPENT-SHEM-15% fuel

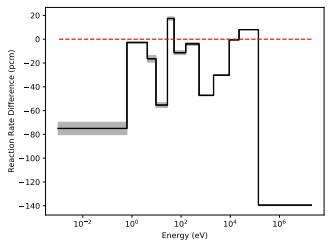

(l) SERPENT-FEDS-15% fuel

Figure 3.30: Absorption errors in multiple regions of the fuel between MCNP and PDT for different types of cross section data (MCD-FEDS-166, SERPENT-SHEM-166, SERPENT-FEDS-166) with two regions in fuel with equal radius division for for 2D pin cell problem (pcm in 95% condifence). Columns have the same cross sections. Rows have the same QOIs.

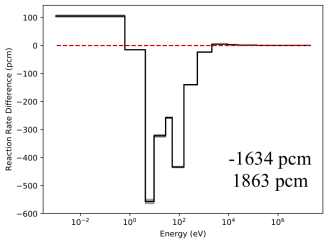

(m) MCD-FEDS-5% fuel

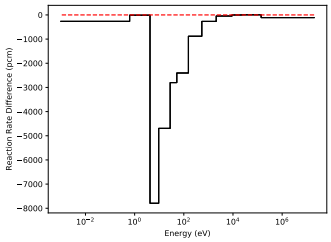

(n) SERPENT-SHEM-5% fuel

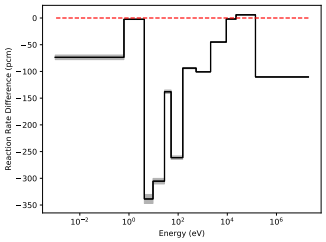

(o) SERPENT-FEDS-5% fuel

Figure 3.30: Continued.

Table 3.39: Errors in integrated fission rates for different types of cross section data (MCD-FEDS, OCD-FEDS, SERPENT-SHEM, SERPENT-FEDS) with two regions in fuel for 2D pin cell problem.

Method	25% fuel	25% fuel	30% fuel	15% fuel	5% fuel	fuel
ER-MCD-FEDS-166	86	93	69	28	7	69
EV-MCD-FEDS-166	-69	-65	17	-24	-42	-33
ER-OCD-FEDS-166	308	258	227	179	154	243
EV-OCD-FEDS-166	245	247	263	216	193	244
ER-SERPENT-SHEM-166	-303	-260	-321	-401	-459	-322
EV-SERPENT-SHEM-166	-283	-323	-317	-399	-454	-331
ER-SERPENT-FEDS-166	-65	-20	-59	-116	-147	-65
EV-SERPENT-FEDS-166	-56	-64	-50	-106	-137	-68

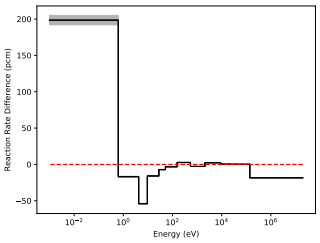

(a) MCD-FEDS-25% fuel

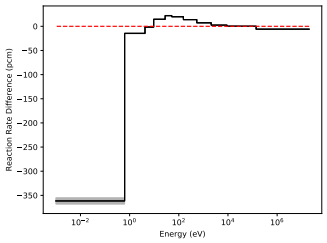

(b) SERPENT-SHEM-25% fuel

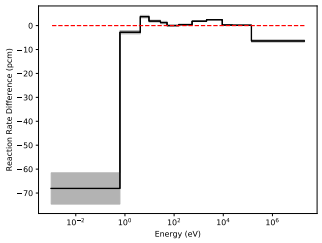

(c) SERPENT-FEDS-25% fuel

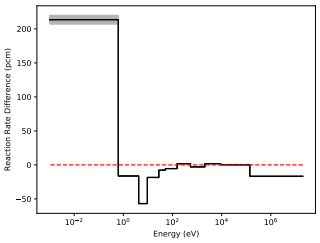

(d) MCD-FEDS-25% fuel

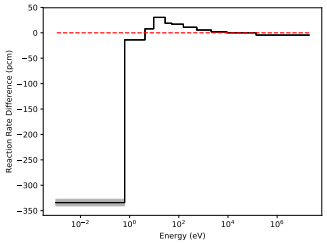

(e) SERPENT-SHEM-25% fuel

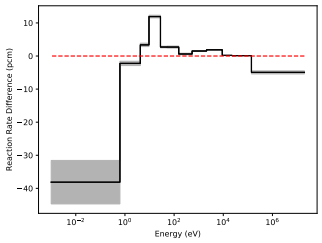

(f) SERPENT-FEDS-25% fuel

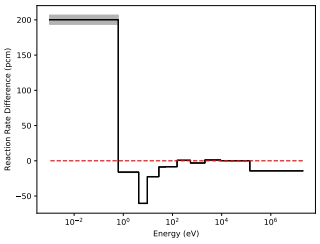

(g) MCD-FEDS-30% fuel

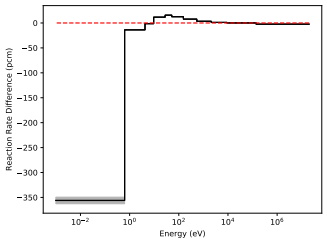

(h) SERPENT-SHEM-30% fuel

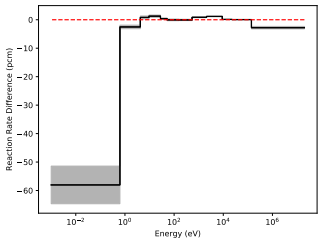

(i) SERPENT-FEDS-30% fuel

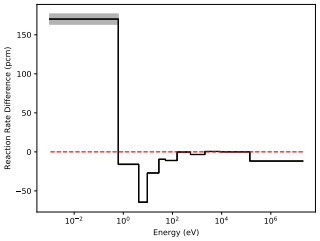

(j) MCD-FEDS-15% fuel

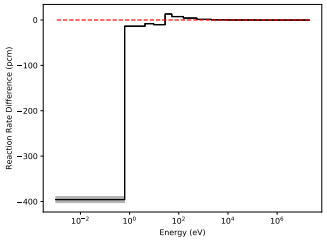

(k) SERPENT-SHEM-15% fuel

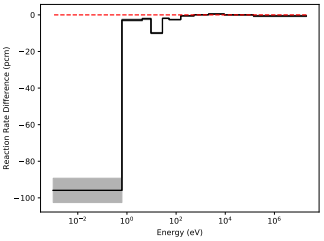

(l) SERPENT-FEDS-15% fuel

Figure 3.31: Fission errors in multiple regions of the fuel between MCNP and PDT for different types of cross section data (MCD-FEDS-166, SERPENT-SHEM-166, SERPENT-FEDS-166) with two regions in fuel with equal radius division for for 2D pin cell problem (pcm in 95% condifence). Columns have the same cross sections. Rows have the same QOIs.

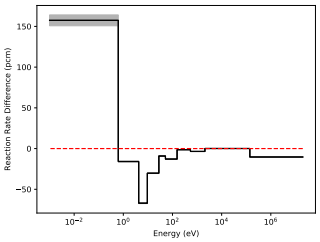

(m) MCD-FEDS-5% fuel

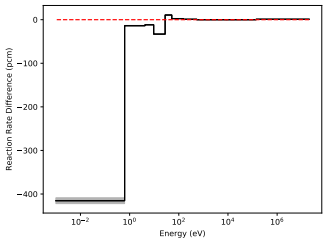

(n) SERPENT-SHEM-5% fuel

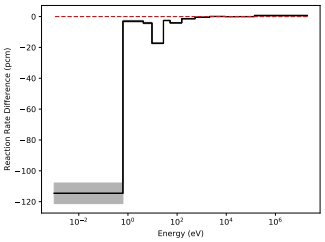

(o) SERPENT-FEDS-5% fuel

Figure 3.31: Continued.

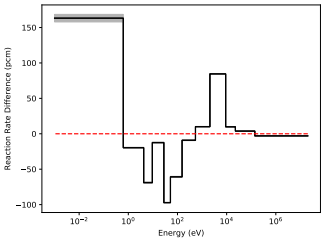

(a) MCD-FEDS fuel

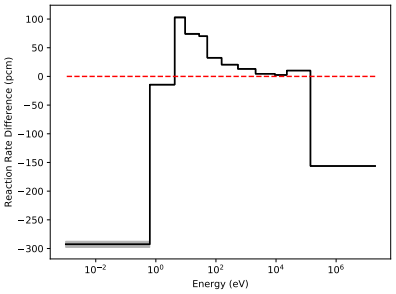

(b) SERPENT-SHEM fuel

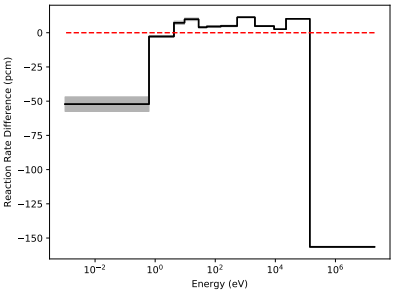

(c) SERPENT-FEDS fuel

Figure 3.32: Absorption errors in the whole fuel between MCNP and PDT for different types of cross section data (MCD-FEDS-166, SERPENT-SHEM-166, SERPENT-FEDS-166) with two regions in fuel with equal radius division for for 2D pin cell problem (pcm in 95% condifence).

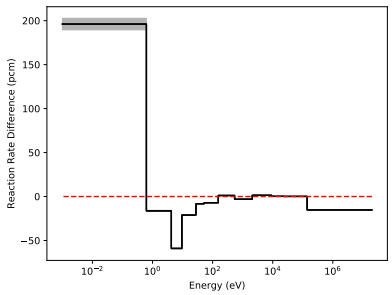

(a) MCD-FEDS fuel

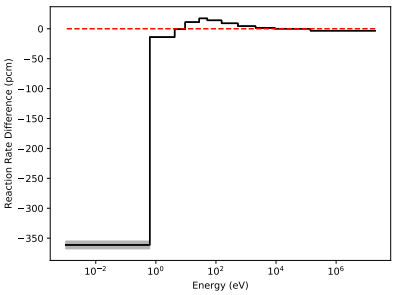

(b) SERPENT-SHEM fuel

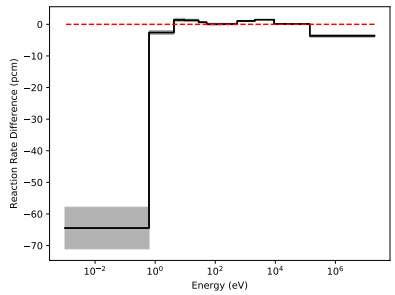

(c) SERPENT-FEDS fuel

Figure 3.33: Fission errors in the whole fuel between MCNP and PDT for different types of cross section data (MCD-FEDS-166, SERPENT-SHEM-166, SERPENT-FEDS-166) with two regions in fuel with equal radius division for for 2D pin cell problem (pcm in 95% condifence).

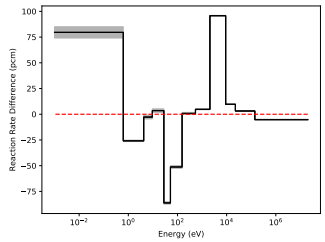

(a) MCD-FEDS-25% fuel

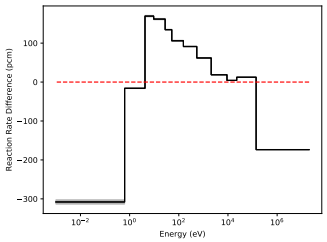

(b) SERPENT-SHEM-25% fuel

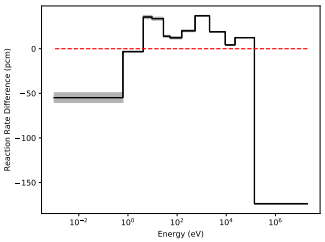

(c) SERPENT-FEDS-25% fuel

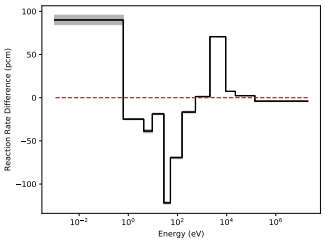

(d) MCD-FEDS-25% fuel

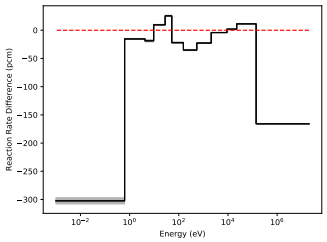

(e) SERPENT-SHEM-25% fuel

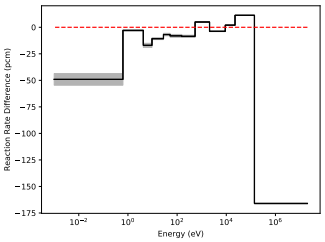

(f) SERPENT-FEDS-25% fuel

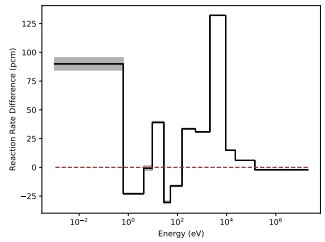

(g) MCD-FEDS-30% fuel

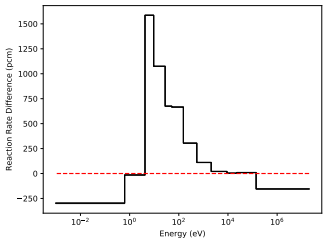

(h) SERPENT-SHEM-30% fuel

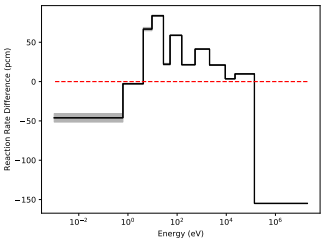

(i) SERPENT-FEDS-30% fuel

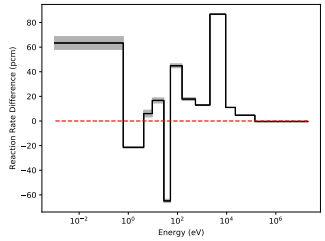

(j) MCD-FEDS-15% fuel

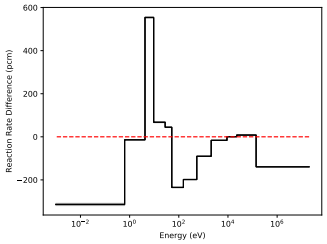

(k) SERPENT-SHEM-15% fuel

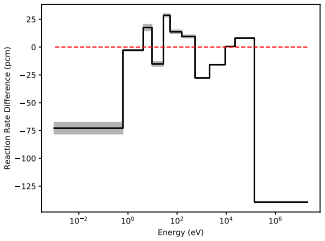

(l) SERPENT-FEDS-15% fuel

Figure 3.34: Absorption errors in multiple regions of the fuel between MCNP and PDT for different types of cross section data (MCD-FEDS-166, SERPENT-SHEM-166, SERPENT-FEDS-166) with two regions in fuel with equal volume division for for 2D pin cell problem (pcm in 95% condifence). Columns have the same cross sections. Rows have the same QOIs.

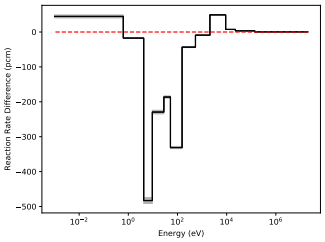

(m) MCD-FEDS-5% fuel

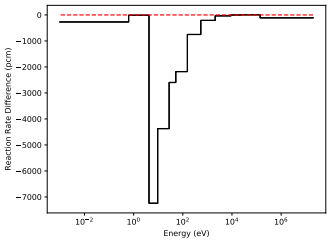

(n) SERPENT-SHEM-5% fuel

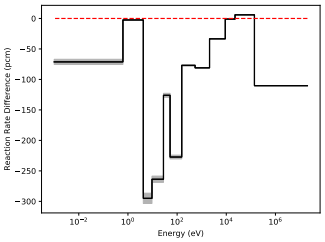

(o) SERPENT- FEDS-5% fuel

Figure 3.34: Continued.

Table 3.40: L1 errors in integrated absorption rates for different types of cross section data (MCD-FEDS, OCD-FEDS, SERPENT-SHEM, SERPENT-FEDS) with two regions in fuel for 2D pin cell problem.

Method	25% fuel	25% fuel	30% fuel	15% fuel	5% fuel	fuel
ER-MCD-FEDS-166	547	517	527	619	1863	542
EV-MCD-FEDS-166	369	466	419	351	1404	412
ER-OCD-FEDS-166	683	707	757	763	2016	752
EV-OCD-FEDS-166	585	700	624	559	1985	699
ER-SERPENT-SHEM-166	767	4477	3279	2120	19283	794
EV-SERPENT-SHEM-166	1258	635	4918	1682	17783	814
ER-SERPENT-FEDS-166	298	617	399	408	1477	271
EV-SERPENT-FEDS-166	420	291	532	352	1294	276

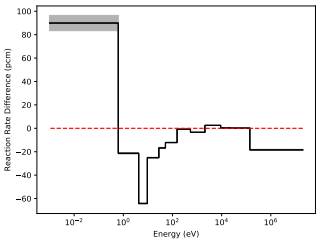

(a) MCD-FEDS-25% fuel

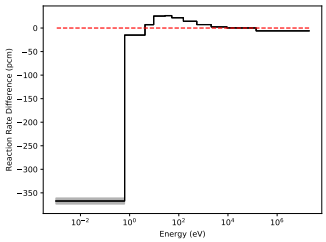

(b) SERPENT-SHEM-25% fuel

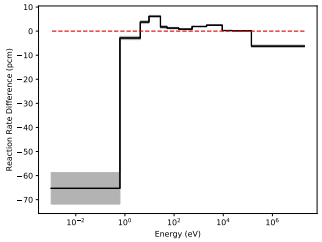

(c) SERPENT-FEDS-25% fuel

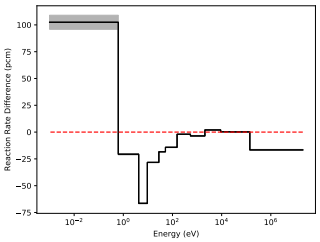

(d) MCD-FEDS-25% fuel

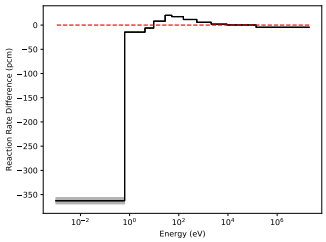

(e) SERPENT-SHEM-25% fuel

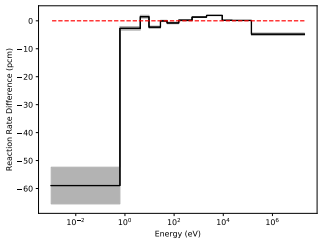

(f) SERPENT-FEDS-25% fuel

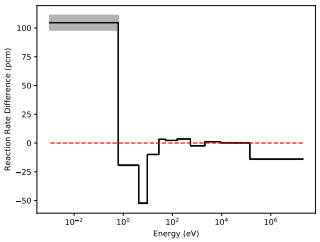

(g) MCD-FEDS-30% fuel

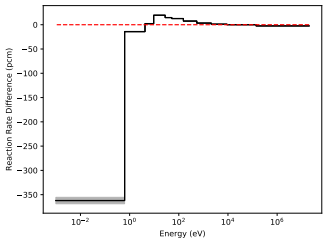

(h) SERPENT-SHEM-30% fuel

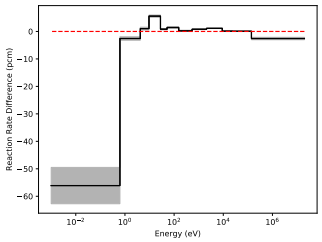

(i) SERPENT-FEDS-30% fuel

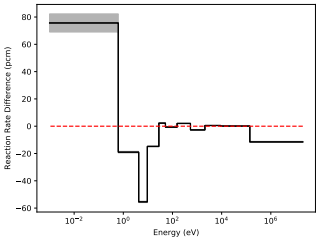

(j) MCD-FEDS-15% fuel

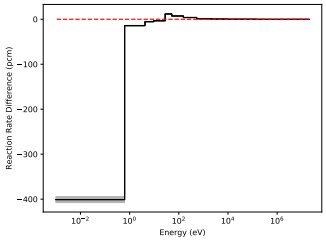

(k) SERPENT-SEHM-15% fuel

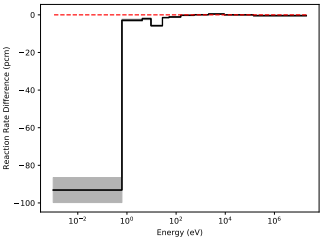

(l) SERPENT-FEDS-15% fuel

Figure 3.35: Fission errors in multiple regions of the fuel between MCNP and PDT for different types of cross section data (MCD-FEDS-166, SERPENT-SHEM-166, SERPENT-FEDS-166) with two regions in fuel with equal volume division for for 2D pin cell problem (pcm in 95% condifence). Columns have the same cross sections. Rows have the same QOIs.

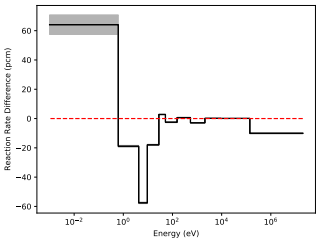

(m) MCD-FEDS-5% fuel

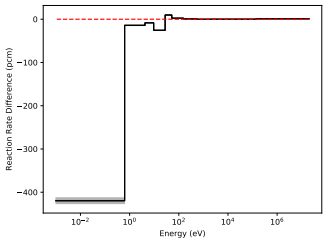

(n) SERPENT-SHEM-5% fuel

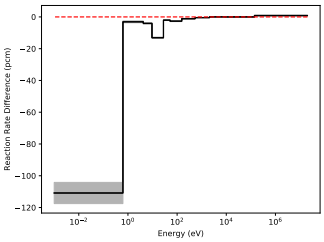

(o) SERPENT-FEDS-5% fuel

Figure 3.35: Continued.

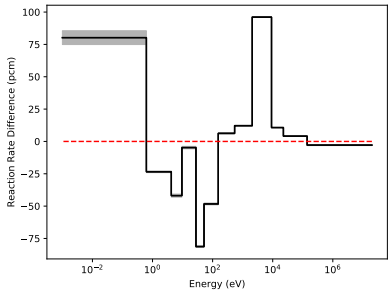

(a) MCD-FEDS fuel

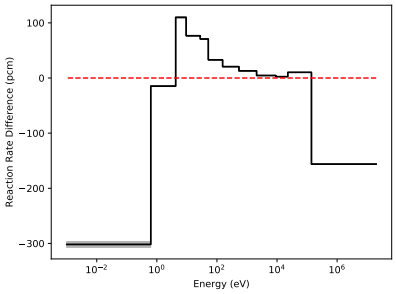

(b) SERPENT-SHEM fuel

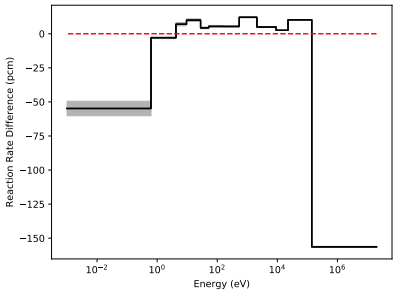

(c) SERPENT-FEDS fuel

Figure 3.36: Absorption errors in the whole fuel between MCNP and PDT for different types of cross section data (MCD-FEDS-166, SERPENT-SHEM-166, SERPENT-FEDS-166) with two regions in fuel with equal volume division for for 2D pin cell problem (pcm in 95% condifence).

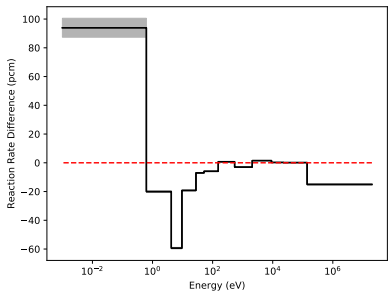

(a) MCD-FEDS fuel

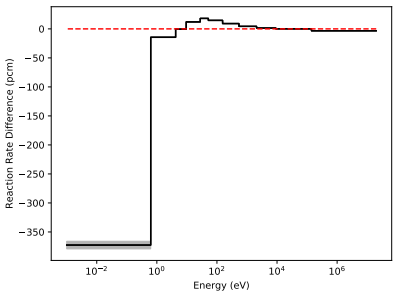

(b) SERPENT-SHEM fuel

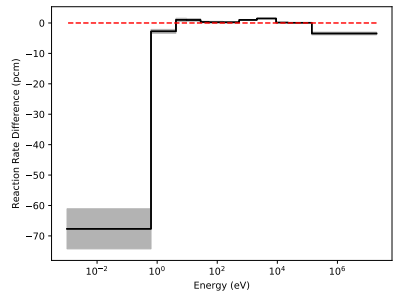

(c) SERPENT-FEDS fuel

Figure 3.37: Fission errors in the whole fuel between MCNP and PDT for different types of cross section data (MCD-FEDS-166, SERPENT-SHEM-166, SERPENT-FEDS-166) with two regions in fuel with equal volume division for for 2D pin cell problem (pcm in 95% condifence).

Table 3.41: L1 errors in integrated fission rates for different types of cross section data (MCD-FEDS, OCD-FEDS, SERPENT-SHEM, SERPENT-FEDS) with two regions in fuel for 2D pin cell problem.

Method	25% fuel	25% fuel	30% fuel	15% fuel	5% fuel	fuel
ER-MCD-FEDS-166	322	342	336	314	308	329
EV-MCD-FEDS-166	255	275	213	185	178	226
ER-OCD-FEDS-166	465	527	530	517	515	509
EV-OCD-FEDS-166	488	515	484	471	469	490
ER-SERPENT-SHEM-166	464	445	426	455	489	437
EV-SERPENT-SHEM-166	494	453	440	449	482	451
EV-SERPENT-FEDS-166	89	70	68	117	148	77
ER-SERPENT-FEDS-166	93	75	72	108	138	79

Moreover, calculations are performed for the four regions in the fuel for cross sections generation. The results for k_{eff} for different type of cross sections for 2D pin cell problem is listed in Table 3.42. It is noticed that NJOY-SHEM method gives much worse results than the ones in the single ring calculation. This may be mainly caused by that the approximate weighting spectrum in NJOY code doesn't work for the multiple fuel rings case. In order to exclude the possibility of a code bug, we further test the case for infinite medium problem with NJOY-SHEM cross sections, and the results are listed in Appendix.

Table 3.42: Errors in k_{eff} for different types of cross sections (NJOY-FEDS,NJOY-SHEM, SERPENT-SHEM, SERPENT-FEDS) with four regions in fuel for 2D pin cell problem.

Method	Unknowns (RRR)	K_{eff}	E_{pcm}	Efficiency $\frac{1}{\lvert Error \rvert \times DOF}$
NJOY-FEDS-166	30	1.46047	-286 $\pm$1	-8.0
NJOY-FEDS-244	108	1.46435	-20 $\pm$1	-7.2
NJOY-FEDS-361	225	1.46449	-11 $\pm$1	-4.2
NJOY-SHEM-166	30	1.41018	-3719 $\pm$1	-8.0
NJOY-SHEM-244	108	1.43766	-1843 $\pm$1	-7.2
NJOY-SHEM-361	225	1.44718	-1193 $\pm$1	-4.2
SERPENT-SHEM-166	30	1.45927	-367 $\pm$1	-8.0
SERPENT-SHEM-244	108	1.46100	-249 $\pm$1	-7.2
SERPENT-SHEM-361	225	1.46260	-141 $\pm$1	-4.2
SERPENT-FEDS-166	30	1.46361	-71 $\pm$1	-8.0
SERPENT-FEDS-244	108	1.46380	-58 $\pm$1	-7.2
SERPENT-FEDS-361	225	1.46377	-60 $\pm$1	-4.2

The errors in absorption and fission rates in 50%, 30%, 15%, 5% fuel regions for different types of cross sections for 166 groups are plotted in Figs.3.38 and 3.39, respectively. The errors in in absorption and fission rates for the whole fuel region for different types of cross sections for 166 groups are plotted in Figs.3.40, and 3.40, respectively. Errors in absorption rates and fission rate for different types of cross section data are summarized in Tables 3.43-3.44, respectively . L1 errors in absorption rates and fission rates for different types of cross section data for are summarized in Tables 3.45-3.46, respectively.

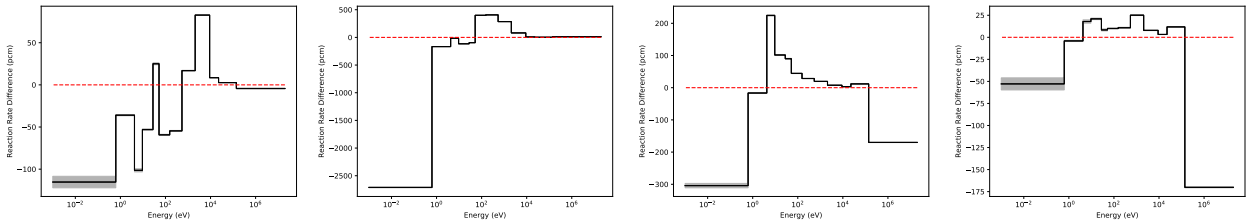

(a) NJOY-FEDS-50% fuel (b) NJOY-SHEM-50% fuel (c) SERPENT-SHEM-50% fuel (d) SERPENT-FEDS-50% fuel

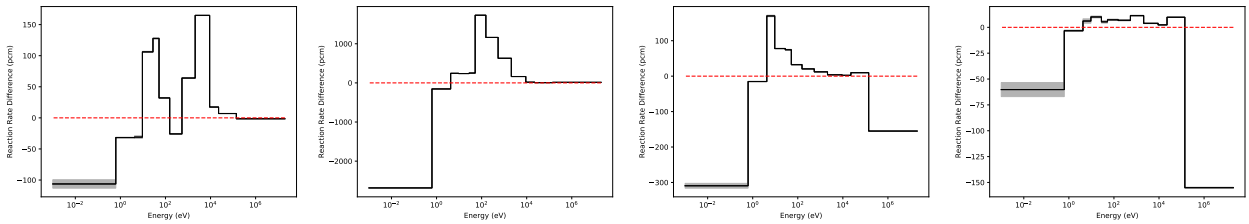

(e) NJOY-FEDS-30% fuel (f) NJOY-SHEM-30% fuel (g) SERPENT-SHEM-30% fuel (h) SERPENT-FEDS-30% fuel

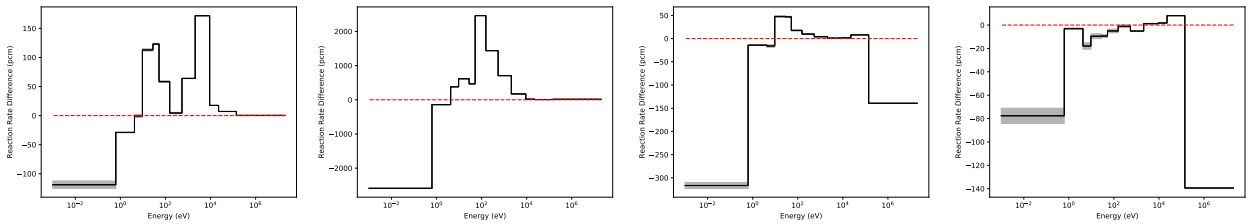

(i) NJOY-FEDS-15% fuel (j) NJOY-SHEM-15% fuel (k) SERPENT-SHEM-15% fuel (l) SERPENT-FEDS-15% fuel

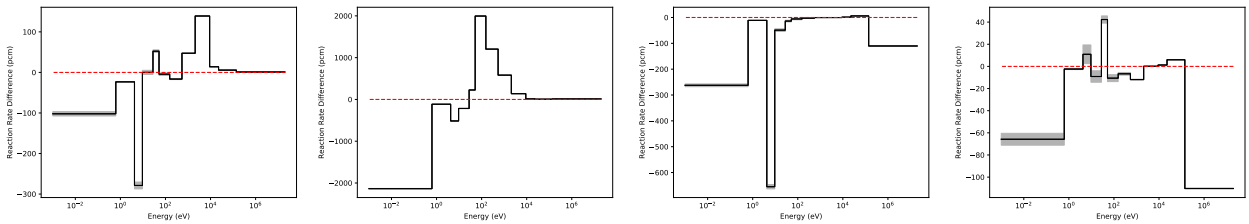

(m) NJOY-FEDS-5% fuel (n) NJOY-SHEM-5% fuel (o) SERPENT-SHEM-5% fuel (p) SERPENT-FEDS-5% fuel

Figure 3.38: Absorption errors in multiple regions of the fuel between MCNP and PDT for different types of cross section data (NJOY-FEDS-166, NJOY-SHEM-166, SERPENT-SHEM-166, SERPENT-FEDS-166) with four regions in fuel for 2D pin cell problem (pcm in 95% condifence). Columns have the same cross sections. Rows have the same QOIs.

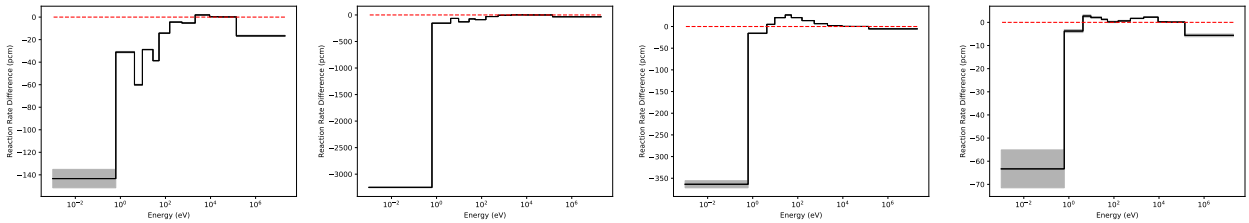

(a) NJOY-FEDS-50% fuel (b) NJOY-SHEM-50% fuel (c) SERPENT-SHEM-50% fuel (d) SERPENT-FEDS-50% fuel

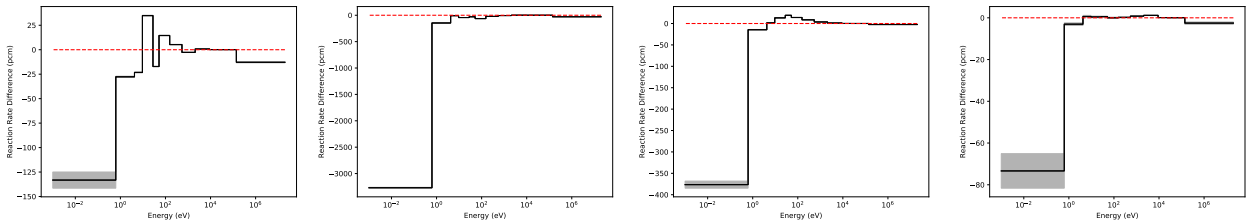

(e) NJOY-FEDS-30% fuel (f) NJOY-SHEM-30% fuel (g) SERPENT-SHEM-30% fuel (h) SERPENT-FEDS-30% fuel

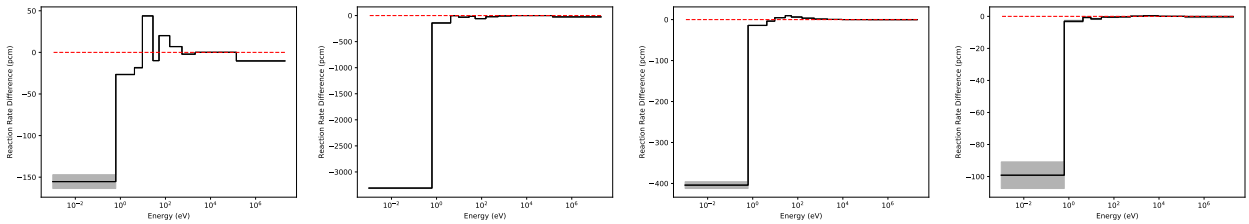

(i) NJOY-FEDS-15% fuel (j) NJOY-SHEM-15% fuel (k) SERPENT-SHEM-15% fuel (l) SERPENT-FEDS-15% fuel

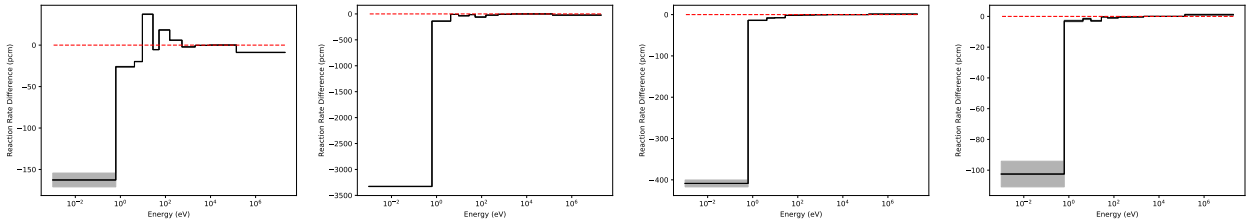

(m) NJOY-FEDS-5% fuel (n) NJOY-SHEM-5% fuel (o) SERPENT-SHEM-5% fuel (p) SERPENT-FEDS-5% fuel

Figure 3.39: Fission errors in multiple regions of the fuel between MCNP and PDT for different types of cross section data (NJOY-FEDS-166, NJOY-SHEM-166, SERPENT-SHEM-166, SERPENT-FEDS-166) with four regions in fuel for 2D pin cell problem (pcm in 95% condifence). Columns have the same cross sections. Rows have the same QOIs.

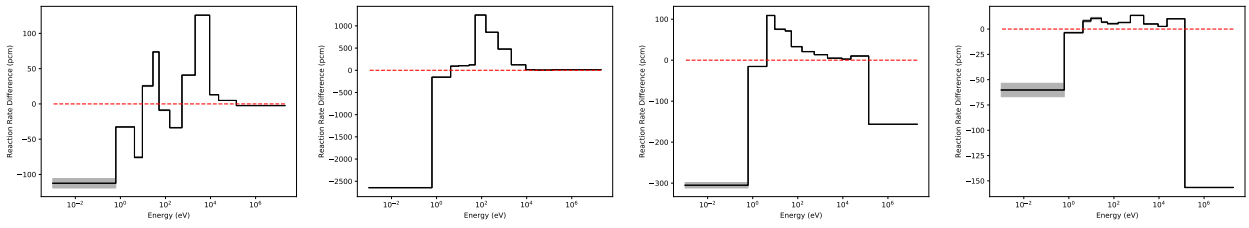

(a) NJOY-FEDS fuel (b) NJOY-SHEM fuel (c) SERPENT-SHEM fuel (d) SERPENT-FEDS fuel

Figure 3.40: Absorption errors in the whole fuel between MCNP and PDT for different types of cross section data (NJOY-FEDS-166, NJOY-SHEM-166, SERPENT-SHEM-166, SERPENT-FEDS-166) with four regions in fuel for 2D pin cell problem (pcm in 95% condifence).

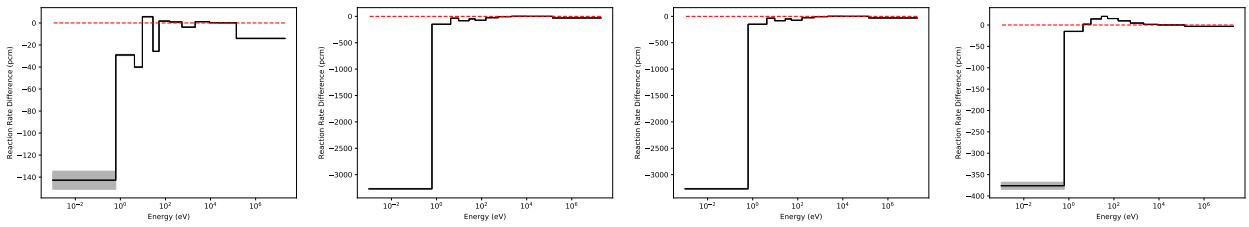

(a) NJOY-FEDS fuel (b) NJOY-SHEM fuel (c) SERPENT-SHEM fuel (d) SERPENT-FEDS fuel

Figure 3.41: Fission errors in the whole fuel between MCNP and PDT for different types of cross section data (NJOY-FEDS-166, NJOY-SHEM-166, SERPENT-SHEM-166, NJOY-SHEM-166) with four regions in fuel for 2D pin cell problem (pcm in 95% condifence).

Table 3.43: Errors in integrated absorption rate for different types of cross section data (NJOY-FEDS, NJOY-SHEM, SERPENT-SHEM, SERPENT-FEDS) with four region in fuel for 2D pin cell problem.

Method	50% fuel	30% fuel	15% fuel	5% fuel	fuel
NJOY-FEDS-166	-302	317	447	-137	17
NJOY-FEDS-244	-102	98	126	10	3
NJOY-FEDS-361	-54	59	72	-26	2
NJOY-SHEM-166	-1921	1612	3571	1219	251
NJOY-SHEM-244	-927	936	1607	503	143
NJOY-SHEM-361	-507	601	889	227	104
SERPENT-SHEM-166	29	-78	-325	-1085	-137
SERPENT-SHEM-244	-85	-99	-235	-584	-148
SERPENT-SHEM-361	-127	-152	-195	-191	-150
SERPENT-FEDS-166	-125	-161	-222	-128	-152
SERPENT-FEDS-244	-119	-157	-209	-113	-140
SERPENT-FEDS-361	-115	-155	-206	-121	-136

Table 3.44: Errors in integrated fission rate for different types of cross section data (NJOY-FEDS, NJOY-SHEM, SERPENT-SHEM, SERPENT-FEDS) with four region in fuel for 2D pin cell problem.

Method	50% fuel	30% fuel	15% fuel	5% fuel	fuel
NJOY-FEDS-166	-349	-160	-127	-136	-245
NJOY-FEDS-244	-36	65	93	97	23
NJOY-FEDS-361	-13	63	82	83	31
NJOY-SHEM-166	-3838	-3615	-3590	-3616	-3719
NJOY-SHEM-244	-1917	-1750	-1731	-1758	-1827
NJOY-SHEM-361	-1222	-1131	-1118	-1130	-1172
SERPENT-SHEM-166	-300	-332	-373	-416	-327
SERPENT-SHEM-244	-197	-211	-231	-246	-209
SERPENT-SHEM-361	-94	-100	-109	-113	-99
SERPENT-FEDS-166	-71	-74	-81	-83	-74
SERPENT-FEDS-244	-67	-68	-78	-80	-68
SERPENT-FEDS-361	-67	-74	-80	-82	-73

Table 3.45: L1 errors in absorption rate for different types of cross section data (NJOY-FEDS, NJOY-SHEM, SERPENT-SHEM, SERPENT-FEDS) with four region in fuel for 2D pin cell problem.

Method	50% fuel	30% fuel	15% fuel	5% fuel	fuel
NJOY-FEDS-166	571	714	704	666	549
NJOY-FEDS-244	268	215	238	239	213
NJOY-FEDS-361	221	215	226	232	206
NJOY-SHEM-166	4312	7291	9002	7139	5851
NJOY-SHEM-244	2498	3929	4504	3671	3277
NJOY-SHEM-361	1823	2625	2867	2477	2219
SERPENT-SHEM-166	1027	882	602	1099	817
SERPENT-SHEM-244	646	596	501	598	546
SERPENT-SHEM-361	401	351	269	310	347
SERPENT-FEDS-166	344	274	246	260	286
SERPENT-FEDS-244	325	265	232	240	267
SERPENT-FEDS-361	324	262	229	245	265

Table 3.46: L1 errors in fission rate for different types of cross section data (NJOY-FEDS, NJOY-SHEM, SERPENT-SHEM, SERPENT-FEDS) with four region in fuel for 2D pin cell problem.

Method	50% fuel	30% fuel	15% fuel	5% fuel	fuel
NJOY-FEDS-166	354	271	270	260	264
NJOY-FEDS-244	176	163	170	172	155
NJOY-FEDS-361	171	152	159	158	151
NJOY-SHEM-166	3843	3617	3591	3616	3722
NJOY-SHEM-244	1920	1797	1799	1801	1829
NJOY-SHEM-361	1226	1132	1118	1131	1174
SERPENT-SHEM-166	490	455	425	418	461
SERPENT-SHEM-244	278	262	253	248	267
SERPENT-SHEM-361	133	122	116	115	125
SERPENT-FEDS-166	92	82	82	85	85
SERPENT-FEDS-244	88	75	80	81	79
SERPENT-FEDS-361	88	81	81	83	84

3.2 2X2 Pin Cell Calculation

The SERPENT-FEDS method is also tested on simple 2x2 MOX and UO_2 pin cell problem. The UO_2 pin cell is of the same material compositions and dimensions in the previous calculation. The MOX fuel is composed of 95% of U-238 and 5% Pu-239 with a density of 10.29769 g/cm^3. The same procedure is applied for comparison of different cross section generation methods. The fuel region is further divided into 2 regions (95%, 5% of volume) for QOIs comparisons. P_3 scattering is used. The mesh is plotted in Fig. 3.42. There is 6, 3, 8 number of cells in radial direction and 16, 32, 32 number of cells in azimuthal direction. Gauss-Chebyshev product quadrature is

used for angular quadrature with 16 polar angles and 32 azimuthal angles.

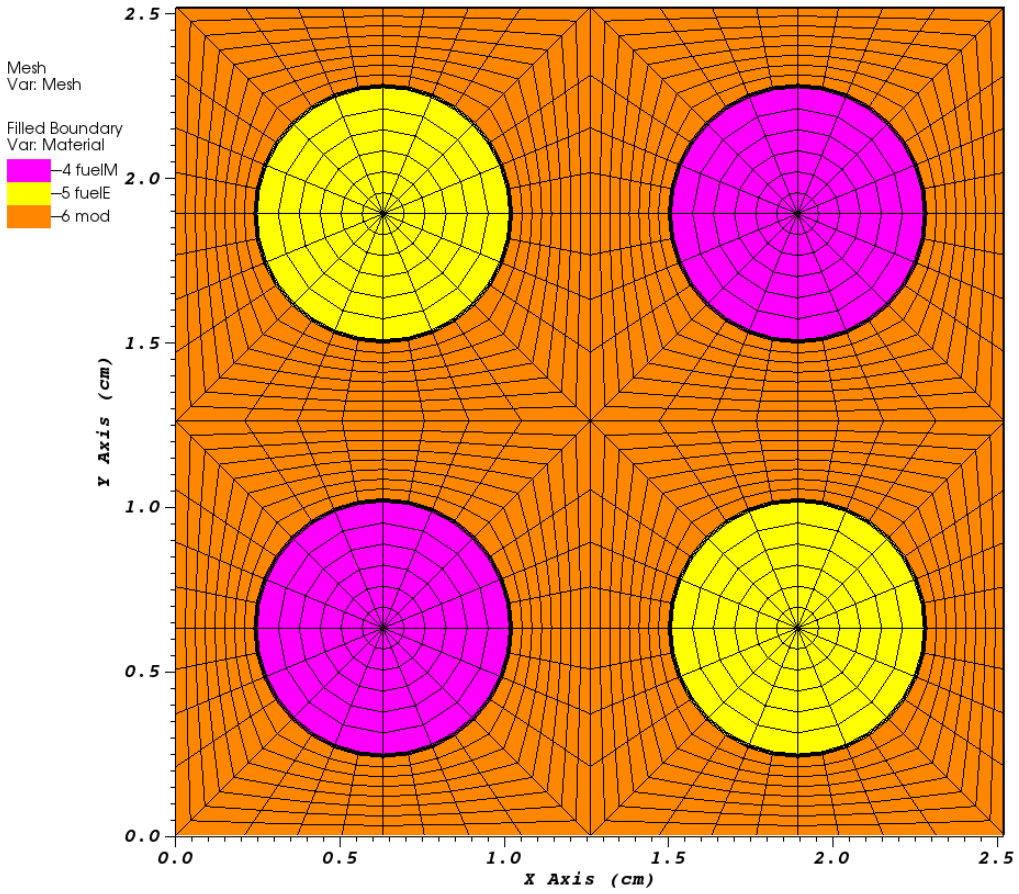

Figure 3.42: PDT mesh for 2x2 pin cell problem

The results for k_{eff} for different type of cross sections for 2X2 pin cell problem is listed in Table 3.47. For each method, the errors in k_{eff} decrease as the number of unknowns increases. And SERPENT-FEDS method gives the best results for k_{eff}.

The absorption errors in the outer 5% fuel in UO_2 and MOX pin cells for different types of cross sections for 166 groups are plotted in Figs. 3.43 and 3.44, respectively. The errors in in absorption and fission rates for UO_2 and MOX fuel region for different types of cross sections

Table 3.47: Errors in k_{eff} for different types of cross sections (NJOY-FEDS, NJOY-SHEM, SERPENT-SHEM, SERPENT-FEDS) for 2X2 pin cell problem.

Method	Unknowns (RRR)	K_{eff}	E_{pcm}	Efficiency $\frac{1}{\lvert Error \rvert \times DOF}$
NJOY-FEDS-166	30	1.51128	414 $\pm$1	-8.0
NJOY-FEDS-244	108	1.50697	128 $\pm$1	-7.2
NJOY-FEDS-361	225	1.50664	106 $\pm$1	-4.2
NJOY-SHEM-166	30	1.50529	16 $\pm$1	-8.0
NJOY-SHEM-244	108	1.50466	-26 $\pm$1	-7.2
NJOY-SHEM-361	225	1.50153	-234 $\pm$1	-4.2
SERPENT-SHEM-166	30	1.49979	-350 $\pm$1	9.5
SERPENT-SHEM-244	108	1.50190	-209 $\pm$1	4.4
SERPENT-SHEM-361	225	1.50304	-134 $\pm$1	3.3
SERPENT-FEDS-166	30	1.50345	-106 $\pm$1	31.4
SERPENT-FEDS-244	108	1.50362	-95 $\pm$1	9.7
SERPENT-FEDS-361	225	1.50357	-98 $\pm$1	4.5

for 166 groups are plotted in Figs.3.45, 3.46, 3.47 and 3.48, respectively. L1 errors in absorption rates and fission rates for different types of cross section data for different unknown numbers are summarized in Tables 3.48. The absorption errors in the outer 5% UO_2 and MOX fuel show similar behavior for each set of cross section data. The SERPENT-FEDS method gives the best results for the absorption errors in the outer 5% fuel for 166 groups in both pin cells and gives the best results in the L1 errors in the absorption rates for the while fuel.

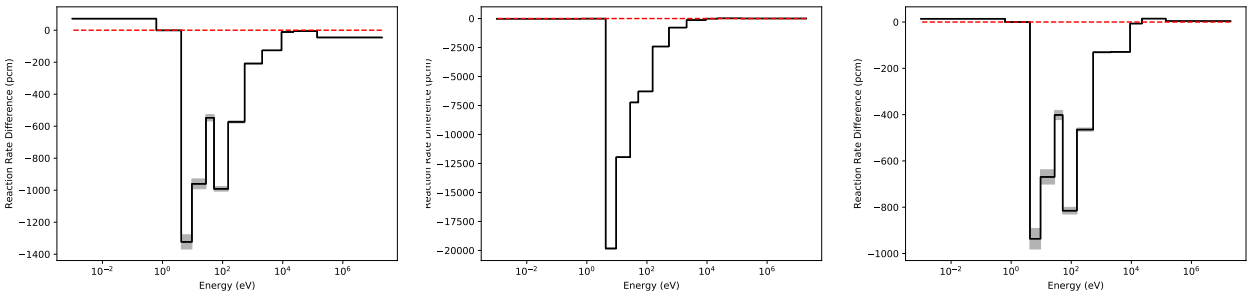

(a) NJOY-FEDS-166 (b) SERPENT-SHEM-166 (c) SERPENT-FEDS-166

Figure 3.43: Absorption errors in outer 5% UO_2 fuel between MCNP and PDT for different types of cross section data (NJOY-FEDS-166, SERPENT-SHEM-166, SERPENT-FEDS-166) for 2X2 pin cell problem (pcm in 95% condifence).

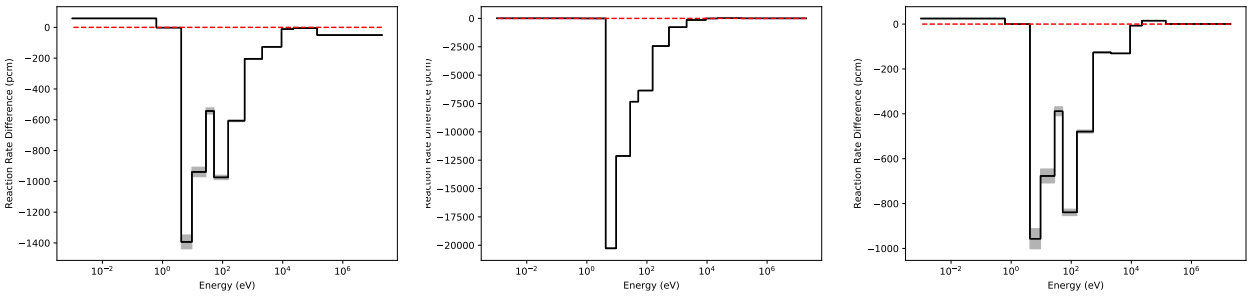

(a) NJOY-FEDS-166 (b) SERPENT-SHEM-166 (c) SERPENT-FEDS-166

Figure 3.44: Absorption errors in outer 5% MOX fuel between MCNP and PDT for different types of cross section data (NJOY-FEDS-166, SERPENT-SHEM-166, SERPENT-FEDS-166) for 2X2 pin cell problem (pcm in 95% condifence).

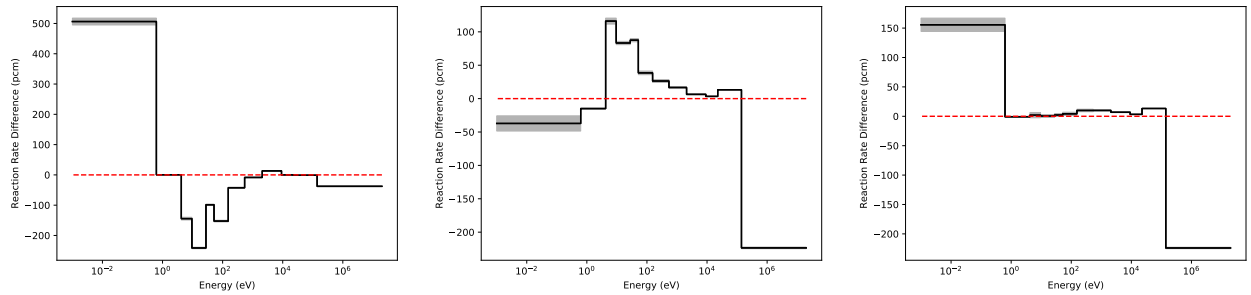

(a) FEDS-166 (b) SERPENT-SHEM-166 (c) SERPENT-FEDS-166

Figure 3.45: Absorption errors in UO_2 fuel between MCNP and PDT for different types of cross section data (NJOY-FEDS-166, SERPENT-SHEM-166, SERPENT-FEDS-166) for 2X2 pin cell problem (pcm in 95% condifence).

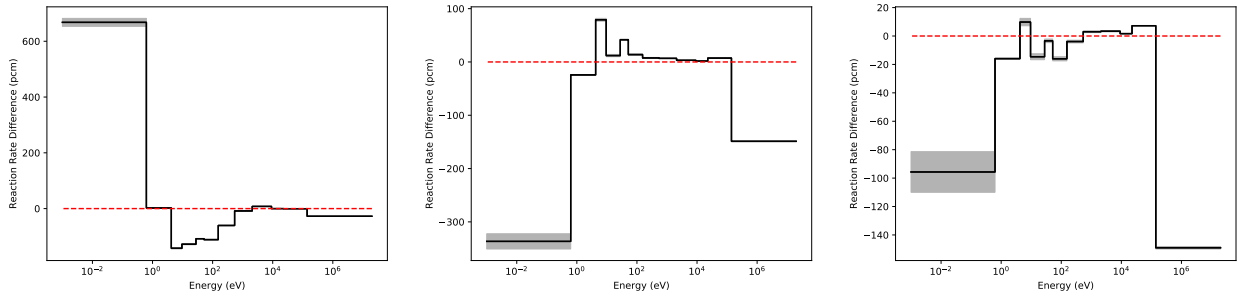

(a) FEDS-166 (b) SERPENT-SHEM-166 (c) SERPENT-FEDS-166

Figure 3.46: Absorption errors in MOX fuel between MCNP and PDT for different types of cross section data (NJOY-FEDS-166, SERPENT-SHEM-166, SERPENT-FEDS-166) for 2X2 pin cell problem (pcm in 95% condifence).

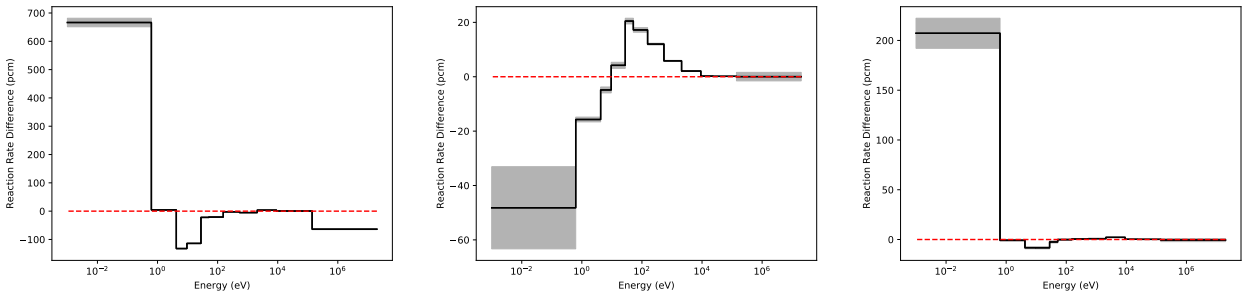

(a) FEDS-166 (b) SERPENT-SHEM-166 (c) SERPENT-FEDS-166

Figure 3.47: Fission errors in UO_2 fuel between MCNP and PDT for different types of cross section data (NJOY-FEDS-166, SERPENT-SHEM-166, SERPENT-FEDS-166) for 2X2 pin cell problem (pcm in 95% condifence).

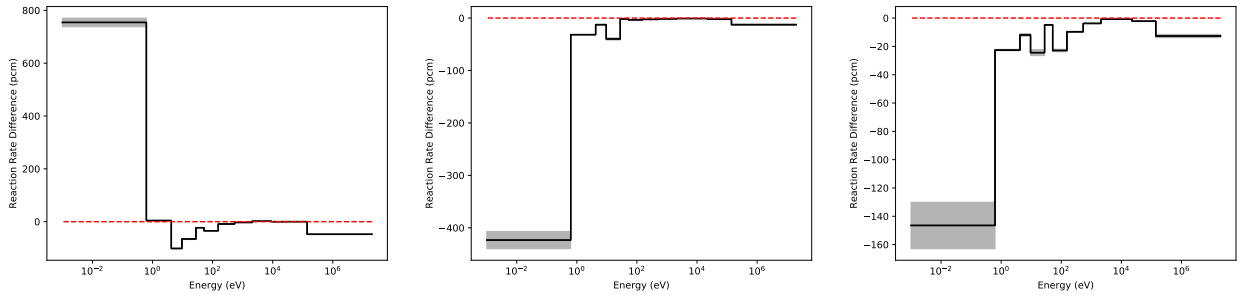

(a) FEDS-166 (b) SERPENT-SHEM-166 (c) SERPENT-FEDS-166

Figure 3.48: Fission errors in MOX fuel between MCNP and PDT for different types of cross section data (NJOY-FEDS-166, SERPENT-SHEM-166, SERPENT-FEDS-166) for 2X2 pin cell problem (pcm in 95% condifence).

Table 3.48: L1 errors in QOIs for different types of cross section data (NJOY-FEDS, NJOY-SHEM, SERPENT-SHEM, SERPENT-FEDS) for 2x2 pin cell problem

Method	UO_2 fuel abs.	UO_2 fuel fiss.	MOX fuel abs.	MOX fuel fiss.
NJOY-FEDS-166	1247	1036	1264	1044
NJOY-FEDS-244	504	436	509	453
NJOY-FEDS-361	443	387	422	380
NJOY-SHEM-166	1988	803	1695	992
NJOY-SHEM-244	1923	774	1500	871
NJOY-SHEM-361	1235	549	958	539
SERPENT-SHEM-166	667	131	683	533
SERPENT-SHEM-244	505	132	460	374
SERPENT-SHEM-361	465	189	363	294
SERPENT-FEDS-166	432	232	324	263
SERPENT-FEDS-244	292	159	217	180
SERPENT-FEDS-361	232	128	184	141

3.3 CASL1B Calculation

We solved a k-eigenvalue problem for CASL1B problem at 600 K as defined in the reference[8]. The fuel radius is 0.4096cm, and there is air around the fuel with thickness of 0.0084 cm. The thickness of clad is 0.057cm, and the size of pitch is 1.26 cm. The compositions of materials are listed in Table P1-4 in reference [8] on Page 23. The PDT mesh is plotted in Fig. 3.49. The fuel region is further divided into 4 regions (50%, 30%, 15%, 5% of volume) for QOIs comparisons. P_3 scattering is used. There is 4, 2, 2, 3, 8 number of cells in radial direction and 12, 12, 16, 32, 32 number of cells in azimuthal direction. Gauss-Chebyshev product quadrature is used for angular

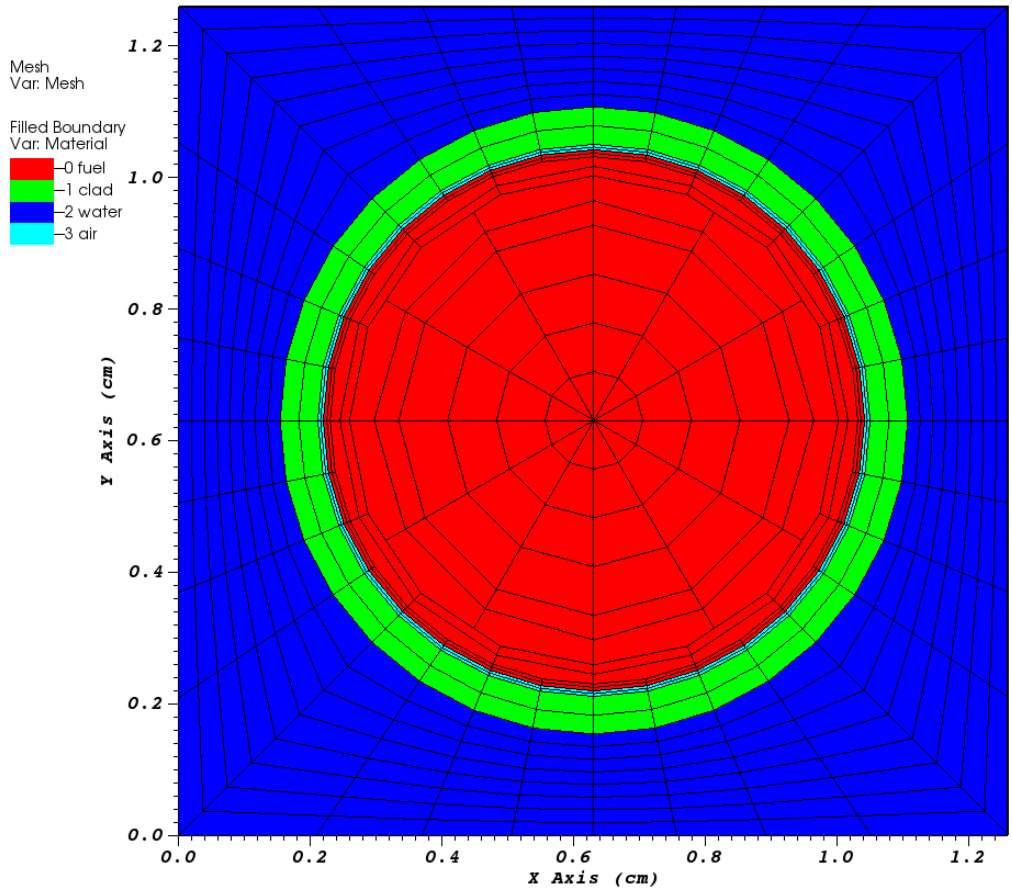

Figure 3.49: PDT mesh for CASL1B problem

quadrature with 24 polar angles and 32 azimuthal angles.

The results of k_{eff} for different types of cross sections for CASL1B problem is listed in Table 3.49. For NJOY-FEDS method, the errors in k_{eff} decrease as the numbers of unknowns increases. SERPENT-FEDS method gives the best results in k_{eff}.

The errors in absorption and fission rates in 50%, 30%, 15%, 5% fuel regions for different types of cross sections for 166 groups are plotted in Figs.3.50-3.51, respectively. The errors in in absorption and fission rates for the whole fuel region for different types of cross sections for 166 groups are plotted in Figs.3.52, and 3.53, respectively. Errors in absorption rates and fission rate

Table 3.49: Errors in k_{eff} for different types of cross sections (NJOY-FEDS, SERPENT-SHEM, SERPENT-FEDS) for CASL1B problem.

Method	Unknowns (RRR)	K_{eff}	E_{pcm}	Efficiency $\frac{1}{\lvert Error \rvert \times DOF}$
NJOY-FEDS-166	30	1.18918	619 $\pm$1	-5.4
NJOY-FEDS-244	108	1.18748	476 $\pm$1	-1.9
NJOY-FEDS-361	225	1.18564	320 $\pm$1	-1.4
SERPENT-SHEM-166	30	1.17920	-225 $\pm$1	14.8
SERPENT-SHEM-244	108	1.17879	-260 $\pm$1	3.6
SERPENT-SHEM-361	225	1.17903	-240 $\pm$1	1.9
SERPENT-FEDS-166	30	1.18113	-62 $\pm$1	54.0
SERPENT-FEDS-244	108	1.18119	-57 $\pm$1	16.3
SERPENT-FEDS-361	225	1.18117	-59 $\pm$1	7.6

for different types of cross section data for different unknown numbers are summarized in Tables 3.50-3.51, respectively . L1 errors in absorption rates and fission rates for different types of cross section data for different unknown numbers are summarized in Tables 3.52-3.53. In the absorption error in the multiple regions of the fuel, SERPENT-SHEM method fails to resolve the errors in RRR, which are of one magnitude larger than that in both FEDS methods. NJOY-FEDS method show larger errors in thermal range in both absorption and fission rates in 50%, 30%, 15%, 5% fuel regions for 166 groups. Overall, SERPENT-FEDS gives the best results for absorption and fission errors in the multiple fuel regions for 166 groups. In addition, SERPENT-FEDS consistently gives the best performance in L1 errors in fission rates in multiple regions of the fuel and in absorption rate in the whole fuel.

3.4 CASL1E Calculation

We solved a k-eigenvalue problem for CASL1E problem at 600 K as defined in the reference[8]. The fuel radius is 0.4096cm and there is integral fuel burnable absorber(IFBA) with thickness of 0.001 cm around fuel. The thickness of air is 0.0074 outside of the absorber, and the clad thickness is 0.057 cm. The length of pitch is 1.26 cm. The compositions of materials are listed in Table

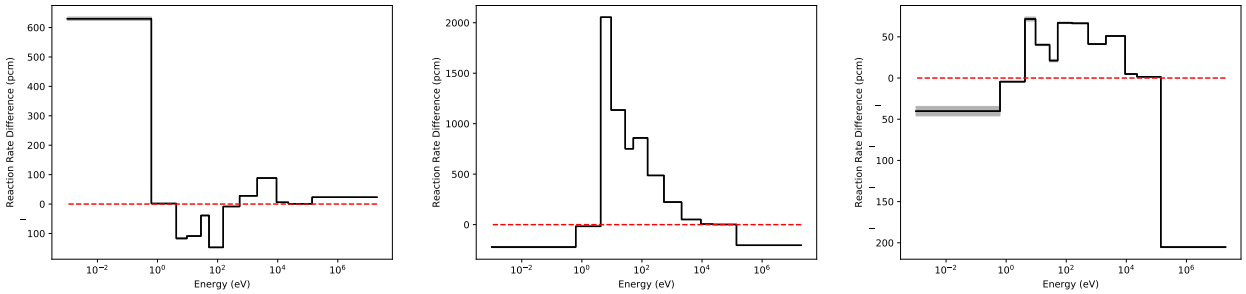

(a) NJOY-FEDS-50% fuel (b) SERPENT-SHEM-50% fuel (c) SERPENT-FEDS-50% fuel

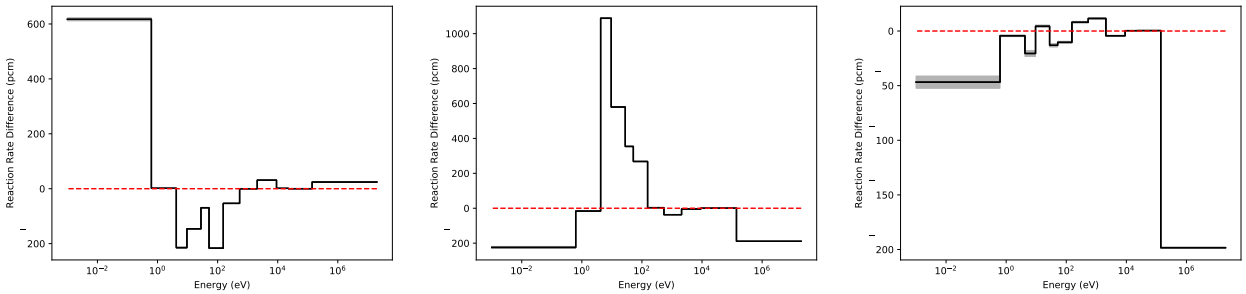

(d) NJOY-FEDS-30% fuel (e) SERPENT-SHEM-30% fuel (f) SERPENT-FEDS-30% fuel

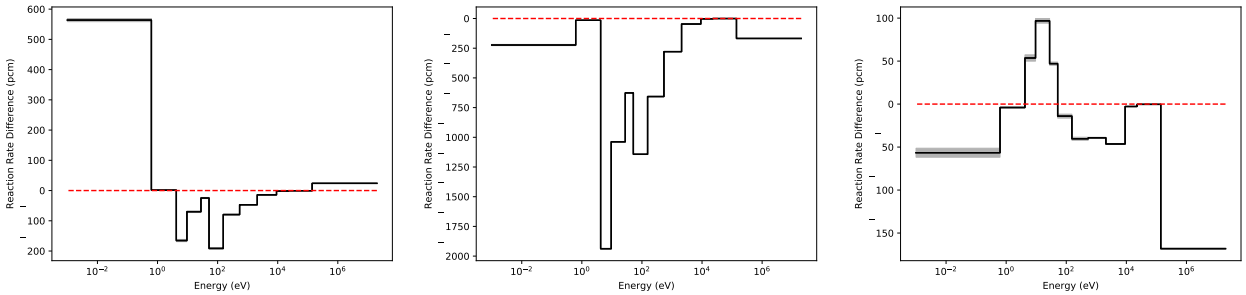

(g) NJOY-FEDS-15% fuel (h) SERPENT-SHEM-15% fuel (i) SERPENT-FEDS-15% fuel

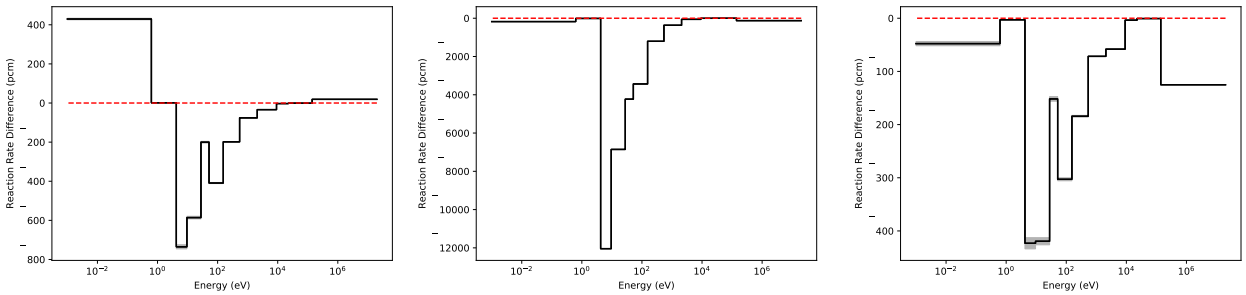

(j) NJOY-FEDS-5% fuel (k) SERPENT-SHEM-5% fuel (l) SERPENT-FEDS-5% fuel

Figure 3.50: Absorption errors in multiple regions of the fuel between MCNP and PDT for different types of cross section data (NJOY-FEDS-166, SERPENT-SHEM-166, SERPENT-FEDS-166) for CASL1B problem (pcm in 95% condifence). Columns have the same cross sections. Rows have the same QOIs.

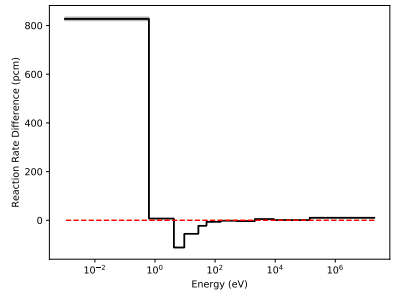

(a) NJOY-FEDS-50% fuel

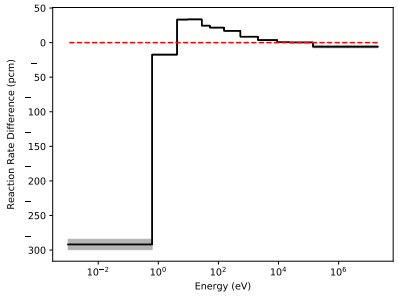

(b) SERPENT-SHEM-50% fuel

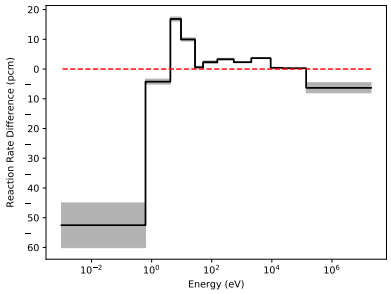

(c) SERPENT-FEDS-50% fuel

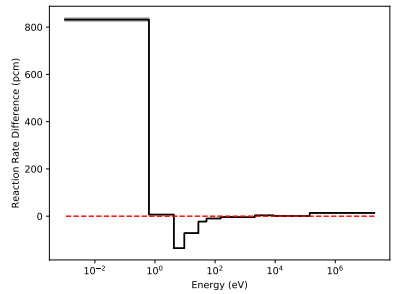

(d) NJOY-FEDS-30% fuel

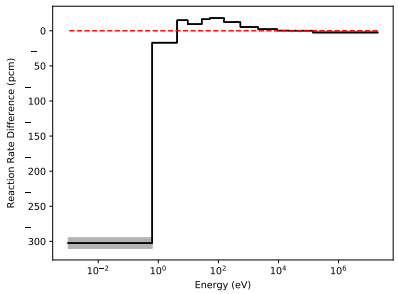

(e) SERPENT-SHEM-30% fuel

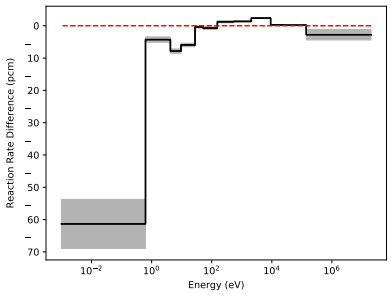

(f) SERPENT-FEDS-30% fuel

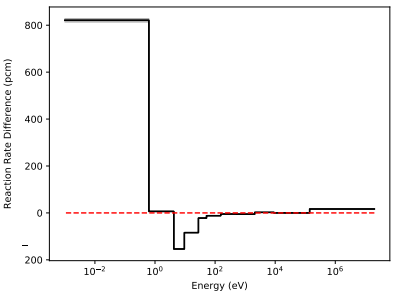

(g) NJOY-FEDS-15% fuel

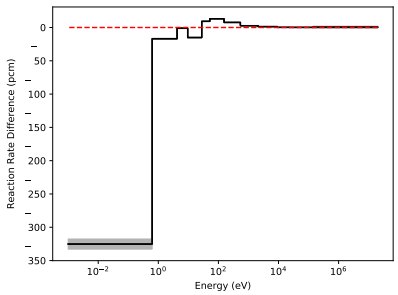

(h) SERPENT-SHEM-15% fuel

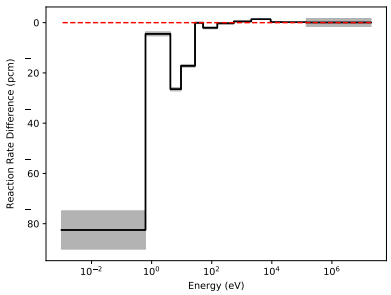

(i) SERPENT-FEDS-15% fuel

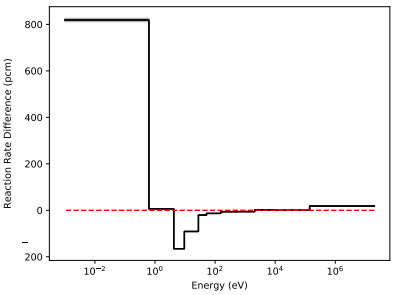

(j) FEDS-5% fuel

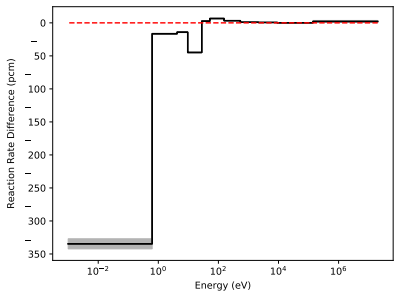

(k) SERPENT-SHEM-5% fuel

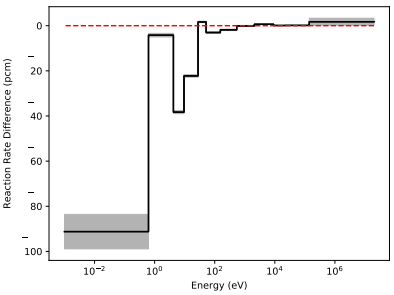

(l) SERPENT-FEDS-5% fuel

Figure 3.51: Fission errors in multiple regions of the fuel between MCNP and PDT for different types of cross section data (NJOY-FEDS-166, SERPENT-SHEM-166, SERPENT-FEDS-166) for CASL1B problem (pcm in 95% condifence). Columns have the same cross sections. Rows have the same QOIs.

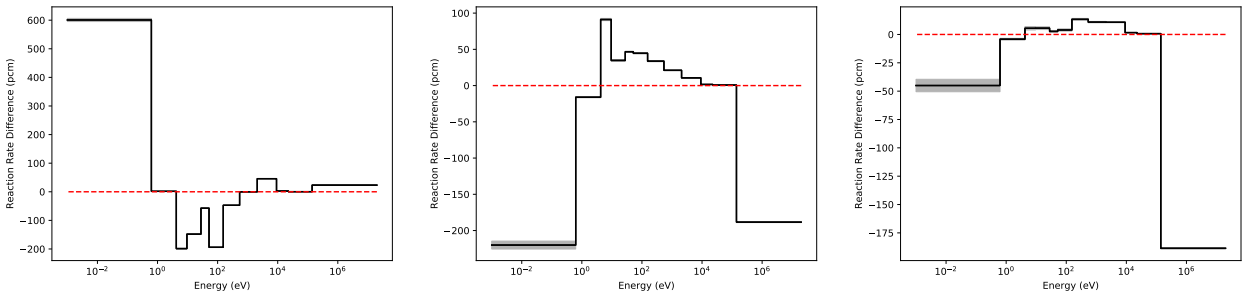

(a) NJOY-FEDS-166 (b) SERPENT-SHEM-166 (c) SERPENT-FEDS-166

Figure 3.52: Absorption errors in the whole fuel between MCNP and PDT for different types of cross section data (NJOY-FEDS-166, SERPENT-SHEM-166, SERPENT-FEDS-166) for CASL1B problem (pcm in 95% condifence).

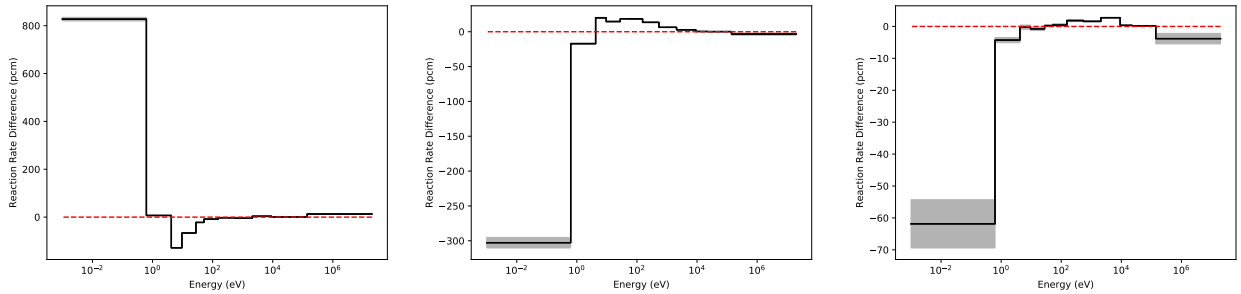

(a) FEDS-166 (b) SERPENT-SHEM-166 (c) SERPENT-FEDS-166

Figure 3.53: Fission errors in the whole fuel between MCNP and PDT for different types of cross section data (NJOY-FEDS-166, SERPENT-SHEM-166, SERPENT-FEDS-166) for CASL1B problem (pcm in 95% condifence).

Table 3.50: Errors in integrated absorption rate for different types of cross sections (NJOY-FEDS, SERPENT-SHEM, SERPENT-FEDS) for CASL1B problem

Method	50% fuel	30% fuel	15% fuel	5% fuel	fuel
NJOY-FEDS-166	358	-25	-5	-1793	29
NJOY-FEDS-244	156	68	6	-162	82
NJOY-FEDS-361	148	92	36	-32	100
SERPENT-SHEM-166	5123	1823	-6136	-28508	-140
SERPENT-SHEM-244	5106	1838	-6102	-28473	-135
SERPENT-SHEM-361	2475	911	-1797	-17619	-147
SERPENT-FEDS-166	114	-262	-173	-1792	-182
SERPENT-FEDS-244	117	-265	-180	-1481	-163
SERPENT-FEDS-361	106	-267	-172	-1407	-182

Table 3.51: Errors in integrated fission rate for different types of cross sections (NJOY-FEDS, SERPENT-SHEM, SERPENT-FEDS) for CASL1B problem

Method	50% fuel	30% fuel	15% fuel	5% fuel	fuel
NJOY-FEDS-166	650	609	565	543	619
NJOY-FEDS-244	440	437	422	418	435
NJOY-FEDS-361	319	320	307	305	317
SERPENT-SHEM-166	-172	-242	-324	-394	-229
SERPENT-SHEM-244	-208	-277	-358	-428	-264
SERPENT-SHEM-361	-198	-254	-321	-379	-243
SERPENT-FEDS-166	-24	-78	-131	-156	-63
SERPENT-FEDS-244	-25	-76	-131	-158	-65
SERPENT-FEDS-361	-21	-78	-130	-153	-63

Table 3.52: L1 errors in integrated absorption rate for different types of cross sections (NJOY-FEDS, SERPENT-SHEM, SERPENT-FEDS) for CASL1B problem

Method	50% fuel	30% fuel	15% fuel	5% fuel	fuel
NJOY-FEDS-166	1198	1376	1183	2692	1320
NJOY-FEDS-244	769	788	733	751	759
NJOY-FEDS-361	557	570	548	512	547
SERPENT-SHEM-166	6013	2766	6136	28508	709
SERPENT-SHEM-244	6040	2823	6102	28473	757
SERPENT-SHEM-361	3314	1803	3698	17619	654
SERPENT-FEDS-166	615	310	569	1792	292
SERPENT-FEDS-244	613	314	561	1481	273
SERPENT-FEDS-361	610	313	568	1407	293

Table 3.53: L1 errors in integrated fission rate for different types of cross sections (NJOY-FEDS, SERPENT-SHEM, SERPENT-FEDS) for CASL1B problem

Method	50% fuel	30% fuel	15% fuel	5% fuel	fuel
NJOY-FEDS-166	1051	1105	1128	1147	1084
NJOY-FEDS-244	592	606	600	599	598
NJOY-FEDS-361	487	495	486	483	489
SERPENT-SHEM-166	458	402	393	426	418
SERPENT-SHEM-244	480	425	425	458	441
SERPENT-SHEM-361	367	343	372	393	337
SERPENT-FEDS-166	102	89	135	165	78
SERPENT-FEDS-244	100	89	134	162	78
SERPENT-FEDS-361	102	88	134	167	76

P1-4 in reference [8] on Page 23. The PDT mesh is plotted in Fig. 3.54. The fuel region is further divided into 4 regions (50%, 30%, 15%, 5% of volume) for QOIs comparisons. P_3 scattering is used. There is 4, 2, 2, 3, 8 number of cells in radial direction and 12, 12, 16, 32, 32 number of cells in azimuthal direction. Gauss-Chebyshev product quadrature is used for angular quadrature with 24 polar angles and 32 azimuthal angles.

The results of k_{eff} for different types of cross sections for CASL1E problem is listed in Table 3.54. For NJOY-FEDS method, the errors in k_{eff} decrease as the numbers of unknowns increases. SERPENT-FEDS method gives the best results in k_{eff}.

The errors in absorption and fission rates in 50%, 30%, 15%, 5% fuel regions for different types of cross sections for 166 groups are plotted in Figs.3.55-3.56, respectively. The errors in in absorption and fission rates for the whole fuel region for different types of cross sections for 166 groups are plotted in Figs.3.57, and 3.58, respectively. Errors in absorption rates and fission rate for different types of cross section data for different unknown numbers are summarized in Tables 3.55-3.56, respectively . L1 errors in absorption rates and fission rates for different types of cross section data for different unknown numbers are summarized in Tables 3.57-3.58. In the absorption error in the multiple regions of the fuel, SERPENT-SHEM method fails to resolve the errors in

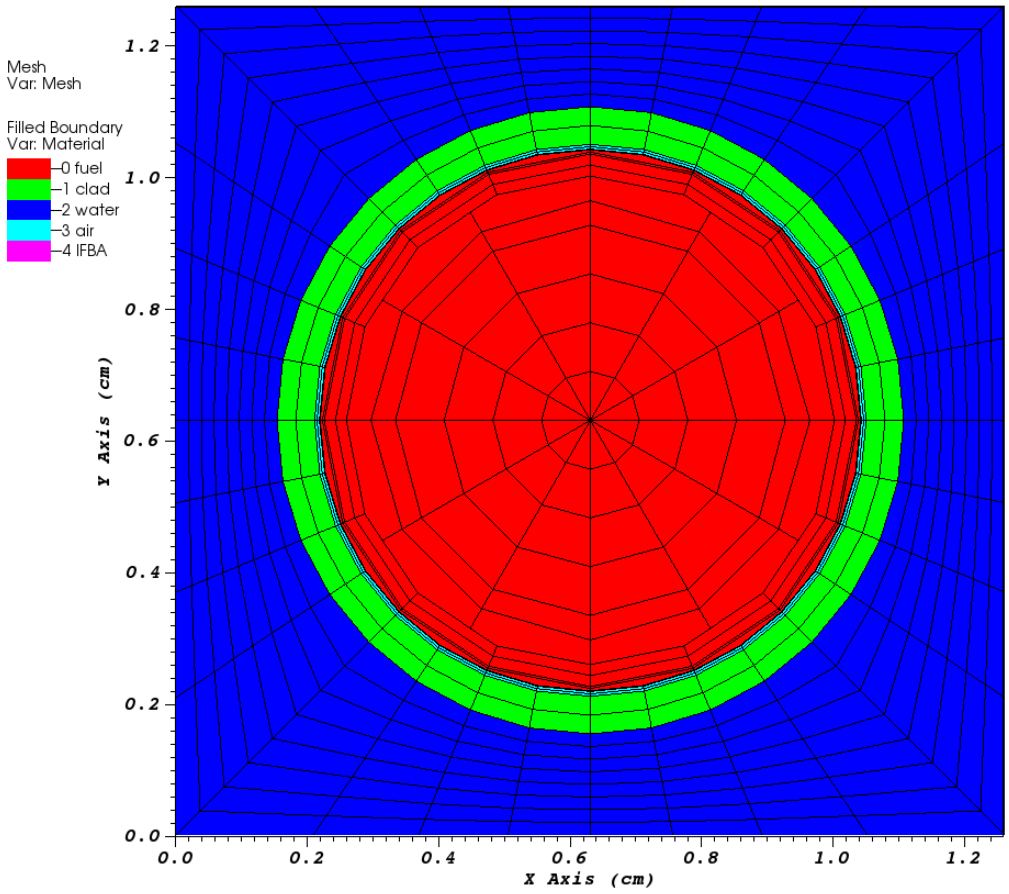

Figure 3.54: PDT mesh for CASL1E problem

Table 3.54: Errors in k_{eff} for different types of cross sections (NJOY-FEDS, NJOY-SHEM, SERPENT-SHEM, SERPENT-FEDS) for CASL1E problem.

Method	Unknowns (RRR)	K_{eff}	E_{pcm}	Efficiency $\frac{1}{\lvert Error \rvert \times DOF}$
NJOY-FEDS-166	30	0.77471	459 ±1	7.3
NJOY-FEDS-244	108	0.77352	305 ±1	3.0
NJOY-FEDS-361	225	0.77276	206 ±1	2.2
NJOY-SHEM-166	30	0.76584	691 ±1	4.8
NJOY-SHEM-244	108	0.76491	812 ±1	1.1
NJOY-SHEM-361	225	0.76891	294 ±1	1.5
SERPENT-SHEM-166	30	0.76956	-208 ±1	16.0
SERPENT-SHEM-244	108	0.76931	-241 ±1	3.8
SERPENT-SHEM-361	225	0.76923	-251 ±1	1.8
SERPENT-FEDS-166	30	0.77029	-115±1	29.1
SERPENT-FEDS-244	108	0.77048	-90±1	10.3
SERPENT-FEDS-361	225	0.77060	-74±1	6.0

RRR, which are of one magnitude larger than that in both FEDS methods. NJOY-FEDS method show larger errors in thermal range in both absorption and fission rates in 50%, 30%, 15%, 5% fuel regions for 166 groups. Overall, SERPENT-FEDS gives the best results for absorption and fission errors in the multiple fuel regions for 166 groups. In addition, SERPENT-FEDS consistently gives the best performance in L1 errors in fission rates in multiple regions of the fuel and in absorption rate in the whole fuel.

Calculations are performed for the four regions in the fuel for cross sections generation. The results for k_{eff} for different type of cross sections for CASL1E problem is listed in Table 3.59. It is noticed that NJOY-SHEM method gives much worse results than the ones in the single ring calculations. In order to exclude the possibility of a code bug, we further test the case for infinite medium problem with NJOY-SHEM cross sections, and the results are listed in Appendix.

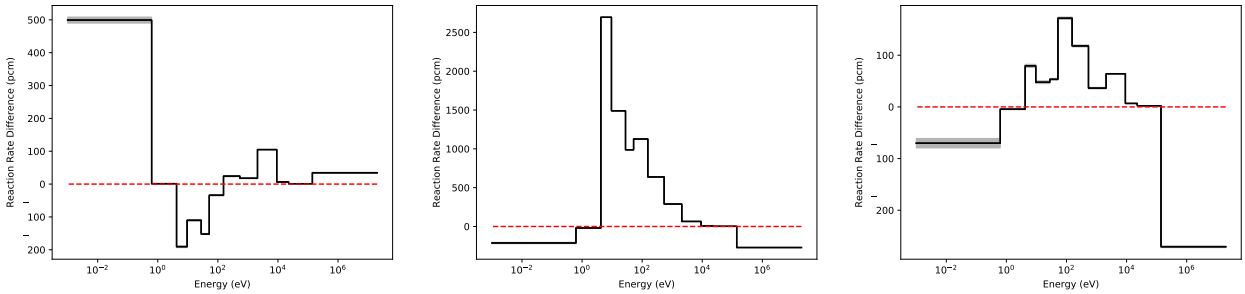

(a) NJOY-FEDS-50% fuel (b) SERPENT-SHEM-50% fuel (c) SERPENT-FEDS-50% fuel

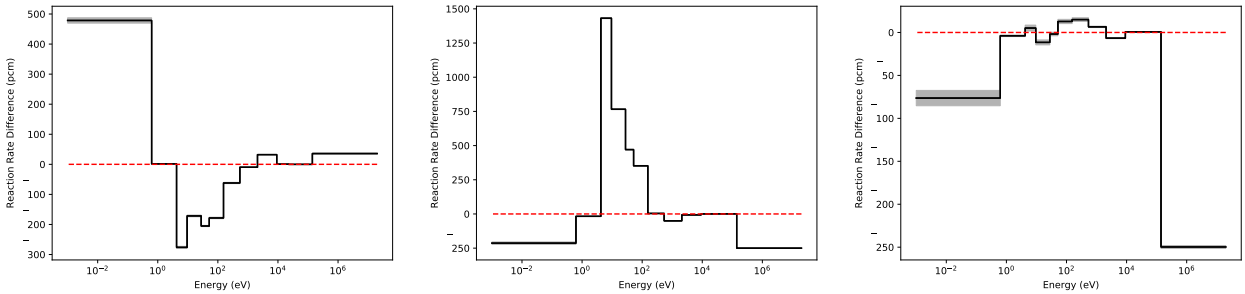

(d) NJOY-FEDS-30% fuel (e) SERPENT-SHEM-30% fuel (f) SERPENT-FEDS-30% fuel

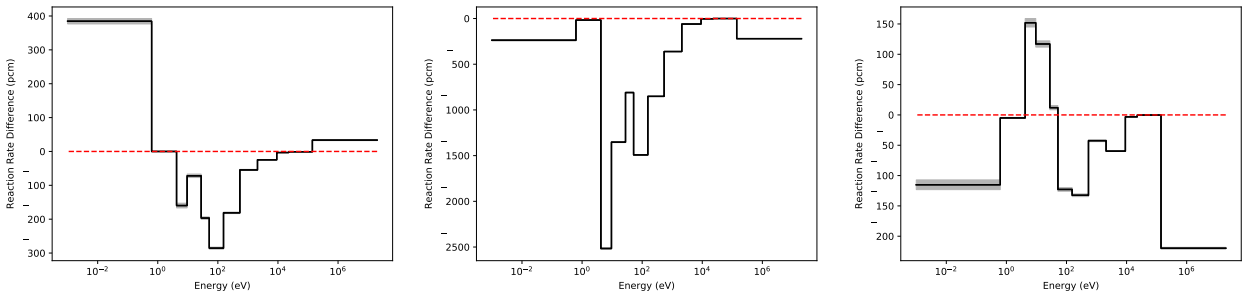

(g) NJOY-FEDS-15% fuel (h) SERPENT-SHEM-15% fuel (i) SERPENT-FEDS-15% fuel

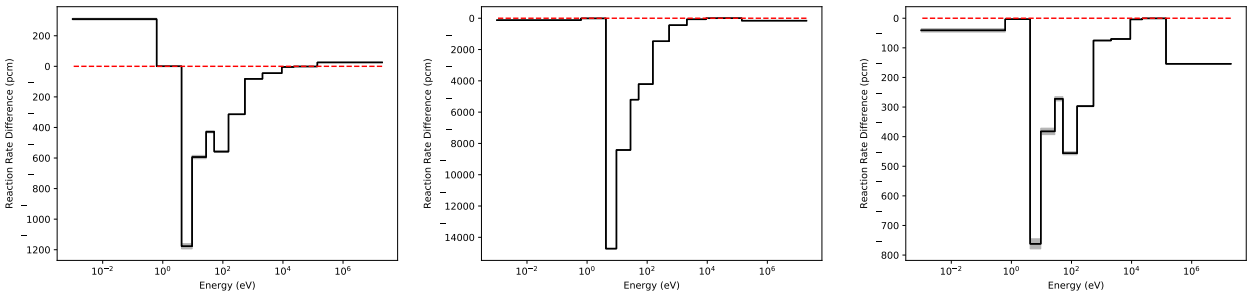

(j) NJOY-FEDS-5% fuel (k) SERPENT-SHEM-5% fuel (l) SERPENT-FEDS-5% fuel

Figure 3.55: Absorption errors in multiple regions of the fuel between MCNP and PDT for different types of cross section data (NJOY-FEDS-166, SERPENT-SHEM-166, SERPENT-FEDS-166) for CASL1E problem (pcm in 95% condifence). Columns have the same cross sections. Rows have the same QOIs.

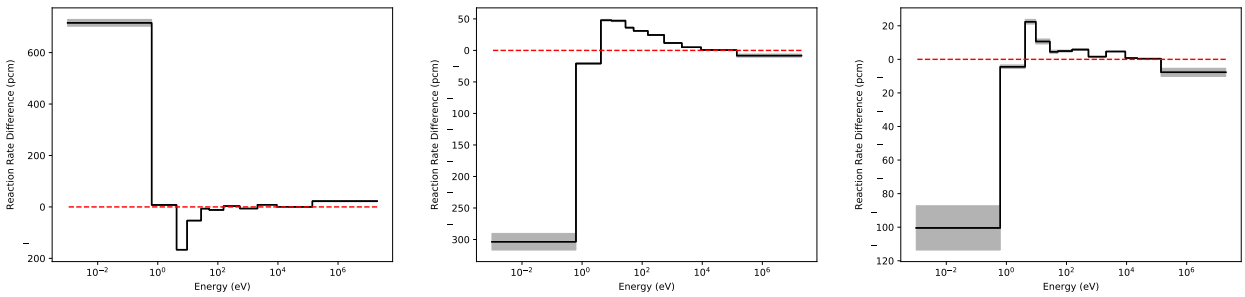

(a) NJOY-FEDS-50% fuel (b) SERPENT-SHEM-50% fuel (c) SERPENT-FEDS-50% fuel

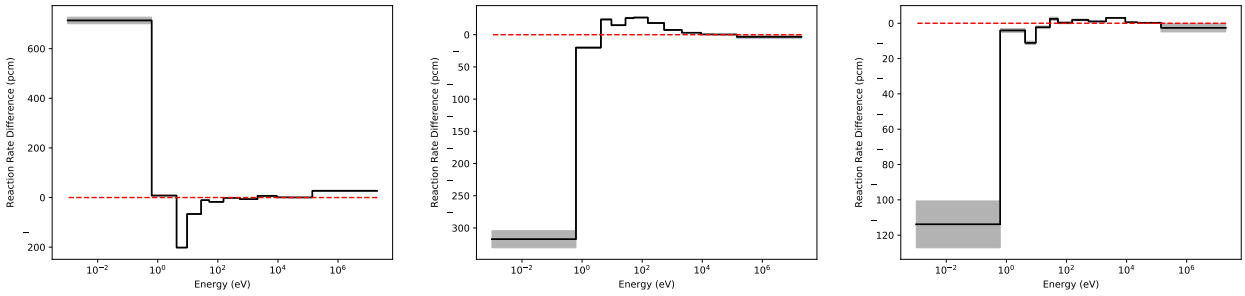

(d) NJOY-FEDS-30% fuel (e) SERPENT-SHEM-30% fuel (f) SERPENT-FEDS-30% fuel

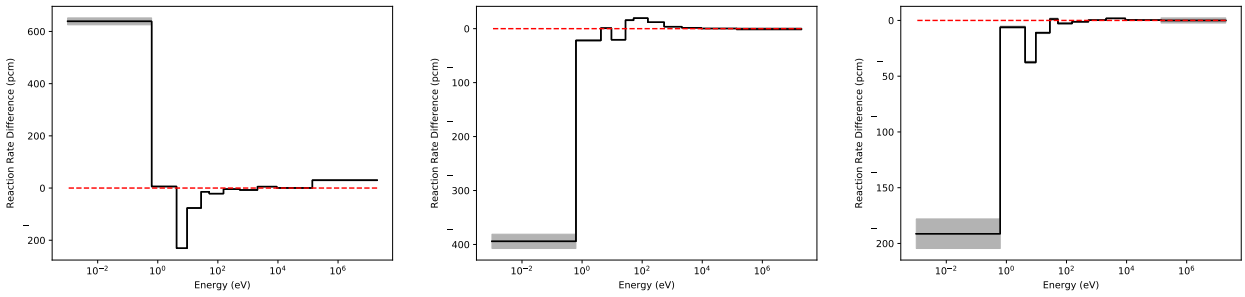

(g) NJOY-FEDS-15% fuel (h) SERPENT-SHEM-15% fuel (i) SERPENT-FEDS-15% fuel

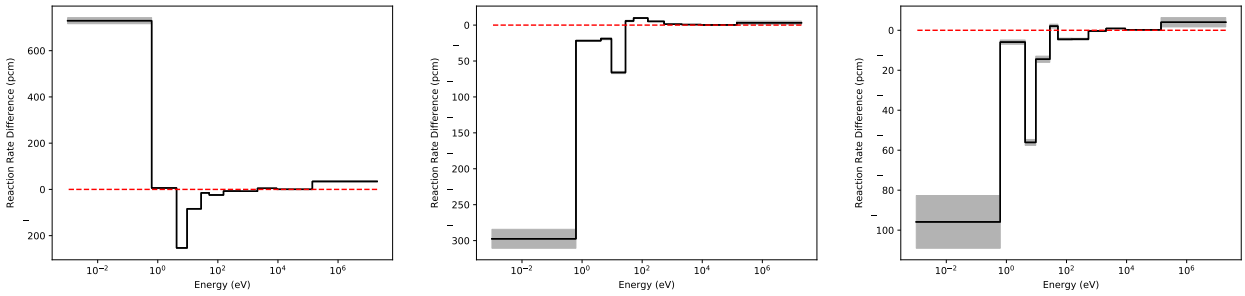

(j) NJOY-FEDS-5% fuel (k) SERPENT-SHEM-5% fuel (l) SERPENT-FEDS-5% fuel

Figure 3.56: Fission errors in multiple regions of the fuel between MCNP and PDT for different types of cross section data (NJOY-FEDS-166, SERPENT-SHEM-166, SERPENT-FEDS-166) for CASL1E problem (pcm in 95% condifence). Columns have the same cross sections. Rows have the same QOIs.

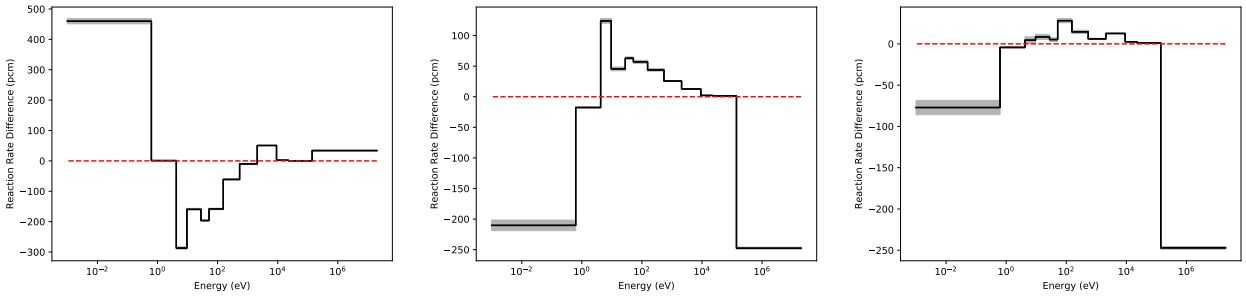

(a) NJOY-FEDS-166 (b) SERPENT-SHEM-166 (c) SERPENT-FEDS-166 fuel

Figure 3.57: Absorption errors in the whole fuel between MCNP and PDT for different types of cross section data (NJOY-FEDS-166, SERPENT-SHEM-166, SERPENT-FEDS-166) for CASL1E problem (pcm in 95% condifence).

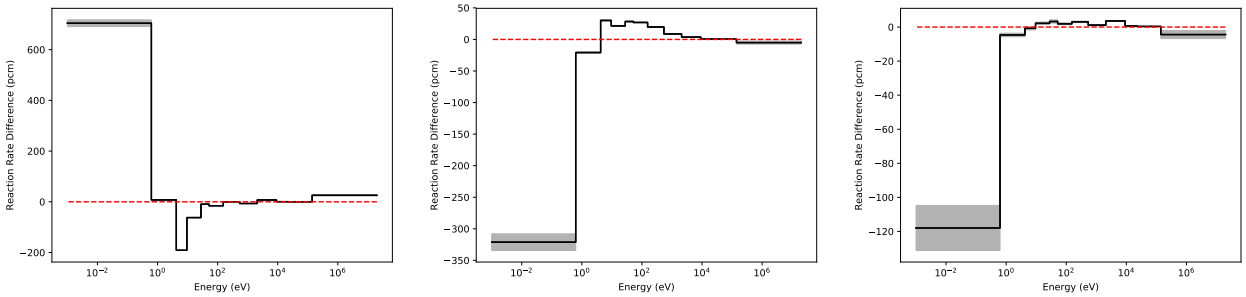

(a) NJOY-FEDS-166 (b) SERPENT-SHEM-166 (c) SERPENT-FEDS-166

Figure 3.58: Fission errors in the whole fuel between MCNP and PDT for different types of cross section data (NJOY-FEDS-166, SERPENT-SHEM-166, SERPENT-FEDS-166) for CASL1E problem (pcm in 95% condifence).

Table 3.55: Errors in integrated absorption rate for different types of cross sections (NJOY-FEDS, NJOY-SHEM, SERPENT-SHEM, SERPENT-FEDS) for CASL1E problem

Method	50% fuel	30% fuel	15% fuel	5% fuel	fuel
NJOY-FEDS-166	203	-354	-561	-2869	-324
NJOY-FEDS-244	-23	-144	92	-892	-107
NJOY-FEDS-361	22	-57	134	-637	-34
NJOY-SHEM-166	7490	3195	-7254	-34358	577
NJOY-SHEM-244	7489	3246	-7173	-34284	611
NJOY-SHEM-361	3623	1557	-1734	-20808	250
SERPENT-SHEM-166	6798	2487	-7922	-34846	-100
SERPENT-SHEM-244	6790	2522	-7862	-34790	-79
SERPENT-SHEM-361	3306	1285	-2153	-21714	-115
SERPENT-FEDS-166	234	-309	-420	-2518	-245
SERPENT-FEDS-244	166	-267	-387	-2152	-222
SERPENT-FEDS-361	189	-266	-377	-2123	-218

Table 3.56: Errors in integrated fission rate for different types of cross sections (NJOY-FEDS, NJOY-SHEM, SERPENT-SHEM, SERPENT-FEDS) for CASL1E problem

Method	50% fuel	30% fuel	15% fuel	5% fuel	fuel
NJOY-FEDS-166	515	452	327	384	461
NJOY-FEDS-244	321	312	232	324	305
NJOY-FEDS-361	218	212	133	225	204
NJOY-SHEM-166	-662	-747	-910	-911	-738
NJOY-SHEM-244	-787	-870	-1030	-1030	-861
NJOY-SHEM-361	-266	-342	-495	-485	-334
SERPENT-SHEM-166	-128	-221	-384	-378	-207
SERPENT-SHEM-244	-163	-254	-416	-410	-241
SERPENT-SHEM-361	-186	-260	-403	-379	-251
SERPENT-FEDS-166	-57	-124	-246	-174	-112
SERPENT-FEDS-244	-54	-113	-217	-153	-105
SERPENT-FEDS-361	-53	-104	-209	-151	-96

Table 3.57: L1 errors in integrated absorption rate for different types of cross sections (NJOY-FEDS, NJOY-SHEM, SERPENT-SHEM, SERPENT-FEDS) for CASL1E problem

Method	50% fuel	30% fuel	15% fuel	5% fuel	fuel
NJOY-FEDS-166	1176	1452	1397	3538	1420
NJOY-FEDS-244	750	781	416	1292	725
NJOY-FEDS-361	570	574	285	958	534
NJOY-SHEM-166	8109	4099	7371	34444	2811
NJOY-SHEM-244	8218	4251	7290	34371	2893
NJOY-SHEM-361	4068	1708	4612	20912	1065
SERPENT-SHEM-166	7803	3563	7922	34846	851
SERPENT-SHEM-244	7830	3631	7862	34790	905
SERPENT-SHEM-361	4278	2327	4879	21714	805
SERPENT-FEDS-166	925	391	982	2518	412
SERPENT-FEDS-244	805	336	863	2152	367
SERPENT-FEDS-361	788	333	847	2123	358

Table 3.58: L1 errors in integrated fission rate for different types of cross sections (NJOY-FEDS, NJOY-SHEM, SERPENT-SHEM, SERPENT-FEDS) for CASL1E problem

Method	50% fuel	30% fuel	15% fuel	5% fuel	fuel
NJOY-FEDS-166	1003	1061	1035	1167	1031
NJOY-FEDS-244	529	537	472	573	524
NJOY-FEDS-361	442	448	382	485	437
NJOY-SHEM-166	846	855	945	915	860
NJOY-SHEM-244	876	895	1036	1034	898
NJOY-SHEM-361	299	358	500	537	344
SERPENT-SHEM-166	537	461	491	430	487
SERPENT-SHEM-244	552	478	518	459	503
SERPENT-SHEM-361	432	395	484	402	396
SERPENT-FEDS-166	168	144	254	189	144
SERPENT-FEDS-244	147	130	224	166	133
SERPENT-FEDS-361	146	120	216	164	122

Table 3.59: Errors in k_{eff} for different types of cross sections (NJOY-FEDS, NJOY-SHEM, SERPENT-SHEM, SERPENT-FEDS) with four regions in fuel for CASL1E problem.

Method	Unknowns (RRR)	K_{eff}	E_{pcm}	Efficiency $\frac{1}{\lvert Error \rvert \times DOF}$
NJOY-FEDS-166	30	0.77198	104 $\pm$1	31.9
NJOY-FEDS-244	108	0.77338	286 $\pm$1	4.7
NJOY-FEDS-361	225	0.77319	262 $\pm$1	2.6
NJOY-SHEM-166	30	0.67559	-12395 $\pm$1	0.3
NJOY-SHEM-244	108	0.68027	-11787 $\pm$1	0.1
NJOY-SHEM-361	225	0.72726	-5694 $\pm$1	0.1
SERPENT-SHEM-166	30	0.77035	-107 $\pm$1	21.7
SERPENT-SHEM-244	108	0.77012	-136 $\pm$1	4.3
SERPENT-SHEM-361	225	0.76993	-160 $\pm$1	1.8
SERPENT-FEDS-166	30	0.77073	-57 $\pm$1	31.8
SERPENT-FEDS-244	108	0.77085	-42 $\pm$1	7.2
SERPENT-FEDS-361	225	0.77083	-44 $\pm$1	3.4

The errors in absorption and fission rates in 50%, 30%, 15%, 5% fuel regions for different types of cross sections for 166 groups are plotted in Figs.3.59 and 3.60, respectively. The errors in in absorption and fission rates for the whole fuel region for different types of cross sections for 166 groups are plotted in Figs.3.61, and 3.61, respectively. Errors in absorption rates and fission rate for different types of cross section data are summarized in Tables 3.60-3.61, respectively . L1 errors in absorption rates and fission rates for different types of cross section data for are summarized in Tables 3.62-3.63, respectively.

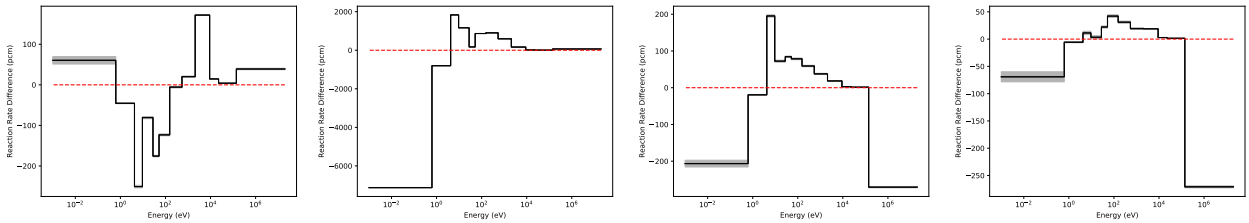

(a) NJOY-FEDS-50% fuel (b) NJOY-SHEM-50% fuel (c) SERPENT-SHEM-50% fuel (d) SERPENT-FEDS-50% fuel

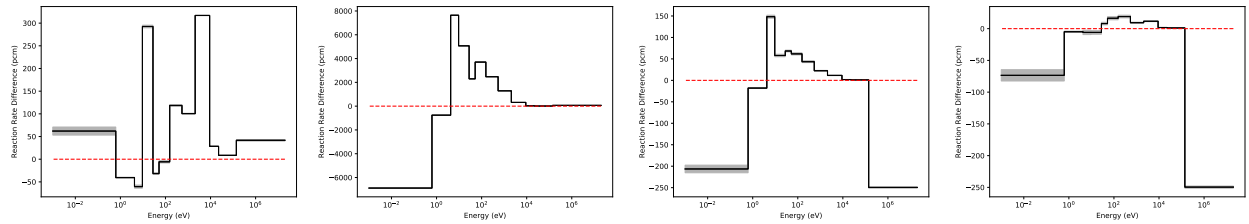

(e) NJOY-FEDS-30% fuel (f) NJOY-SHEM-30% fuel (g) SERPENT-SHEM-30% fuel (h) SERPENT-FEDS-30% fuel

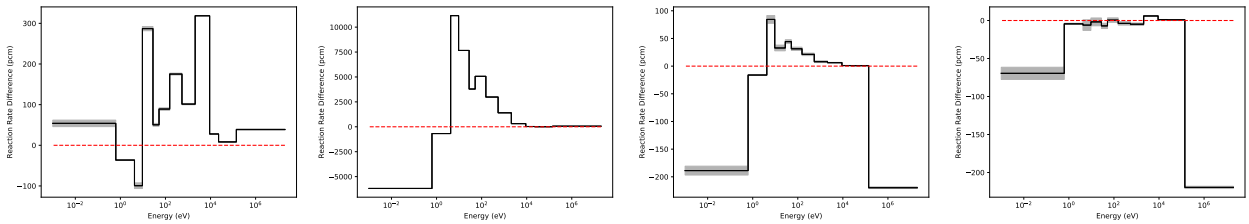

(i) NJOY-FEDS-15% fuel (j) NJOY-SHEM-15% fuel (k) SERPENT-SHEM-15% fuel (l) SERPENT-FEDS-15% fuel

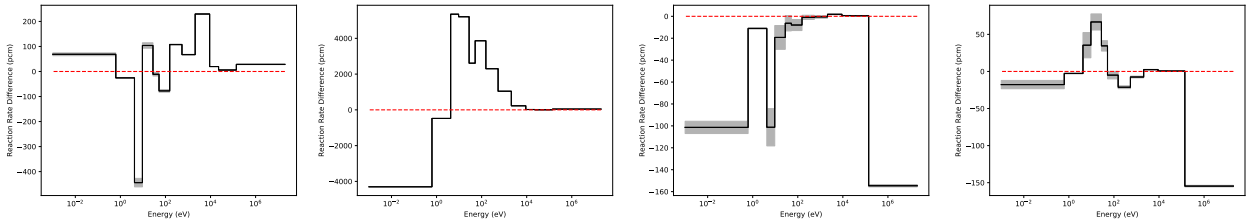

(m) NJOY-FEDS-5% fuel (n) NJOY-SHEM-5% fuel (o) SERPENT-SHEM-5% fuel (p) SERPENT-FEDS-5% fuel

Figure 3.59: Absorption errors in multiple regions of the fuel between MCNP and PDT for different types of cross section data (NJOY-FEDS-166, NJOY-SHEM-166, SERPENT-SHEM-166, SERPENT-FEDS-166) with four regions in fuel for CASL1E problem (pcm in 95% condifence). Columns have the same cross sections. Rows have the same QOIs.

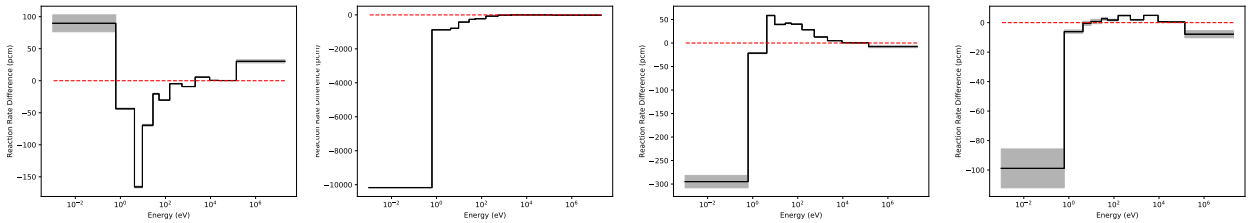

(a) NJOY-FEDS-50% fuel (b) NJOY-SHEM-50% fuel (c) SERPENT-SHEM-50% fuel (d) SERPENT-FEDS-50% fuel

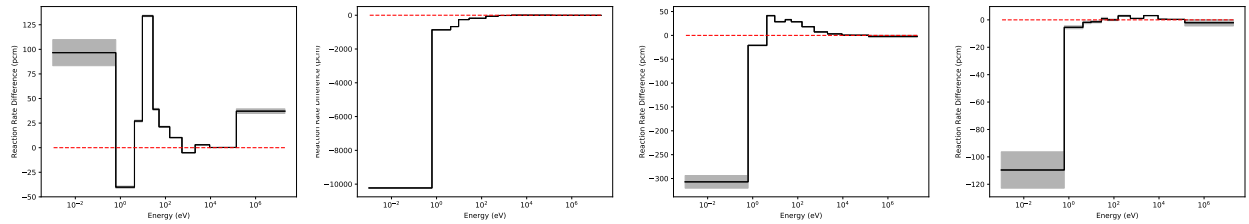

(e) NJOY-FEDS-30% fuel (f) NJOY-SHEM-30% fuel (g) SERPENT-SHEM-30% fuel (h) SERPENT-FEDS-30% fuel

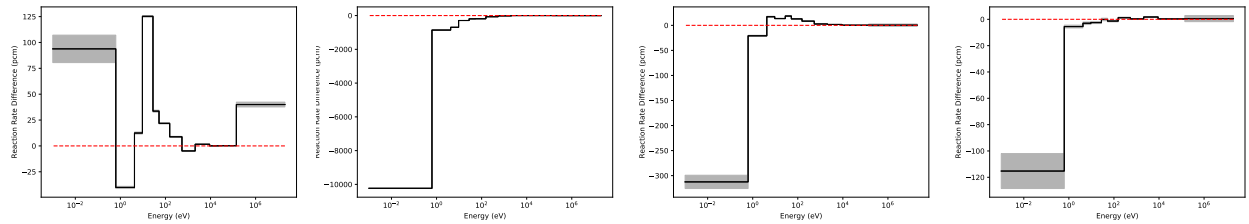

(i) NJOY-FEDS-15% fuel (j) NJOY-SHEM-15% fuel (k) SERPENT-SHEM-15% fuel (l) SERPENT-FEDS-15% fuel

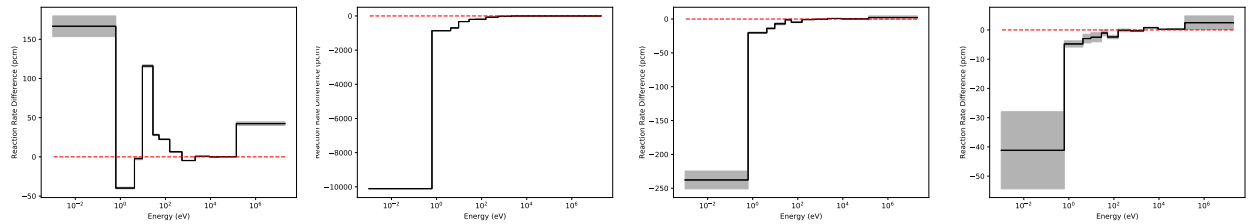

(m) NJOY-FEDS-5% fuel (n) NJOY-SHEM-5% fuel (o) SERPENT-SHEM-5% fuel (p) SERPENT-FEDS-5% fuel

Figure 3.60: Fission errors in multiple regions of the fuel between MCNP and PDT for different types of cross section data (NJOY-FEDS-166, NJOY-SHEM-166, SERPENT-SHEM-166, SERPENT-FEDS-166) with four regions in fuel for CASL1E problem (pcm in 95% condifence). Columns have the same cross sections. Rows have the same QOIs.

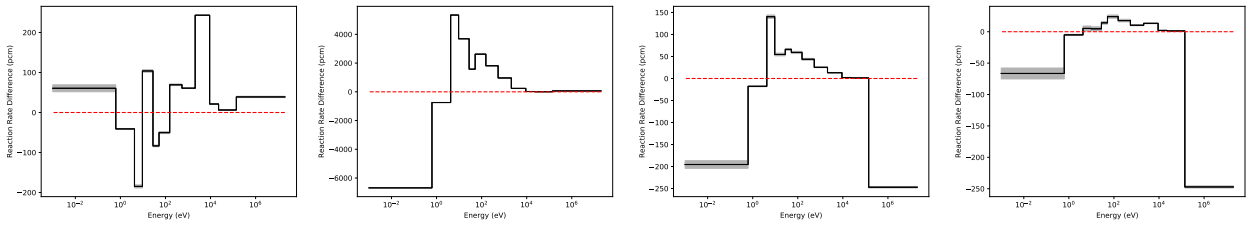

(a) NJOY-FEDS fuel (b) NJOY-SHEM fuel (c) SERPENT-SHEM fuel (d) SERPENT-FEDS fuel

Figure 3.61: Absorption errors in the whole fuel between MCNP and PDT for different types of cross section data (NJOY-FEDS-166, NJOY-SHEM-166, SERPENT-SHEM-166, SERPENT-FEDS-166) with four regions in fuel for CASL1E problem (pcm in 95% condifence).

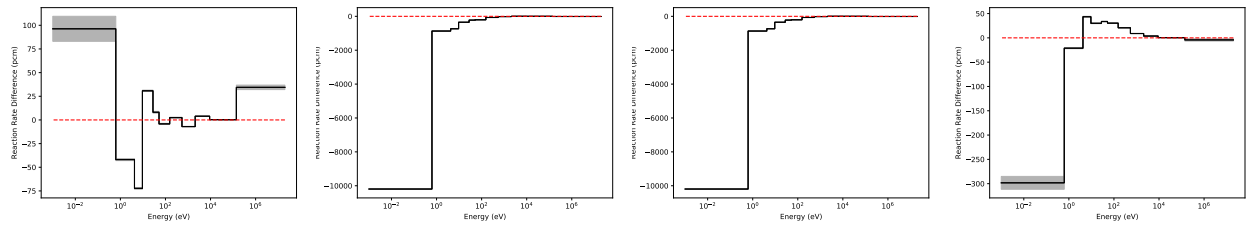

(a) NJOY-FEDS fuel (b) NJOY-SHEM fuel (c) SERPENT-SHEM fuel (d) SERPENT-FEDS fuel

Figure 3.62: Fission errors in the whole fuel between MCNP and PDT for different types of cross section data (NJOY-FEDS-166, NJOY-SHEM-166, SERPENT-SHEM-166, NJOY-SHEM-166) with four regions in fuel for CASL1E problem (pcm in 95% condifence).

Table 3.60: Errors in integrated absorption rate for different types of cross section data (NJOY-FEDS, NJOY-SHEM, SERPENT-SHEM, SERPENT-FEDS) with four region in fuel for CASL1E problem.

Method	50% fuel	30% fuel	15% fuel	5% fuel	fuel
NJOY-FEDS-166	-337	862	1043	92	276
NJOY-FEDS-244	-70	258	275	108	97
NJOY-FEDS-361	30	188	174	69	103
NJOY-SHEM-166	-2122	15268	25624	15911	8943
NJOY-SHEM-244	-1923	14672	24228	13709	8461
NJOY-SHEM-361	-857	7403	12641	4596	4211
SERPENT-SHEM-166	87	-27	-167	-376	-24
SERPENT-SHEM-244	109	-3	-141	-418	-6
SERPENT-SHEM-361	15	74	61	-1172	-52
SERPENT-FEDS-166	-159	-242	-281	-50	-195
SERPENT-FEDS-244	-140	-220	-289	51	-162
SERPENT-FEDS-361	-146	-211	-292	63	-157

Table 3.61: Errors in integrated fission rate for different types of cross section data (NJOY-FEDS, NJOY-SHEM, SERPENT-SHEM, SERPENT-FEDS) with four region in fuel for CASL1E problem.

Method	50% fuel	30% fuel	15% fuel	5% fuel	fuel
NJOY-FEDS-166	-168	369	339	390	99
NJOY-FEDS-244	199	361	359	441	284
NJOY-FEDS-361	202	305	307	393	259
NJOY-SHEM-166	-12801	-12427	-12514	-12445	-12627
NJOY-SHEM-244	-12193	-11805	-11880	-11807	-12009
NJOY-SHEM-361	-6041	-5584	-5643	-5582	-5819
SERPENT-SHEM-166	-48	-124	-212	-229	-104
SERPENT-SHEM-244	-78	-152	-239	-254	-134
SERPENT-SHEM-361	-120	-177	-236	-210	-159
SERPENT-FEDS-166	-46	-66	-77	3	-54
SERPENT-FEDS-244	44	-55	-45	13	-39
SERPENT-FEDS-361	-35	-51	-54	20	-41

Table 3.62: L1 errors in absorption rate for different types of cross section data (NJOY-FEDS, NJOY-SHEM, SERPENT-SHEM, SERPENT-FEDS) with four region in fuel for CASL1E problem.

Method	50% fuel	30% fuel	15% fuel	5% fuel	fuel
NJOY-FEDS-166	1025	1137	1313	1213	994
NJOY-FEDS-244	705	712	613	767	647
NJOY-FEDS-361	550	530	441	668	522
NJOY-SHEM-166	13686	30509	39309	25435	23751
NJOY-SHEM-244	13043	29101	37183	22722	22479
NJOY-SHEM-361	6802	14323	18863	10421	10937
SERPENT-SHEM-166	1013	860	627	382	835
SERPENT-SHEM-244	1065	913	680	425	882
SERPENT-SHEM-361	910	922	820	1179	769
SERPENT-FEDS-166	464	376	298	334	380
SERPENT-FEDS-244	393	333	241	232	315
SERPENT-FEDS-361	394	322	213	220	308

Table 3.63: L1 errors in fission rate for different types of cross section data (NJOY-FEDS, NJOY-SHEM, SERPENT-SHEM, SERPENT-FEDS) with four region in fuel for CASL1E problem.

Method	50% fuel	30% fuel	15% fuel	5% fuel	fuel
NJOY-FEDS-166	518	459	428	481	349
NJOY-FEDS-244	488	444	442	535	427
NJOY-FEDS-361	455	404	399	492	416
NJOY-SHEM-166	12810	12431	12516	12446	12633
NJOY-SHEM-244	12201	11808	11881	11808	12014
NJOY-SHEM-361	6048	5587	5644	5583	5824
SERPENT-SHEM-166	502	445	363	235	448
SERPENT-SHEM-244	515	460	379	258	462
SERPENT-SHEM-361	373	334	291	214	335
SERPENT-FEDS-166	82	83	85	28	77
SERPENT-FEDS-244	63	70	51	16	58
SERPENT-FEDS-361	64	65	60	9	59

3.5 Depletion Calculation for a NSC Pin Cell

A quasi-static depletion calculation at 300 K for a Nuclear Science Center (NSC) pin cell is performed using NJOY-FEDS and SERPENT-FEDS cross sections. The material compositions of fuel are listed in Table 3.64, including the nuclides whose densities will grow as time going on. The material compositions of the coolant are listed in Table 3.65. The fuel radius is 1.8 cm, and the length of pitch is 2 cm. Reflective boundary conditions are used. The mesh is plotted in Fig. 3.63. The fuel region is further divided into 4 regions (50%, 30%, 15%, 5% of volume) for QOIs comparisons. There is 4, 2, 2, 3, 8 number of cells in radial direction and 32, 32, 32, 32, 32

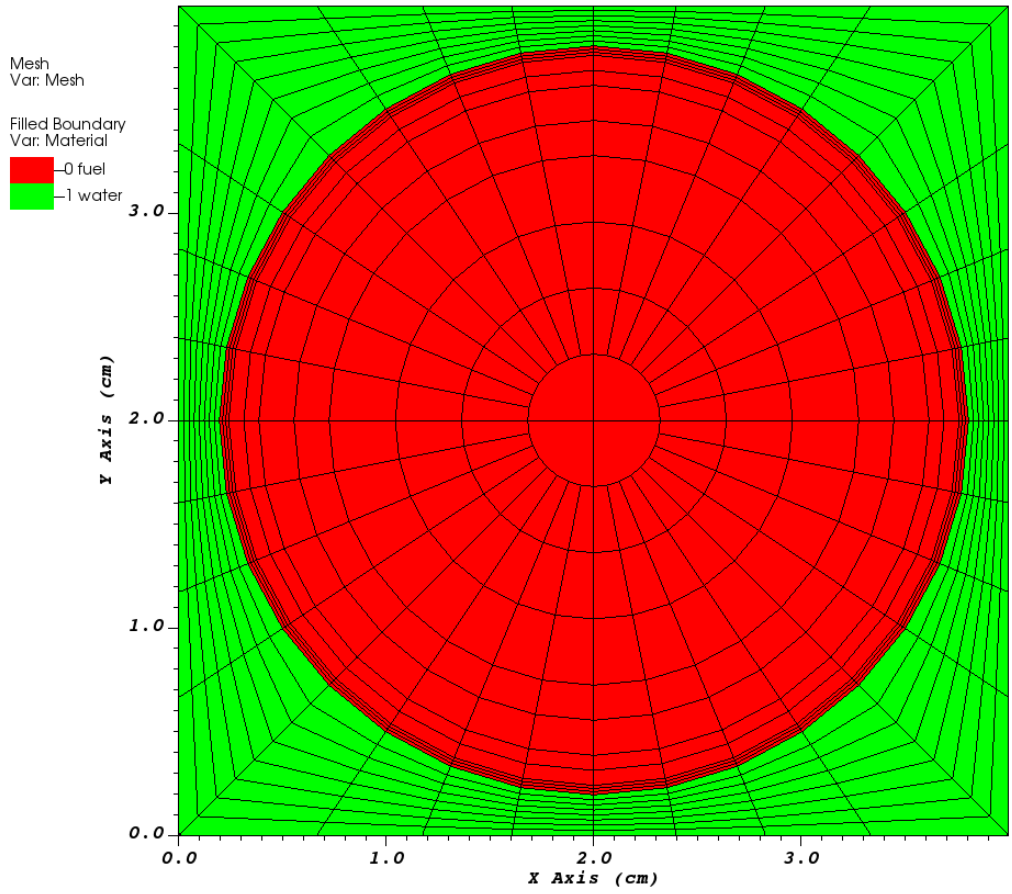

Figure 3.63: PDT mesh for the 2D NSC pin cell depletion calculation.

number of cells in azimuthal direction. Gauss-Chebyshev product quadrature is used for angular quadrature with 24 polar angles and 32 azimuthal angles. The flux is normalized at a pin power of 6500 W. The simulation time is one year. Implicit euler is used for time stepping scheme with 5-day broad time step and 0.25 day Bateman sub-cycles.

The results for k_{eff} over one year is plotted in Fig. 3.64. The atom densities of U-235, Pu239 and Xe-135 over one year are plotted in Figs. 3.65, 3.66, and 3.67. It is observed as time goes on, the errors in k_{eff} and the above three atom densities grow for both SERPENT-FEDS and NJOY-FEDS methods. SERPENT-FEDS method gives slightly better results than NJOY-FEDS method.

Table 3.64: Initial fuel material composition for the 2D NSC pin cell depletion calculation (density units $\frac{\text{atom}}{\text{b-cm}}$).

Nuclide	Density	Nuclide	Density	Nuclide	Density
U-234	7.12E-06	Pu-240	0	Er-166	7.68E-05
U235	1.08E-03	Pu-241	0	Er-167	5.27E-05
U-236	6.24E-06	Pu-242	0	Er168	0
U-237	0	Am-241	0	Zr-90	1.65E-02
U-238	4.30E-03	Am-242	0	Zr-91	3.60E-03
U-239	0	Am-243	0	Zr-92	5.51E-03
Np-237	0	Cm-242	0	Zr-94	5.58E-03
Np-238	0	Cm-243	0	Zr-96	8.99E-04
Np-239	0	Xe-135	0	C-12	1.78E-03
Pu-238	0	Sm-149	0	H-1	4.89E-02
Pu-239	0	Sm-150	0	Nb-95	0
Mo-99	0	Tc-99	0	Rh-103	0
I-131	0	Xe-133	0	Ce-141	0
Pm-147	0	Pm-149	0	Sm-151	0
Eu-155	0	Sm-150	0		

Table 3.65: Coolant composition for the 2D NSC pin cell depletion calculation (density units $\frac{\text{atom}}{\text{b-cm}}$)

Nuclide	Density
H-1	6.67E-02
O-16	3.33E-02

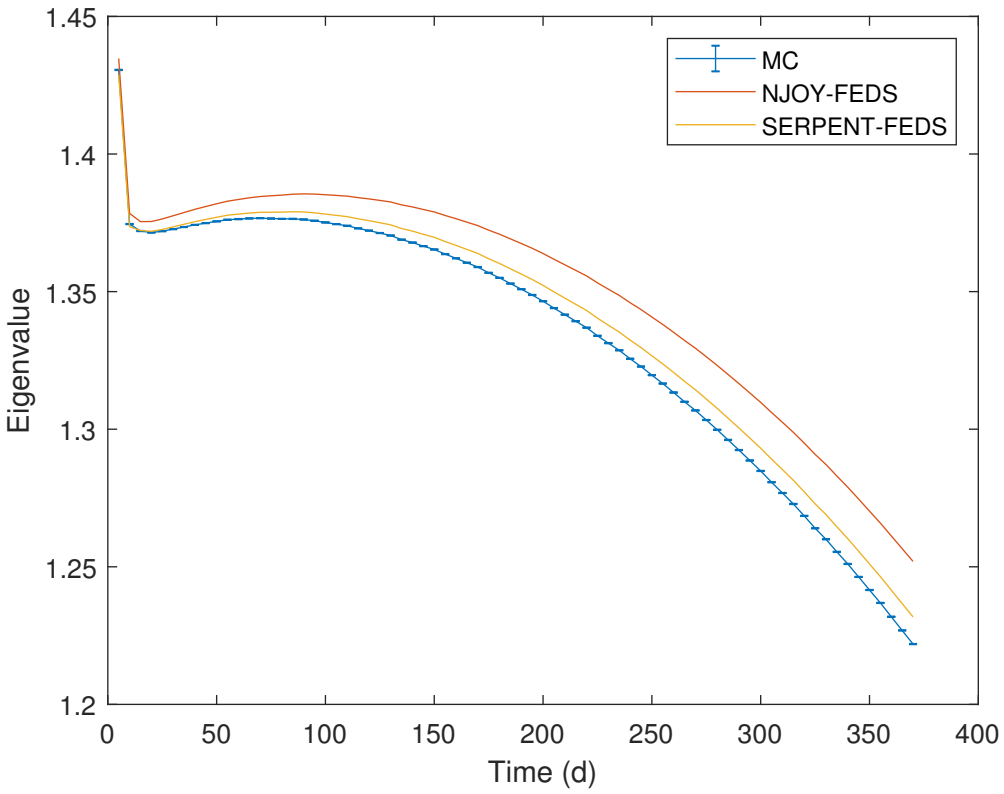

Figure 3.64: Eigenvalue over one year for the 2D NSC pin cell depletion calculation.

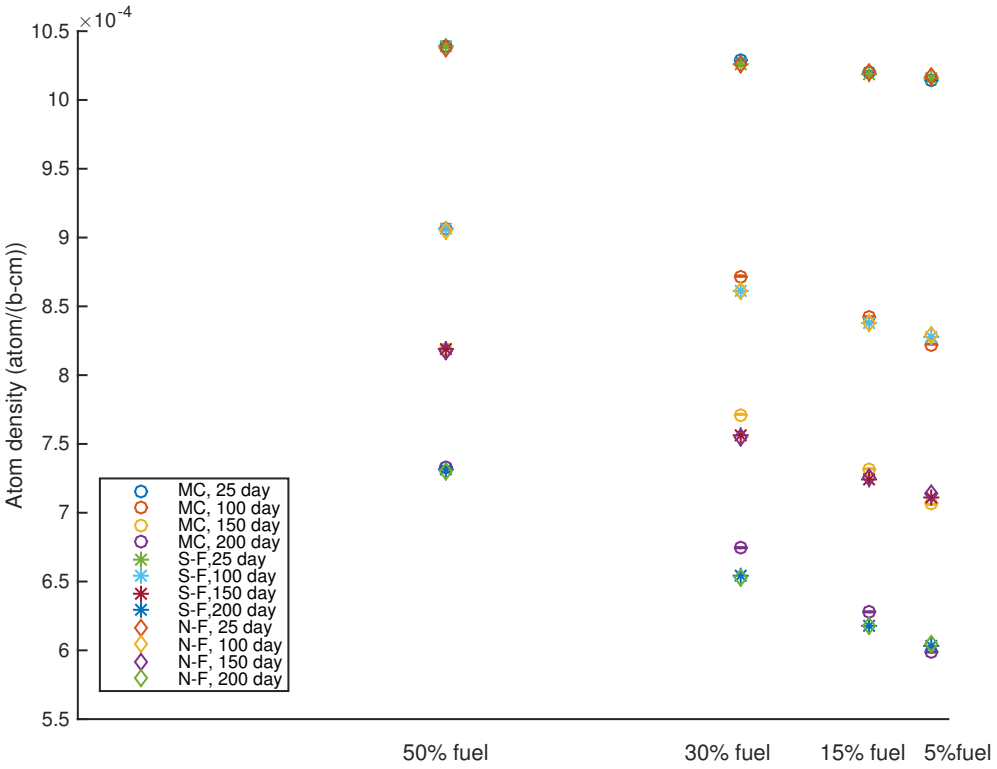

Figure 3.65: U-235 atom density ($\frac{\text{atom}}{\text{b-cm}}$) in 50%, 30% 15% and 5% fuel region over one year for the 2D NSC pin cell depletion calculation.

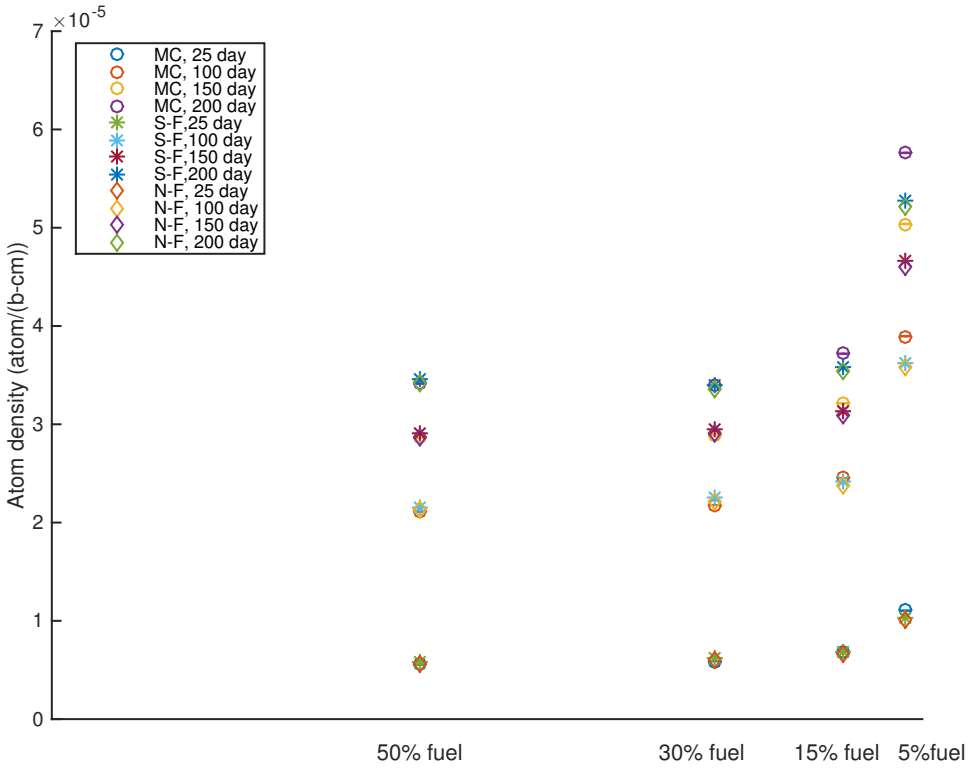

Figure 3.66: Pu-239 atom density ($\frac{\text{atom}}{\text{b-cm}}$)in 50%, 30% 15% and 5% fuel region over one year for the 2D NSC pin cell depletion calculation.

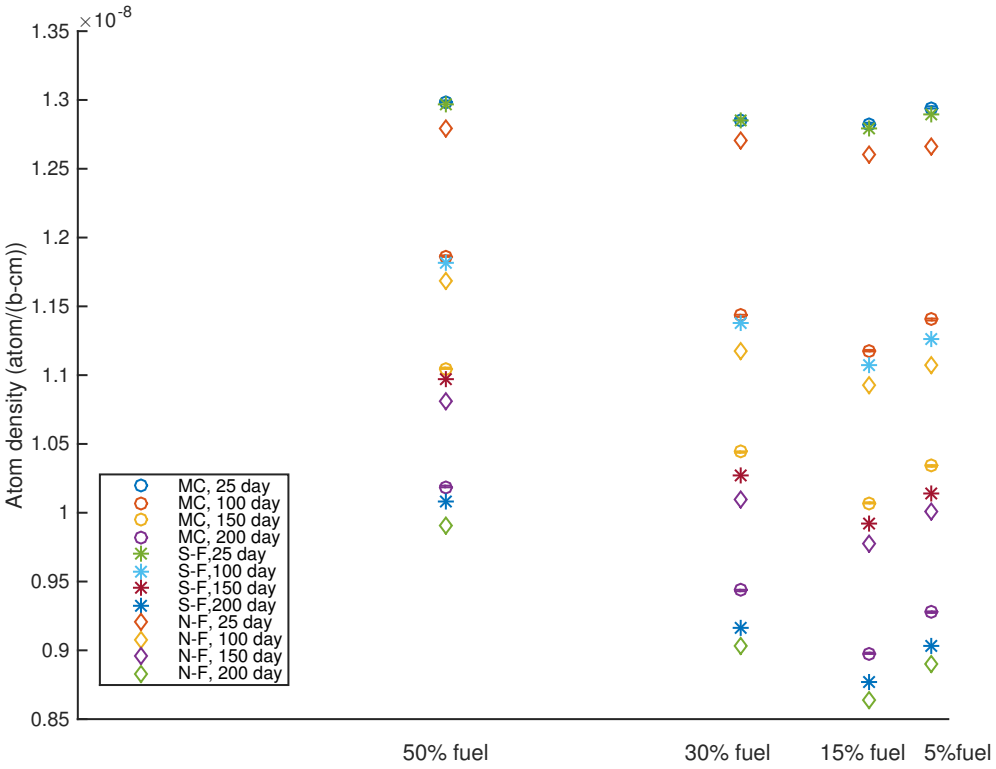

Figure 3.67: Xe-135 atom density ($\frac{\text{atom}}{\text{b-cm}}$) in 50%, 30% 15% and 5% fuel region over one year for the 2D NSC pin cell depletion calculation.

4. SUMMARY AND CONCLUSIONS

4.1 Conclusions

We have further improved and tested the Finite-Element-with-Discontiguous-Support Multi-group (FEDS-MG) method by introducing energy-dependent escape cross sections, tested the FEDS method with analytical spatial-dependent escape cross sections, and also implemented FEDS discontiguous energy group structure in SERPENT for SERPENT-FEDS cross section generation.

Calculations are performed using NJOY-FEDS, NJOY-SHEM, SERPENT-SHEM, and SERPENT-FEDS cross sections for multiple problems. The results for k_{eff}, spatial absorption rate and fission rate are compared to that obtained from continuous-energy Monte Carlo (MC). It is observed that the errors associated with the above QoIs decrease with the number of energy unknowns for each set of cross sections. Introducing the energy-dependent escape cross section improves the NJOY-FEDS performance when the number of energy unknowns is small. Overall, SERPENT-FEDS cross sections consistently give the best results for k_{eff} for all the test problems. Regarding the spatial absorption rate, the errors associated with SERPENT-SHEM and NJOY-SHEM cross sections show similar behavior, and can be an order of magnitude larger than the errors associated with NJOY-FEDS cross sections. This indicates the discontiguous energy mesh in FEDS is more accurate than the standard MG structure for resolving the spatial and energy self-shielding. The implementation of FEDS energy mesh in SERPENT greatly reduces the error in spatial absorption and fission rate compared to SERPENT-SHEM results.

After introducing the spatial resolution for cross sections in the fuel, there is dramatic improvement in FEDS-NJOY results for all calculated QoIs, while the error in k_{eff} increases in SERPENT-SHEM results. Comparing the spatial chord length models, the MCD model for escape cross sections in hollow cylinders consistently exhibits better accuracy than the OCD model, especially for spatial reaction rates. The equal volume division exhibits better accuracy in NJOY-FEDS than equal radius division for spatial reaction rate. Further increasing spatial resolution in NJOY-FEDS

does not guarantee improvement in the accuracy of results based on the test problems.

4.2 Further Work

There are several advantages using the nested energy mesh with discontiguous group within coarse groups as explained in the previous chapter. However, determining the optimal number and the boundaries of the coarse groups still remains to be a question. Resolution of the solution in some coarse groups may be more important than in others for an accurate quantities of interest, such as absorption rate in the outer 5% of the fuel region. Weighting the standard deviations of the snapshots with importance information on certain coarse groups may yield better accuracy in the results.

The generation of snapshots can be improved. Several assumptions are made for the current snapshots calculations: the source from the moderator is of the same shape as the weighting spectrum in NJOY and the heterogeneity effects is accounted for the escape cross section. An alternative way to generate the snapshots would be use the existing ultra-fine code, such as CENTRM continuous energy discrete ordinates code [9], and the Japanese lattice physics code AEGIS [10].

Further improvement is still needed for resolving the spatial energy self-shielding, especially in the fuel region near the moderator. More spatial resolution for fuel cross section generation should be added toward the fuel outer layer. Also, more studies should be performed to incorporate the resonances of important nuclides not present in the chosen bounding material, such as the snapshots of the zirconium cladding near the fuel.

Further tests to compare FEDS-NJOY and SERPENT-FEDS methods in time dependent and radiative transfer problems would be of interests.

REFERENCES

[1] A. T. Till, "Finite elements with discontiguous support for energy discretization in particle transport," Ph.D. thesis, Texas A&M University, College Station, TX, 2015.

[2] A. Till, M. L. Adams, and J. E. Morel, "The finite element with discontiguous support multigroup method: Theory," Joint International Conference on Mathematics and Computation (M&C), Supercomputing in Nuclear Applications (SNA), and the Monte Carlo (MC) Method. American Nuclear Society, Nashville, Tennessee, 2015.

[3] A. T. Till, M. Hanus, J. Lou, J. E. Morel, and M. L. Adams, "Comparisons of the finite-element-with-discontiguous-support method to continuous-energy monte carlo for pin-cell problems (summary)," PHYSOR 2016, Sun Valley, ID, May 1-5,, 2016.

[4] A. Hebert, "The ribon extended self-shielding model," Nucl. Sci. Eng., vol. 151, pp. 1–24, 2005.

[5] J. Leppänen and et al., "The serpent monte carlo code: Status, development and applications in 2013," Ann. Nucl. Energy, vol. 82, pp. 142–150, 2015.

[6] A. Hebert and A. Santamarina, "Refinement of the santamarina-hfaiedh energy mesh between 22.5 ev and 11.4 kev," International Conference on the Physics of Reactors (PHYSOR). American Nuclear Society, Interlaken, Switzerland, 2008.

[7] W. Gille, "Chord length distribution density of an infinitely long circular hollow cylinder," Mathematical and Computer Modeling, vol. 34, pp. 423–431, 2001.

[8] O. R. N. L. A. Godfrey, Physics Integration, "Vera core physics benchmark progress problem specifications," CASL-U-2012-0131-004.

[9] M. L. WILLIAMS and M. ASGARI, "Computation of continuous energy neutron spectra with discrete ordinates transport theory," Nuclear Science and Engineering, vol. 121, p. 173, 1995.

[10] N. Sugimura and A. Yamamoto, "Resonance treatment based on ultra-fine-group spectrum calculation in the aegis code," Journal of Nuclear Science and Technology, vol. 44, p. 958, 2007.

[11] W. M. Stacey, Nuclear Reactor Physics. John Wiley & Sons, 2001.

[12] E. Wigner, E. Creutz, H. J. H, and T. Snyder, "Resonance absorption of neutrons by spheres," Journal of Applied Physics, vol. 26(3), pp. 260–270, 1955.

[13] R. Goldstein and R. Cohen, "Theory of resonance absorption of neutrons," Nuclear Science and Engineering, vol. 13, pp. 132–140, 1962.

[14] G. Bell, "Theory of effective cross sections," Los Alamos National Laboratory, 1959.

[15] M. Nikolave and V. Philippov, "Measurements of structure of total neutron cross sections," At. Energ., vol. 15, p. 493, 1963.

[16] L. B. Levitt, "Probability table method for treating unresolved neutron resonances in monte carlo calculations," Nucl. Sci. Eng., vol. 49:4, pp. 450–457, 1972.

[17] D. E. Cullen and G. C. Pomraning, "Application of the probability table method to multigroup calculations of neutron transport," Nuclear Science and Engineering, vol. 55(4), pp. 387–117, 1974.

[18] J. C. Stewart, "Non-grey radiative transfer," J. Quant. Spectrosc. Radiat. Transfer, vol. 4, pp. 723–729, 1964.

[19] D. E. Cullen and G. C. Pomraning, "The multiband method in radiative transfer calculations," Journal of Quantitative Spectroscopy and Radiative Transfer, vol. 24(2), pp. 97–117, 1980.

[20] T. Takeda, H. Fujimoto, K. Sengoku, S. Shiroya, H. Unesaki, and K. Kanda, "Application of multiband method to kuca tight-pitch lattice analysis," Journal of Nuclear Science and Technology, vol. 28(9), pp. 863–869, 1991.

[21] S. Chandrasekhar, "The radiative equilibrium of the outer layers of a star, with special reference to the blanketing effect of the reversing layer," Mon. Not. R. Astr. Soc., vol. 96, pp. 21–41, 1935.

[22] S. E. Strom and R. L. Kurucz, "A statistical procedure for computing line-blanketed model stellar atmospheres with applications to the f5 iv star procyon," J. Quant. Spectrosc. Radiat. Transfer, vol. 6, pp. 591–607, 1966.

[23] D. F. Carbon, "A comparison of the straight-mean, harmonic-mean, and multiple-picket approximations for the line opacities in cool model atmospheres," The Astrophysical Journal, vol. 187, pp. 135–145, 1974.

[24] T. Yamamoto, "Background-cross-section-dependent subgroup parameters," Journal of Nuclear Science and Technology, vol. 40 (6), pp. 370–375, 2003.

[25] S. Huang and D. Y. K. Wang, "An advanced approach to calculation of neutron resonance self-shielding," Nuclear Engineering and Design, vol. 241 (8), pp. 3051–3057, 2011.

[26] P. Ribon and J. M. Maillard, "Probability tables and gauss quadrature: Application to neutron cross-sections in the unresolved energy range," ANS Topical Meeting on Advances in reactor Physics and Safety, ANS, Saratoga Springs, New York, 1986.

[27] G. Chiba and H. Unesaki, "Improvement of moment-based probability table for resonance self-shielding calculation," Annals of Nuclear Energy, vol. 33 (13), pp. 1141–1146, 2006.

[28] A. Hebert and M. Coste, "Computing moment-based probability tables for self-shielding calculations in lattice codes," Nucl. Sci. Eng., vol. 142, pp. 245–257, 2002.

[29] N. Martin and A. Hebert, "A monte carlo lattice code with probability tables and optimized energy meshes," Nucl. Sci. Eng., vol. 167, pp. 177–195, 2011.

[30] A. V. Shilkov, "Generalized multigroup approximation and lebesgue averaging method in particle transport problems," Transport Theory and Statistical Physics, vol. 23 (6), pp. 781–814, 1994.

[31] A. A. Wray, J. Ripoll, and D. Prabhu, "Investigation of the opacity binning approach for solving the shock-generated radiation of the apollo as-501 re-entry," Tech. rep., 2006.

[32] R. MacFarlane and et. al., "The njoy nuclear data processing system," LA-9303-M(ENDF-324), 1982.

[33] N. Greene and et al., "Ampx: a modular code system for generating coupled multigroup neutron-gamma libraries from endf/b," ORNL-TM-3706?Oak Ridge National Laboratory, Oak Ridge, 1976.

[34] P. R. Graves-Morris and et al., eds., Pade approximants and their applications. Academic, 1973.

[35] D. E. Cullen, "Calculation of probability table parameters to include intermediate resonance self-shielding," UCRL-79762, Lawrence Livermore National Laboratory, 1977.

[36] J. Askew and et. al., "A general description of the lattice code wims," J. Br. Nucl. Energy. Soc., vol. 5:564, 1966.

[37] T. Takeda and Y.Kanayama, "A multiband method with resonance interference effect," Nuclear Science and Engineering,, vol. 131, pp. 401–410, 1999.

[38] M. Coste, "Absorption résonnante des noyaux lourds dans les eéseaux hétérogènes," Formalisme du module d'autoprotection d'APOLLO2, CEA-N-2746, Commissariat à l'Énergie Atomique, 1994.

[39] J. Leppänen, "Performance of woodcock delta-tracking in lattice physics applications using theserpent monte carlo reactor physics burnup calculation code," Ann. Nucl. Energy, vol. 37, pp. 715–722, 2010.

[40] J. Leppänen, "Two practical methods for unionized energy grid construction in continuous-energy monte carlo neutron transport calculation," Ann. Nucl. Energy, vol. 36, pp. 878–885, 2009.

APPENDIX A

APPENDIX TO SECTION 1

A.1 Neutron Energy Distribution

For an infinite homogenous medium where the spatial effects can be neglected, the neutron scalar flux within a differential energy interval dE for a steady state can be described as follows:

$$[\Sigma_a(E) + \Sigma_s(E)]\phi(E)dE = [\int_0^\infty dE'\Sigma_s(E' \to E)\phi(E') + \frac{\chi(E)}{k_\infty}\int_0^\infty dE'\nu\Sigma_f(E')\phi(E')]dE \tag{A.1}$$

A.1.1 Fission Source Energy Range

At very high energy range, the neutrons directly produced by fission become dominant, and the number of those direct fission neutrons are much larger than the number of those which are scattered into dE. Therefore, by neglecting the scattering source, Eq. (A.1) can be simplified as:

$$\phi^{(0)} \simeq \frac{1}{\Sigma_t(E)}\frac{\chi(E)}{k_\infty}\int_0^\infty dE'\nu\Sigma_f(E')\phi(E') = \frac{\chi(E)}{\Sigma_t(E)} \times \text{Const.} \tag{A.2}$$

The solution for scalar flux can be further improved by plugging the above term into the scattering source, which leads:

$$\begin{aligned}
\phi^{(1)} &\simeq \frac{1}{\Sigma_t(E)}[\int_0^\infty dE'\Sigma_s(E' \to E)\phi^{(0)}(E') + \chi(E) \times \text{Const.}] \\
&= \frac{1}{\Sigma_t(E)}[\int_0^\infty dE'\Sigma_s(E' \to E)\frac{\chi(E')}{\Sigma_t(E)} \times \text{Const.} + \chi(E) \times \text{Const.}] \\
&= \frac{\chi(E)}{\Sigma_t(E)} \times \text{Const.}[1 + \frac{1}{\chi(E)}\int_0^\infty dE'\Sigma_s(E' \to E)\frac{\chi(E')}{\Sigma_t(E)}]
\end{aligned} \tag{A.3}$$

Therefore, the improved neutron scalar flux has a shape of fission spectrum divided by total cross section times the summary of 1 and a correction factor. Numerical evaluation for typical compositions indicates that $\phi(E) = \chi(E)/\Sigma_t(E)$ represents the energy distribution well for energies

$E \geq 0.5$ MeV [11].

A.1.2 Slowing-Down Energy Range

For 1 eV$< E < 0.5$ MeV, there is little fission or inelastic scattering, and elastic scattering becomes the dominant reaction. Then Eq. (A.1) can be simplified as follows:

$$\Sigma_t(E)\phi(E) = \int_0^\infty dE'\Sigma_s(E' \to E)\phi(E') = \sum_j \int_E^{E/a_j} dE' \frac{\Sigma_s^j(E')\phi(E')}{E'(1-\alpha_j)} \tag{A.4}$$

where the elastic scattering transfer function is

$$\Sigma_s(E' \to E) = \begin{cases} \frac{\Sigma_s(E')}{E'(1-\alpha)}, & E \leq E' \leq \frac{E}{\alpha} \\ 0, & \text{otherwise} \end{cases} \tag{A.5}$$

Assuming $\Sigma_t(E)E\phi(E)$ is a slowly varying function of E over the scattering-in interval E to E/α_j, it leads to:

$$E'\Sigma_s^j(E')\phi(E') = E\Sigma_s^j(E)\phi(E) + \frac{d}{d\ln E}[E\Sigma_s^j(E)\phi(E)]\ln\frac{E'}{E} + ... \tag{A.6}$$

If the scattering-in interval is small, then Eq. (A.4) can be written as:

$$\begin{aligned} \Sigma_t(E)\phi(E) &= \int_0^\infty dE'\Sigma_s(E' \to E)\phi(E') \\ &\approx \sum_j \{\Sigma_s^j(E)\phi(E) + \frac{1}{E}(1 + \frac{\alpha_j \ln\alpha_j}{1-\alpha_j})\frac{d}{d\ln E}[E\Sigma_s^j(E)\phi(E)]\} \\ &= \{\Sigma_s(E)\phi(E) + \frac{d}{dE}[E\bar{\xi}(E)\Sigma_s(E)\phi(E)]\} \end{aligned} \tag{A.7}$$

where $\xi_j = 1 + \frac{\alpha_j \ln\alpha_j}{1-\alpha_j}$.

Integrating the above equation from E to arbitrary E_1, we have:

$$\phi(E) = \frac{E_1\bar{\xi}(E_1)\Sigma_s(E_1)\phi)(E_1)}{E\bar{\xi}(E)\Sigma_s(E)} \exp\left[-\int_E^{E_1} dE' \frac{\Sigma_a(E')}{E'\bar{\xi}(E')\Sigma_s(E')}\right] \tag{A.8}$$

Since for most of the slowing-down energy range, $\Sigma_a(E) \ll \Sigma_s(E)$ except at resonances, the neutron flux in the slowing down region has the form of $\phi(E) \sim \frac{1}{\xi(E)\Sigma_t(E)E}$.

A.1.3 Thermal Energy Range

In the thermal energy range $E < E_{th}$, Eq. (A.1) can be written as:

$$[\Sigma_a(E) + \Sigma_s(E)]\phi(E) = \int_0^{E_{th}} dE'\Sigma_s(E' \to E)\phi(E') + S(E), \quad E < E_{th} \tag{A.9}$$

where $S(E) = \int_{E_{th}}^{\infty} dE'\Sigma_s(E' \to E)\phi(E')$. Assuming slowing down density is zero and no absorption, an equilibrium distribution can be achieved:

$$\Sigma_s(E)\phi(E) = \int_0^{E_{th}} dE'\Sigma_s(E' \to E)\phi(E') \tag{A.10}$$

In order for the above equation to be valid, the principle of detailed balance must be achieved, which states:

$$\Sigma_s(E \to E')\phi(E) = \Sigma_s(E' \to E)\phi(E') \tag{A.11}$$

According to the principle, the Maxwell-Boltzmann distribution multiplying the neutron speed satisfies the above equation, where the Maxwell-Boltzmann distribution is:

$$M(E,T) = \frac{2\pi}{(\pi kT)^{3/2}}\sqrt{E}\exp\left(-\frac{E}{kT}\right) \tag{A.12}$$

A.2 Resonance Flux

A.2.1 Resonance Flux in a Homogeneous Material

Consider a homogeneous mixture made of a moderator and a resonance absorber, assuming the scattering cross section of the moderator is much larger than its absorption cross section and is fairly constant, we have:

$$\Sigma_t^M(E) \approx \Sigma_s^M(E) = \Sigma_p^M \tag{A.13}$$

$$\Sigma_t(E) = \Sigma_t^A(E) + \Sigma_t^M(E) \approx \Sigma_a^A(E) + \Sigma_s^A(E) + \Sigma_p^M \tag{A.14}$$

The neutron balance for slowing-down energy range containing resonances in the homogeneous mixture can be written as:

$$\Sigma_t(E)\phi(E) = \int_E^{E/\alpha_M} \frac{dE'}{E'} \frac{\Sigma_s^M \phi(E')}{1-\alpha_M} + \int_E^{E/\alpha_A} \frac{dE'}{E'} \frac{\Sigma_s^A(E')\phi(E')}{1-\alpha_A} \tag{A.15}$$

Since the scattering-in interval of the moderator is normally much larger than the practical width of the resonance, the asymptotic value of the flux is applied to the first integral.

$$\begin{aligned} \Gamma_p &\ll E_0(1-\alpha_M) \\ \phi_{\text{asy}}(E) &\cong 1/E \end{aligned} \tag{A.16}$$

Then Eq. (A.15) can be simplified as:

$$\Sigma_t(E)\phi(E) = \frac{\Sigma_s^M}{E} + \int_E^{E/\alpha_A} \frac{dE'}{E'} \frac{\Sigma_s^A(E')\phi(E')}{1-\alpha_A} \tag{A.17}$$

A.2.1.1 Narrow Resonance

If the practical width of the resonance is also small compared to the scattering-in interval of resonance absorber,

$$\begin{aligned} \Gamma_p &\ll E_0(1-\alpha_A) \\ \phi_{\text{asy}}(E) &\cong 1/E \end{aligned} \tag{A.18}$$

$$\int_E^{E/\alpha_A} \frac{dE'}{E'} \frac{\Sigma_s^A(E')\phi(E')}{1-\alpha_A} \cong \frac{\Sigma_p^A}{1-\alpha_A} \int_E^{E/\alpha_A} \frac{dE'}{E'} \frac{1}{E'} \tag{A.19}$$

it leads to:

$$\phi_{NR}(E) = \frac{1}{E} \frac{\Sigma_s^M + \Sigma_p^A}{\Sigma_t(E)} \tag{A.20}$$

A.2.1.2 Wide Resonance

If the practical width of the resonance is much larger than the scattering-in interval of the resonance absorber,

$$\begin{aligned} \Gamma_p &\gg E_0(1-\alpha_A) \\ \alpha_A &\to 1 \end{aligned} \tag{A.21}$$

$$\int_E^{E/\alpha_A} \frac{dE'}{E'} \frac{\Sigma_s^A(E')\phi(E')}{1-\alpha_A} \to\cong \Sigma_s^A(E)\phi(E) \tag{A.22}$$

it leads to:

$$\phi_{WR}(E) = \frac{1}{E} \frac{\Sigma_s^M}{[\Sigma_t(E) - \Sigma_s^A(E)]} \tag{A.23}$$

Generally speaking, the WR approximation is more applicable to the lowest-energy resonances.

A.2.2 Resonance Flux in a Heterogeneous Fuel-Moderator Lattice

Consider a heterogeneous case with fuel (F) and a moderator (M), then the neutron balance in the fuel can be described as:

$$\begin{aligned} &\Sigma_t^F(E)\phi_F(E)V_F \\ =&V_F[1-P_{F0}(E)][\int_E^{E/\alpha_f} dE' \frac{\Sigma_s^f(E')\phi_F(E)}{(1-\alpha_f)E'} + \int_E^{E/\alpha_m} dE' \frac{\Sigma_s^m(E')\phi_F(E)}{(1-\alpha_m)E'}] \\ +&V_M P_{M0}(E) \int_E^{E/\alpha_M} dE' \frac{\Sigma_s^M(E')\phi_M(E)}{(1-\alpha_M)E'} \end{aligned} \tag{A.24}$$

where m is the notation for added moderator in the fuel (e.g. the oxygen in UO_2 fuel), $P_{F0}(E)$ is the probability that neutrons in the fuel slowing down to energy E will make its next collision in the moderator, $P_{M0}(E)$ is the probability that neutron in the moderator slowing down to energy E will make its next collision in the fuel. Here, $P_{F0}(E)$ and $P_{M0}(E)$ are assumed to be uniform in the fuel and moderator, respectively.

Consider the fact that the scattering-in interval of the both moderators is much larger than the

practical width the resonance, the asymptotic form of the neutron flux can be applied in the added moderator and moderator scattering sources:

$$\begin{gathered}\Gamma_p \ll E_0(1-\alpha_M), \quad \Gamma_p \ll E_0(1-\alpha_m), \\ \phi_{\text{asy}}(E) \cong \frac{1}{E}\end{gathered} \tag{A.25}$$

then Eq. (A.24) can be written as:

$$\begin{aligned}&\Sigma_t^F(E)\phi_F(E)V_F \\ =&V_F[1-P_{F0}(E)][\int_E^{E/\alpha_f} dE' \frac{\Sigma_s^(E')\phi_F(E)}{(1-\alpha_F)E'} + \frac{\Sigma_s^m(E)}{E}] \\ +&V_M P_{M0}(E)\frac{\Sigma_s^M(E)}{E}\end{aligned} \tag{A.26}$$

According to the reciprocity theorem , we have [11]:

$$P_{F0}(E)\Sigma_t^F(E)V_F = P_{M0}\Sigma_t^M(E)V_M \tag{A.27}$$

further assuming the absorption cross section in the moderator is much smaller than the scattering cross section, it leads to:

$$\begin{aligned}&\Sigma_t^F(E)\phi_F(E) \\ =&[1-P_{F0}(E)][\int_E^{E/\alpha_f} dE' \frac{\Sigma_s^f(E')\phi_F(E)}{(1-\alpha_f)E'} + \frac{\Sigma_s^m}{E}] \\ +&P_{F0}(E)\frac{\Sigma_t^F(E)}{E}\end{aligned} \tag{A.28}$$

A.2.2.1 Narrow Resonance

If the practical width of the resonance is also small compared to the scattering-in interval of resonance absorber,

$$\begin{aligned} \Gamma_p \ll & E_0(1-\alpha_f) \\ \phi_{\text{asy}}(E) \cong & 1/E \end{aligned} \tag{A.29}$$

it leads to:

$$\phi_{NR}(E) = \frac{1}{E}\frac{P_{F0}(E)\Sigma_t^F(E) + [1-P_{F0}(E)](\Sigma_p^f + \Sigma_s^m)}{\Sigma_t^F(E)} \tag{A.30}$$

A.2.2.2 Wide Resonance

If the practical width of the resonance is much larger than the scattering-in interval of the resonance absorber,

$$\begin{aligned} \Gamma_p \gg & E_0(1-\alpha_f) \\ \alpha_f \to & 1 \end{aligned} \tag{A.31}$$

$$\int_E^{E/\alpha_f} \frac{dE'}{E'}\frac{\Sigma_s^f(E')\phi(E')}{1-\alpha_f} \to \cong \Sigma_s^f(E)\phi(E) \tag{A.32}$$

it leads to:

$$\phi_{WR}(E) = \frac{1}{E}\frac{P_{F0}(E)\Sigma_t^F + [1-P_{F0}(E)]\Sigma_s^m}{[\Sigma_t^F(E) - [1-P_{F0}(E)]\Sigma_s^f(E)]} \tag{A.33}$$

A.2.2.3 Intermediate Resonance

The intermediate resonance is suggested by comparison of the narrow and wide resonances. Applying the Wigner rational approximation [12]:

$$P_{F0} = \frac{1}{\Sigma_t \bar{l} + 1} = \frac{\Sigma_e}{\Sigma_e + \Sigma_t^F} \tag{A.34}$$

to define escape cross section Σ_e for simple convex objects, it leads to:

$$\Sigma_e = \frac{1}{\bar{l}} = \frac{1}{4V/S} \tag{A.35}$$

where $\bar{l}$ is the mean chord length, V is the volume and S is the surface area of convex objects. Then, we have:

$$\begin{aligned} \phi_{NR}^{(1)}(E) &= \frac{1}{E}\frac{\Sigma_e + \Sigma_p^f + \Sigma_s^m}{\Sigma_t^F + \Sigma_e}, \\ \phi_{WR}^{(1)}(E) &= \frac{1}{E}\frac{\Sigma_e + \Sigma_s^m}{\Sigma_a^f + \Sigma_s^m + \Sigma_e}, \\ \phi_{IR}^{(1)}(E) &= \frac{1}{E}\frac{\Sigma_e + \lambda\Sigma_p^f + \Sigma_s^m}{\Sigma_a^f + \lambda\Sigma_s^f + \Sigma_s^m + \Sigma_e}, \end{aligned} \tag{A.36}$$

where $\lambda \in (0, 1)$ is known as Goldstein-Cohen parameter [13].

Therefore, while evaluating resonance integral, it is often observed that the approximate flux has the form of $\phi(E) \sim M(E) \times f_{ss}(\Sigma_t(E))$, where $M(E)$ is energy-dependent spectral function and f_{ss} is the cross section dependent self-shielding factor while neglecting spatial difference.

A.2.2.4 Equivalence Theory

When introducing microscopic cross section, the term background cross section σ_0 is employed, for a resonant nuclide r assuming no overlap of resonances, using NR flux as an example :

- for a homogeneous system:

$$\phi_{NR}^{(1)}(E) = \frac{1}{E}\frac{\sigma_{p,r} + \sigma_0^{homo}}{\sigma_{t,r} + \sigma_0^{homo}} \tag{A.37}$$

- for a heterogeneous system:

$$\phi_{NR}^{(1)}(E) = \frac{1}{E}\frac{\sigma_{p,r} + \sigma_0^{het}}{\sigma_{t,r} + \sigma_0^{het}} \tag{A.38}$$

where

$$\sigma_0^{homo} = \sum_{k \neq r} \frac{N_k \sigma_{t,k}}{N_r} \tag{A.39}$$

$$\sigma_0^{het} = \sigma_0^{homo} + \frac{\Sigma_e}{N_r} \tag{A.40}$$

Here, the spatial self-shielding effect is represented by the escape cross section divided by the nuclide atom density, and the energetic self-shielding effect is represented by the homogeneous background cross section. It is observed that the depression of neutron flux at the resonance peak is reduced by the background cross section. The above equations shows that the neutron flux in both heterogeneous and homogeneous systems can be approximated in the same analytic form, which is the principle of the equivalence theory. Therefore, when the effective cross section are tabulated for various background cross section, the results can be used for both homogeneous and heterogeneous systems.

In Eq. (A.34), Wigner rational approximation is used for defining the escape probability in order to derive the similar analytical solution between the homogeneous and heterogeneous systems. Here, we listed some of other available expressions of escape probability:

- Introducing Bell factor a_B [14]:

$$P_{F0}(E) = \frac{a_B}{\Sigma_t^F(E)\bar{l} + a_B} = \frac{a_B \Sigma_e}{\Sigma_t^F(E) + a_B \Sigma_e} \tag{A.41}$$

  where $a_B = 2\frac{(\bar{l})^2}{l^2}$.

- N-Terms Rational Approximations:

$$P_{F0} = \sum_{n=1}^{N} \frac{b_n a_n}{\Sigma_t^F(E)\bar{l} + a_n} \tag{A.42}$$

  where $\sum_{n=1}^{N} b_n = 1$ and $\sum_{n=1}^{N} b_n a_n = 1$

A.3 History of Multiband Theory

The probability table is the notation for describing the cross section functions by sets of discrete values. The idea was first briefly stated in 1963 [15], and named as subgroup method. In 1972, Levitt independently proposed his probability table method for treating the resonance self-shielding in the unresolved resonance region in Monto Carlo calculations [16]. And later, Cullen combined Nikolaev's and Levitt's probability table method and Goldstine's work on IR approximation in order to develop the multiband method for neutron transport in 1974[17]. The notation "probability table" is focused on establishing the tables and their probability, the names "subgroup method" and "multiband method" are focused on the application of these tables to neutronic calculations. Many authors have contributed to the development and evolution of MB methods[4, 18–31].

A.3.1 Derivation of Probability Table

In energy range (E_g, E_{g-1}), the cross section σ is divided into N internals. A simple example is given in Fig. A.1. One thing is noticed from the figure is that defined probability table is not sensitive to the permutation of resonances.

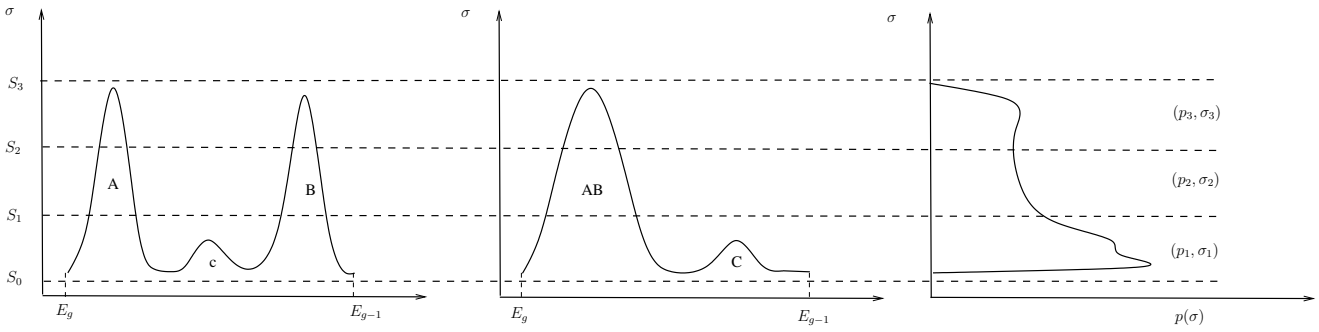

Figure A.1: Examples of probability tables

There is (p_i, σ_i) associated for each interval i:

$$p_i = \frac{\int_{E_g}^{E_{g-1}} \delta(\sigma(E), i) dE}{E_{g-1} - E_g} \tag{A.43}$$

where

$$\delta(\sigma(E), i) = \begin{cases} 1, & \text{if } S_{i-1} \leq \sigma(E) \leq S_i \\ 0, & \text{otherwise}\,. \end{cases} \tag{A.44}$$

There are different ways to define (p_i, σ_i). Soviets originally used the least square method to calculate (p_i, σ_i) [26]. The original multiband method used equal band weights. Cullen and Pomraning later concluded that it's a moment problem, where (p_i, σ_i) is defined by equating $2N$ moments of $\sigma(E)$ distribution to the same $2N$ moments of (p_i, σ_i) from I to $I + 2N - 1$:

$$m_n \equiv \frac{1}{\Delta E_g} \int_{\Delta E_g} \sigma^n(E) dE = \sum_{i=1} p_i \sigma_i^n \equiv M_n \tag{A.45}$$

where a Riemann integral can be written as a Lebesgue integral:

$$m_n \equiv \int_\sigma \sigma^n p(\sigma) d\sigma \tag{A.46}$$

The above equations are further solved by padé approximation[26]. Other possible method is the Tchebichev integration formula [26]. The simple way to solve the partial cross section x_i is:

$$I = \int x f(\sigma_t) dE = \sum_i f(\sigma_{t,i}) \sum_j w_{ij} x_j = \sum_i f(\sigma_{t,i}) x_i \tag{A.47}$$

Then only a single value x_i associated with $\sigma_{t,i}$ is required. The discrete value x_i is defined by equalizing N moments implying the partial cross section:

$$\frac{1}{\Delta E} \int_{\Delta E} x \sigma_t^n dE = \sum_i p_i x_i \sigma_{t,i}^n \tag{A.48}$$

A.3.2 Calculation of Multiband Parameters

$$\frac{1}{v_{gb}}\frac{\partial\psi_{gb}}{\partial t}+\boldsymbol{\Omega}\cdot\overrightarrow{\nabla}\psi_{gb}+\Sigma_{t,gb}\psi_{gb}=\frac{1}{4\pi}\sum_{g'=1}^{G}\sum_{b'=1}^{B}[\Sigma_{s,g'b'\rightarrow gb}\phi_{g'b'}]+\frac{\chi_{gb}}{4\pi}\sum_{g'=1}^{G}\sum_{b'=1}^{B}[\nu\Sigma_{f,g'b'}\phi_{g'b'}]+q_{gb}\,, \tag{A.49}$$

$$\psi_{gb}=\int_{\Sigma_{t,g,b-1}}^{\Sigma_{t,g,b}}d\Sigma_t^*\int_{E_g}^{E_{g-1}}\psi(t,\boldsymbol{r},\boldsymbol{\Omega},E)\delta_{gb}[\Sigma_t(E)-\Sigma_t^*]dE\,, \tag{A.50a}$$

$$\phi_{gb}=\int_{\Sigma_{t,g,b-1}}^{\Sigma_{t,g,b}}d\Sigma_t^*\int_{E_g}^{E_{g-1}}\phi(t,\boldsymbol{r},E)\delta_{gb}[\Sigma_t(E)-\Sigma_t^*]dE\,, \tag{A.50b}$$

$$\frac{1}{v_{gb}}=\frac{\int_{\Sigma_{t,g,b-1}}^{\Sigma_{t,g,b}}d\Sigma_t^*\int_{E_g}^{E_{g-1}}\frac{1}{v}\psi(t,\boldsymbol{r},\boldsymbol{\Omega},E)\delta_{gb}[\Sigma_t(E)-\Sigma_t^*]dE}{\int_{\Sigma_{t,g,b-1}}^{\Sigma_{t,g,b}}d\Sigma_t^*\int_{E_g}^{E_{g-1}}\psi(t,\boldsymbol{r},\boldsymbol{\Omega},E)\delta_{gb}[\Sigma_t(E)-\Sigma_t^*]dE}\,, \tag{A.50c}$$

$$\Sigma_{t,gb}=\frac{\int_{\Sigma_{t,g,b-1}}^{\Sigma_{t,g,b}}d\Sigma_t^*\int_{E_g}^{E_{g-1}}\Sigma_t(\boldsymbol{r},E)\psi(t,\boldsymbol{r},\boldsymbol{\Omega},E)\delta_{gb}[\Sigma_t(E)-\Sigma_t^*]dE}{\int_{\Sigma_{t,g,b-1}}^{\Sigma_{t,g,b}}d\Sigma_t^*\int_{E_g}^{E_{g-1}}\psi(t,\boldsymbol{r},\boldsymbol{\Omega},E)\delta_{gb}[\Sigma_t(E)-\Sigma_t^*]dE}\,, \tag{A.50d}$$

$$\Sigma_{s,g'b'\rightarrow gb}=\frac{\int_{\Sigma_{t,g,b-1}}^{\Sigma_{t,g,b}}d\Sigma_t^*\int_{\Sigma_{t,g',b'-1}}^{\Sigma_{t,g',b'}}d\Sigma_t^{*'}\int_{E_g}^{E_{g-1}}\int_{E_{g'}}^{E_{g'-1}}\Sigma_s(\boldsymbol{r},E'\rightarrow E)\phi(t,\boldsymbol{r},E')\delta_{gb}\delta_{g'b'}dE'dE}{\int_{\Sigma_{t,g',b'-1}}^{\Sigma_{t,g',b'}}d\Sigma_t^{*'}\int_{E_{g'}}^{E_{g'-1}}\phi(t,\boldsymbol{r},E')\delta_{g'b'}dE'}\,, \tag{A.50e}$$

$$\chi_{gb}=\int_{\Sigma_{t,g,b-1}}^{\Sigma_{t,g,b}}d\Sigma_t^*\int_{E_g}^{E_{g-1}}\chi(E)\delta_{gb}[\Sigma_t(E)-\Sigma_t^*]dE\,, \tag{A.50f}$$

$$\nu\Sigma_{f,g'b'}=\frac{\int_{\Sigma_{t,g',b'-1}}^{\Sigma_{t,g',b'}}d\Sigma_t^{*'}\int_{E_{g'}}^{E_{g'-1}}\nu\Sigma_f(\boldsymbol{r},E')\phi(t,\boldsymbol{r},E')\delta_{g'b'}[\Sigma_t(E')-\Sigma_t^{*'}]dE'}{\int_{\Sigma_{t,g',b'-1}}^{\Sigma_{t,g',b'}}d\Sigma_t^{*'}\int_{E_{g'}}^{E_{g'-1}}\phi(t,\boldsymbol{r},E')\delta_{g'b'}[\Sigma_t(E')-\Sigma_t^{*'}]dE'}\,, \tag{A.50g}$$

$$q_{gb}=\int_{\Sigma_{t,g,b-1}}^{\Sigma_{t,g,b}}d\Sigma_t^*\int_{E_g}^{E_{g-1}}q(t,\boldsymbol{r},\boldsymbol{\Omega},E)\delta_{gb}[\Sigma_t(E)-\Sigma_t^*]dE\,. \tag{A.50h}$$

It is also proved that the MB parameters in Eq. (A.50) can be derived from the existing group's self-shielded data [32,33]. A normal MG cross section for reaction R in group g, using approximate flux derived from resonance approximation $\phi(E)\sim M(E)f_{ss}(\Sigma_t(E))$ (see Appendix 1), can be

derived as:

$$\begin{aligned}\Sigma_{R,g} &= \frac{\int_{E_g}^{E_{g-1}} \Sigma_R(E)\phi(E)dE}{\int_{E_g}^{E_{g-1}} \phi(E)dE} \\ &= \frac{\int_{E_g}^{E_{g-1}} \Sigma_R(E)M(E)f_{ss}(\Sigma_t(E))dE}{\int_{E_g}^{E_{g-1}} M(E)f_{ss}(\Sigma_t(E))dE} \\ &= \frac{\int_{E_g}^{E_{g-1}} \sum_{b=1}^{B} \int_{\Sigma_{t,g,b-1}}^{\Sigma_{t,g,b}} d\Sigma_t^* \Sigma_R(E)M(E)f_{ss}(\Sigma_t^*(E))\delta_{gb}[\Sigma_t^* - \Sigma_t]dE}{\int_{E_g}^{E_{g-1}} \sum_{b=1}^{B} \int_{\Sigma_{t,g,b-1}}^{\Sigma_{t,g,b}} d\Sigma_t^* M(E)f_{ss}(\Sigma_t^*(E))\delta_{gb}[\Sigma_t^* - \Sigma_t]dE}\,.\end{aligned} \tag{A.51}$$

Defining:

$$p_{gb}(\Sigma_t^*) = \frac{\int_{E_g}^{E_{g-1}} M(E)\delta_{gb}[\Sigma_t^* - \Sigma_t]dE}{\int_{E_g}^{E_{g-1}} M(E)dE}\,, \tag{A.52}$$

$$\Sigma_{R,gb}(\Sigma_t^*) = \frac{\int_{E_g}^{E_{g-1}} \Sigma_R(E)M(E)\delta_{gb}[\Sigma_t^* - \Sigma_t]dE}{\int_{E_g}^{E_{g-1}} M(E)\delta_{gb}[\Sigma_t^* - \Sigma_t]dE}\,, \tag{A.53}$$

and integratiing Eq. (A.51) over energy first, it leads to:

$$\Sigma_{R,g} = \frac{\sum_{b=1}^{B} \int_{\Sigma_{t,g,b-1}}^{\Sigma_{t,g,b}} d\Sigma_t^* \Sigma_{R,gb}(\Sigma_t^*)f_{ss}(\Sigma_t^*)p_{gb}(\Sigma_t^*)}{\sum_{b=1}^{B} \int_{\Sigma_{t,g,b-1}}^{\Sigma_{t,g,b}} d\Sigma_t^* f_{ss}(\Sigma_t^*)p_{gb}(\Sigma_t^*)}\,. \tag{A.54}$$

Therefore, the Riemann integral over energy in can be transformed into the Lebesque integral over total cross section. It is observed that Eq. (A.52) is the definition of total cross section probability density and $p(\Sigma_t^*)d\Sigma_t^*$ is the probability of the total cross section with $d\Sigma_t^*$ with energy interval $[E_g, E_{g-1}]$, satisfying:

$$\sum_{b=1}^{B} \int_{\Sigma_{t,g,b-1}}^{\Sigma_{t,g,b}} p_{gb}(\Sigma_t^*)d\Sigma_t^* = 1 \tag{A.55}$$

Further simplifying Eq. (A.54) from a practical computational view leads to:

$$\Sigma_{R,g} = \frac{\sum_{b=1}^{B} \Sigma_{R,gb} f_{ss}(\Sigma_{t,gb}^*)P_{gb}}{\sum_{b=1}^{B} f_{ss}(\Sigma_{t,gb}^*)P_{gb}}\,, \tag{A.56}$$

where

$$P_{gb} = \int_{\Sigma_{t,g,b-1}}^{\Sigma_{t,g,b}} p_{gb}(\Sigma_t^*) d\Sigma_t^* \tag{A.57}$$

is the band weight for band b. Since $\Sigma_R(\Sigma_t^*)$ is much smoother than $\Sigma_R(E)$ over the resonance energy range, using a quadrature approximation rather than the actual integral is feasible and can be accurate.

Both MG and MB methods are aimed to preserve reaction rates. While MG method attempts to approximate the Riemann form of the integral over energy of cross section multiplied by flux moments, MB method attempts to approximate the Lebesgue form of the integrals. By using resonance approximation of the flux, MB method transforms integrals of a flux-response quantity over energy into integrals over cross section space. Then instead of MG method resolving many thin resonances in energy space, MB resolves a slowing varying function in cross section space, which reduces the number of unknowns.

Using the idea from probability table, moment methods is applied to calculate the multiband parameters (Σ_{Rb}, P_b) as described in Eq. (A.56) and Eq. (A.57), respectively. Defining a generalized self-shielding factor is of the form:

$$f_{ss}(E) = \frac{1}{[\Sigma_t(E) + \Sigma_0]^n} \tag{A.58}$$

the multiband parameters can be calculated for various n and Σ_0. Generally,

- $n = 0$ represents the unshielded flux for weighting,
- $n = 1$ represents the totally self-shielded flux for weighting,
- $n = 2$ represents the totally self-shielded current for weighting.

Consider a simple case with two bands, the multiband parameters are $(P_b, \Sigma_{t,gb})$ for $b = 1, 2$. Giving the restriction $\Sigma_{t,g1} < \Sigma_{t,g2}$ for uniqueness of the solution, the following relationships are

obtained for various n:

$$\begin{aligned}
\Sigma_{t,g}^{0} &= \frac{\Sigma_{t,g1}P_1 + \Sigma_{t,g2}P_2}{P_1 + P2}, n = 0 \\
\Sigma_{t,g}^{1} &= \frac{P_1 + P_2}{\frac{P_1}{\Sigma_{t,g1}} + \frac{P2}{\Sigma_{t,g2}}}, n = 1 \\
\Sigma_{t,g}^{2} &= \frac{\frac{P_1}{\Sigma_{t,g1}} + \frac{P2}{\Sigma_{t,g2}}}{\frac{P_1}{\Sigma_{t,g1}^2} + \frac{P2}{\Sigma_{t,g2}^2}}, n = 2
\end{aligned} \tag{A.59}$$

After algebraic manipulation, the solutions are :

$$P_{1/2} = \frac{1}{2} \pm \delta, \ .\Sigma_{t,1/2} = \frac{1}{A \pm B} \tag{A.60}$$

where

$$\begin{aligned}
\delta &= \frac{1 - A(\Sigma_{t,g}^{1})}{2B\Sigma_{t,g}^{1}} \\
A &= \frac{1}{2\Sigma_{t,g}^{2}} \frac{\Sigma_{t,g}^{0} - \Sigma_{t,g}^{2}}{\Sigma_{t,g}^{0} - \Sigma_{t,g}^{1}} \\
B^2 &= \frac{1}{\Sigma_{t,g}^{0}\Sigma_{t,g}^{1}}[1 - 2A\Sigma_{t,g}^{1} + \Sigma_{t,g}^{0}\Sigma_{t,g}^{1}A^2]
\end{aligned} \tag{A.61}$$

Once $(P_b, \Sigma_{t,gb})$ for $b = 1, 2$ are known, it can be applied to solve for any reaction $\Sigma_{R,gb}$. The same procedure can be applied for N bands $(P_b, \Sigma_{R,gb})$ for $b = 1, ..., N$. Giving $2N$ sets of self-shielded cross section, $(P_b, \Sigma_{t,gb})$ are solved from Eq. (A.56) and Eq. (A.57). Then $\Sigma_{R,gb}$ for $b = 1, ..., N$ can be further solved form linear system of Eq. (A.56) for various reaction type. For $\Sigma_0 = 0$ and different value of N , it is the Hausdroff moments problem [34], while for $N = 1$, and different values of Σ_0, it is the Stieltjes-Hilbert moments problem[34].

In a normal MG method, the scattering cross section from an initial group g' to final group g only depends on the scattering cross section g' and the transfer matrix:

$$\Sigma_{s,g' \to g} = \Sigma_{s,g'} T_{g' \to g} \tag{A.62}$$

where $T_{g' \to g}$ is independent of the cross section in either group g' and group g. For MB method, various definition of the scattering transfer have been studied:

- The NR approximation, which assumes there is no correlation between the initial and final scattering cross section, defines that the neutrons scattered into band gb only depends on the weight of each band in group g:

$$\Sigma_{s,g'b' \to g} = \Sigma_{s,g'b'} T_{g' \to g} \tag{A.63}$$

  Then,

$$\Sigma_{s,g'b' \to gb} = P_b \Sigma_{s,g'b'} T_{g' \to g} = P_b \Sigma_{s,g'b' \to g}. \tag{A.64}$$

- The WR approximation assumes there is no slowing-down due to the absorber, which indicates the scattered neutron will stay in the same group.

$$\Sigma_{s,g'b' \to gb} = \Sigma_{s,g'b'} \delta_{b'b} \delta_{g'g} \tag{A.65}$$

  In this case, there is correlation between the initial and final cross sections.

- The IR approximation is a linear combination of NR and WR approximation, which suggests[35]

$$\Sigma_{s,g'b' \to gb} = [\lambda P_b + (1 - \lambda)\delta_{b'b}] \Sigma_{s,g'b'} T_{g' \to g}. \tag{A.66}$$

  where λ is a group-averaged value, and also available in MG libraries[32, 36]. Therefore, the MB weights and cross section can be derived from the existing self-sheilded MG libraries.

A.3.3 Correlations in Multiband Method

There are several problems arising for MB method when it comes to a practical calculation: the overlapping of the resonances from different resonant nuclides in the same material (also called the resonance interference effect) , the space-dependent mixture of resonant nuclides, and the same

resonant nuclides at different temperatures. Various methods have been proposed to solve those issues. Takeda et. al. introduced the conditional probability that a nuclide takes a certain band under the condition that the other nuclide takes another band [37]. Ribon and Hebert used a correlated weight matrix to represent this effect for the elastic slow-down scattering at low energy[4, 26], which is briefly explained here. In lethargy space, the elastic slowing-down scattering for a single resonant nuclide can described as:

$$\begin{aligned}\frac{1}{(1-\alpha)\Delta u_g}\int_{u_{g-1}}^{u_g} du \int_{u-\epsilon}^{u} du' e^{u'-u} f[\sigma(u)]g[\sigma(u')] &= \int_0^{max(\sigma)} d\sigma \int_0^{max(\sigma)} d\sigma' \Pi_s(\sigma,\sigma') f(\sigma) g(\sigma') \\ &= \sum_{k=1}^{K}\sum_{l=1}^{K} W_{k,l} f(\sigma_k) g(\sigma_l)\end{aligned} \tag{A.67}$$

where $\alpha = (\frac{A-1}{A+1})^2$, $\epsilon = \ln \frac{1}{\alpha}$, $\Pi_s(\sigma,\sigma')$ is the conditional probability density, $f(\sigma)$ and $g(\sigma)$ are arbitrary functions of the total cross section, $W_{k,l}$ is the slowing-down weight matrix, expected to be normalized as:

$$\sum_{k=1}^{K} W_{k,l} = W_l, \quad \sum_{l=1}^{K} W_{k,l} = W_k \tag{A.68}$$

The above normalization can not be achieved simultaneously, since the integral range of $(u-\epsilon, u)$ indicates that the initial energy value u' may be in group $g-1$ while quadrature points σ_k and σ_l are only defined in group g. For a pair of resonant nuclides a and b with K and L order of the probability tables, respectively , it has:

$$\begin{aligned}\frac{1}{\Delta u_g}\int_{u_{g-1}}^{u_g} du f[\sigma^a(u), \sigma^b(u)] &= \int_0^{\max(\sigma^a)} d\sigma^a \int_0^{\max(\sigma^b)} d\sigma^b \Pi(\sigma^a,\sigma^b) f(\sigma^a,\sigma^b) \\ &= \sum_{k=1}^{K}\sum_{l=1}^{L} w_{k,l}^{ab} f(\sigma_k^a, \sigma_l^b)\end{aligned} \tag{A.69}$$

where the conditional probability is defined as:

$$\Pi(\sigma^a, \sigma^b) = \sum_{k=1}^{K} \sum_{l=1}^{L} \delta(\sigma^a - \sigma_k^a)\delta(\sigma^b - \sigma_l^b) w_{k,l}^{ab} \tag{A.70}$$

Then, the moment problem for two correlated nuclides is: :

$$M_{m,n} = \frac{1}{\Delta u_g} \int_{u_{g-1}}^{u_g} du \sigma^a(u)^m \sigma^b(u)^m = \sum_{k=1}^{K} \sum_{l=1}^{L} w_{k,l}^{ab} (\sigma_k^a)^m (\sigma_l^b)^n \tag{A.71}$$

The correlated weight $w_{k,l}^{ab}$ can be solved by the method proposed in the reference [38]. A detailed derivation of mutual resonance shielding model including correlation can be find in the reference[4].

APPENDIX B

APPENDIX TO SECTION 2

B.1 Energy Penalty

The energy is included in the observation to bound the energy element also in energy not just flux. This is called energy penalty. The magnitude of the energy penalty determines its importance in the clustering and therefore should be balanced compared to other information in the observation. The observation of the energy penalty over selected energy range is chosen as:

$$O_{g,\text{energy}} = \beta\sqrt{N}\log_{10}[\frac{\phi_{\max}}{\phi_{\min}}]\frac{\log_{10}E_g}{\log_{10}\frac{E_{\max}}{E_{\min}}} \tag{B.1}$$

where N is the number of other observations. In this way, the magnitude of energy penalty to other observations only depends on the value of β. In the later calculation, $\beta = 0.96$ is used and energy bounding is mostly relied on coarse group structure.

When it comes to energy bounding, it is observed that using coarse group structure is more effective than using energy penalty. However, using coarse group structure requires manually carefully selecting group boundaries and an apportioning algorithm to automatically allocate the number of energy elements in each coarse group, which is described in the next section. The reason in introduce the energy penalty is to make the minimization process have the maximum freedom to chose its energy mesh.

B.2 Apportioning Algorithm

The apportioning algorithm is defined as follows:

$$y_g \equiv \frac{v_g}{v_{tot}} N_{tot} \tag{B.2a}$$

$$M_g \equiv \max(1, y_g) \tag{B.2b}$$

$$M_{tot} \equiv \sum_g M_g \tag{B.2c}$$

$$\gamma_g \equiv \frac{M_g - 1}{M_{tot} - G} \tag{B.2d}$$

$$\hat{N}_g \equiv \lfloor \gamma_g (N_{tot} - G) \rfloor + 1 \tag{B.2e}$$

$$\delta_g \equiv (\gamma_g (N_{tot} - G) + 1) - \hat{N}_g \tag{B.2f}$$

$$\Delta \equiv N_{tot} - \sum_g \hat{N}_g \tag{B.2g}$$

where v_g is the metric in coarse group g, $v_{tot} = \sum_g v_g$, and N_{tot} is the total number of discontiguous group. Define:

$$N_g = \begin{cases} \hat{N}_g & if g \in a \\ \hat{N}_g + 1 & if g \notin a \end{cases} \tag{B.3}$$

where a is a list of g related to Δ largest δ_g. There are three properties regrading the algorithm:

1. The algorithm ensures that each coarse group has at least one group, $N_g \geq 1$, which can be derived as follows:

$$M_{tot} = \sum_g \max(1, y_g) = \sum_g \max(1, \frac{v_g}{v_{tot}} N_{tot}) \geq N_{tot} \geq G \tag{B.4}$$

   It is also obvious tat $N_{tot} \geq G$, where $N_{tot} = G$ is the simplest case where no apportioning algorithm is needed as one coarse group has exactly one group.

$$Mg \geq 1 \implies \gamma_g \geq 0 \tag{B.5}$$

Therefore,

$$\begin{aligned} \lfloor \gamma_g (N_{tot} - G) \rfloor \geq 0 \\ \implies \hat{N}_g \geq 1 \\ \implies N_g \geq 1 \end{aligned} \tag{B.6}$$

2. The algorithm ensures the summation of number of discontiguous groups in each coarse group is the user defined N_{tot}.

$$\begin{aligned} &\sum_g \hat{N}_g = \lfloor \gamma_g (N_{tot} - G) \rfloor + 1 \leq \sum_g \gamma_g (N_{tot} - G) + G = N_{tot} \\ &\implies \Delta \geq 0 \end{aligned} \tag{B.7}$$

Therefore,

$$\sum_g N_g = \Delta + \sum_g \hat{N}_g = N_{tot} \tag{B.8}$$

3. The algorithm ensures that the number of discontiguous groups in each coarse group is proportional to the relative metric in that coarse group, which can be derived as:

$$N_g \simeq \frac{M_g - 1}{M_{tot} - G} (N_{tot} - G) + 1 \tag{B.9}$$

Define

$$\begin{aligned} r \equiv \frac{N_{tot} - G}{M_{tot} - G}, \quad \text{and } G \leq N_{tot} \leq M_{tot} \\ \implies 0 \leq r \leq 1 \end{aligned} \tag{B.10}$$

Then

$$N_g \simeq \frac{v_g}{v_{tot}} N_{tot} r + (1-r)1, \tag{B.11}$$

$$\frac{N_g}{N_{tot}} \simeq \frac{v_g}{v_{tot}} r + (1-r)\frac{1}{N_{tot}}, \tag{B.12}$$

$$\tag{B.13}$$

Therefore, when r is close to 1, the number of discontiguous groups in each coarse group is approximately proportional to the metrics in each coarse group; while when r is close to 0, in which there is little difference of the variance in each coarse group, the number of discontiguous groups in each coarse group is close to 1.

B.3 Generation of the Hyperfine Energy Grid

The hyperfine group structure is chose as follows:

1. Create a list of all problem relevant materials and corresponding temperatures, including actual problem material and approximate problem material may appear in the later process.

2. Derive a list of all nuclides at their corresponding temperatures.

3. Create a PENDF for each nuclide at its corresponding temperature.

4. Create a hyperfine (unionized) energy grid over all above PENDF.

5. Compute Σ_t for each material over the unionized energy grid.

6. Iteration to remove energy grid if the error calculated at this point using a linear interpolation of its neighbor points is below the tolerance for all material at its temperature. No multiple consecutive points should be removed.

7. Iteration to add midpoint if the relative difference between two neighbor points is larger than the tolerance.

8. Compute Σ_t for each material over the unionized energy grid.

9. Iteration to remove energy grid if the error calculated at this point using a linear interpolation of its neighbor points is below the tolerance for all material at its temperature. No consecutive points should be removed.

10. Iteration to add midpoint if the relative difference between two neighbor points is larger than the tolerance.

B.4 NJOY Work Flow

FEDS-NJOY and SHEM-NJOY cross sections on fine contiguous groups are processed through NJOY code, which is composed of a set of modules performing defined tasks. The workflow for generating FEDS-NJOY or MG-NJOY cross sections are displayed in Fig. B.1. Each module in NJOY has a specific processing task. RECONR reconstructs point-wise cross sections on unionized energy grid using ENDF resonance parameters and nonlinear interpolation schemes. BROADR generates Doppler-broadened cross sections at the user-defined temperatures. UNRESR generates effective self-shielded cross sections in the unresolved energy range. THERMR generates neutron scattering cross sections for free or bound scatterers at the thermal energies. GROUPR generates flux-weighted multigroup cross sections from point-wise cross sections. In GROUPR with the narrow resonance approximation, the l-th Legendre component of angular flux ϕ_l can be approximated as:

$$\phi_l = \frac{C(E)}{[\Sigma_t(E)]^{l+1}}\,, \tag{B.14}$$

where $C(E)$ is selected as mid-life pressurized water reactor spectrum consisting of thermal Maxwellian at low energies, a $1/E$ function at intermediate energies and a fission spectrum at high energies with a fusion peak added. With equivalence theory, for isotope i, the above equation can be further written as:

$$\phi_l^i = \frac{C(E)}{[\sigma_t(E)^i + \sigma_0^i]^{l+1}}\,, \tag{B.15}$$

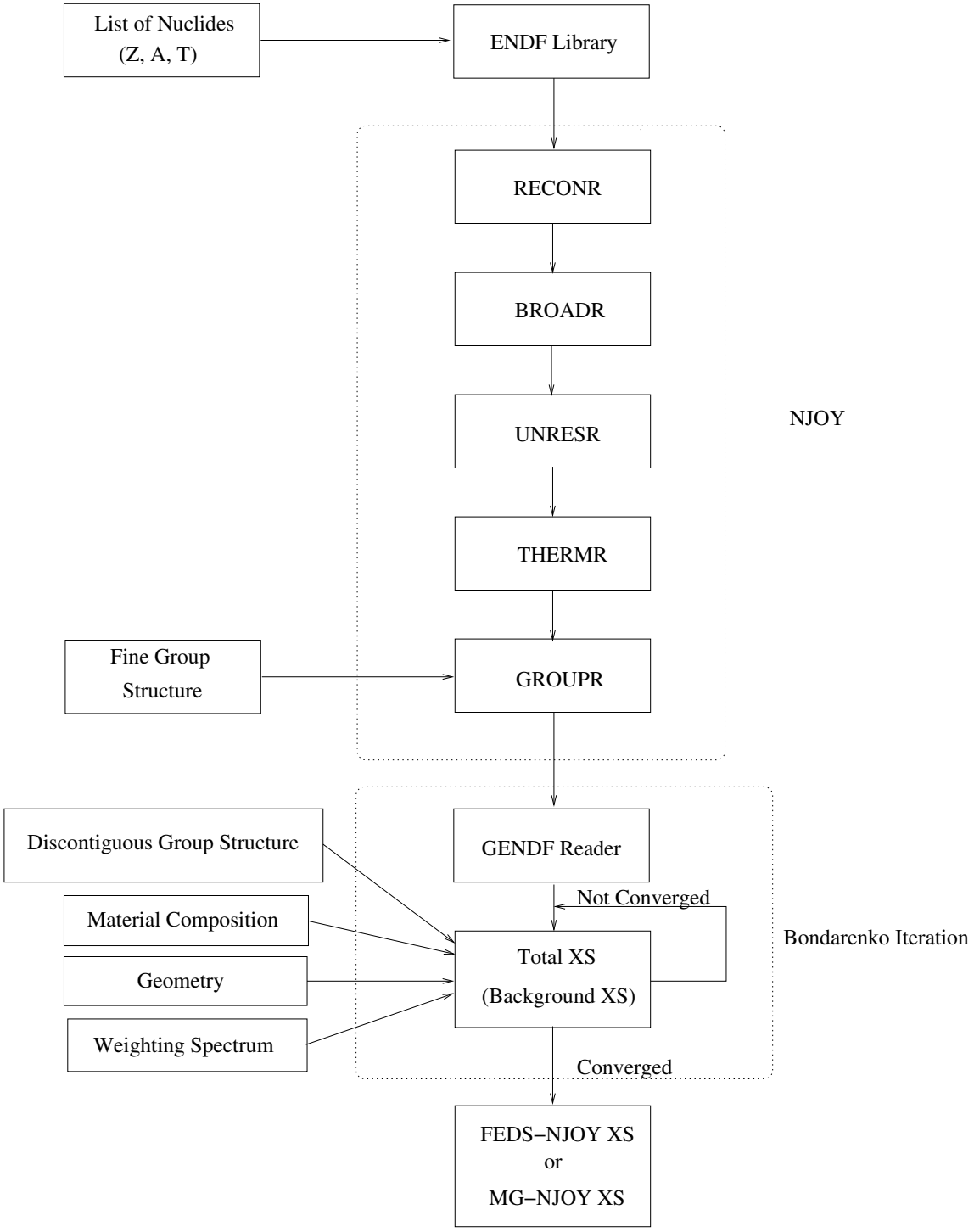

Figure B.1: Work flow for FEDS-NJOY or MG-NJOY cross sections generation

where the background cross section σ_0 represents all the effect from other nuclides in the material. For heterogeneous systems, considering the escape effects, the background cross section in material for nuclide i can be written as:

$$\sigma^i_{0,g} = \frac{1}{\rho_i}\{\Sigma_e + \sum_{j\neq i} \rho_j \sigma^j_{t,0,g}(\sigma^j_{0,g}, T)\} \tag{B.16}$$

where the escape cross section Σ_e is approximated by the average chord length. Then the total material cross sections are:

$$\Sigma_{t,l,g} = \sum_i \rho_i \sigma^i_{t,l,g}(\sigma^i_0, T) \tag{B.17}$$

where

$$\sigma^i_{t,l,g}(\sigma_0, T) = \frac{\int_g \frac{C(E)\sigma^i_t}{[\sigma_0+\sigma^i_t(E,T)]^{l+1}} dE}{\int_g \frac{C(E)}{[\sigma_0+\sigma^i_t]^{l+1}} dE}\,. \tag{B.18}$$

The output file of GROUPR is named GENDF, which contains the microscopic fine group cross sections as a function of temperature T and σ_0. The escape cross section for each material can be obtained from the geometry information. The material total cross section and the background cross section for each nuclide can be built by Eq. (B.17) through the Bondarenko iteration [32]. For standard MG group structure, each discontiguous group only contains one fine group.

APPENDIX C

APPENDIX TO SECTION 3

C.1 Results for Two and Three Coarse Groups for 2D Pin Cell Problem

We also tried to generate FEDS-NJOY cross sections with only one big coarse group for energy range $[4.21983, 22699.4]$ eV. However, due to the memory issue on NUEN cluster, we were only able to generate the FEDS-NJOY cross sections with two and three coarse groups in the above energy range. The coarse group boundaries are $[4.21983, 2.084.10, 22699.4]$ eV and $[4.21983, 51.7847, 2084.10, 22699.4]$ eV, respectively.

Table C.1: Errors in k_{eff} for 2D pin cell problem with 2 coarse groups

Method	Unknowns (RRR)	K_{eff}	E_{pcm}	Efficiency $\frac{1}{\lvert\text{Error}\rvert \times \text{DOF}}$
NJOY-FEDS-166	30	1.46726	-178 $\pm$1	18.7
NJOY-FEDS-195	59	1.46644	-122 $\pm$1	13.9
NJOY-FEDS-244	108	1.46618	-105 $\pm$1	8.8
NJOY-FEDS-361	225	1.46565	-69 $\pm$1	6.5
NJOY-FEDS-417	281	1.46509	-30 $\pm$1	11.7

Table C.2: Errors in k_{eff} for 2D pin cell problem with 3 coarse groups

Method	Unknowns (RRR)	K_{eff}	E_{pcm}	Efficiency $\frac{1}{\lvert Error \rvert \times DOF}$
NJOY-FEDS-166	30	1.47043	-395 $\pm$1	8.4
NJOY-FEDS-195	59	1.46694	-156 $\pm$1	10.8
NJOY-FEDS-244	108	1.46615	-102 $\pm$1	9.0
NJOY-FEDS-361	225	1.46545	-55 $\pm$1	8.1
NJOY-FEDS-417	281	1.46545	-55 $\pm$1	6.5

It is observed that with fewer coarse groups, there is an improvement in accuracy of results in k_{eff}.

C.2 Comparisons of MCNP and SERPENT Tally Values

Both MCNP and SERPENT are Monte Carlo codes. MCNP is widely used for neutron, photon, and electron transport simulation. SERPENT is mainly for lattice reactor physics burn up calculation. SERPENT uses woodcock delta-tracking method [39] and a single unionized energy grid for all reaction cross sections [40], to optimize the performance at a cost of memory usage. When computing the QoIs in k-eigenvalue problems, the MCNP results are used as references[1,25]. For each SERPENT run, we always check and make sure that the difference in k_{eff} between MCNP and SERPENT results is below two standard deviations. Here, we also include a section for the comparison of coarse group absorption rates in the whole fuel.The results from MCNP and SERPENT are consistent. In the calculation results section, MCNP results are used as references for two reasons: SERPENT doesn't have the direct tally functions as MCNP does.

Table C.3: Comparison of fuel absorption rate from MCNP and SERPENT for 12 Coarse group for 2D pin cell

Upper energy (eV)	SERPENT	MCNP	Relative Error
6.24999×10^{-1}	1.3119E+00 $\pm$ 6.70E-05	1.3119E+00 $\pm$ 1E-04	3.27E-05
4.21983×10^{0}	6.3675E-02 $\pm$ 1.97E-04	6.3666E-02 $\pm$ 1E-04	1.28E-04
9.50002×10^{0}	1.1513E-01 $\pm$ 3.60E-04	1.1515E-01 $\pm$ 2E-04	-1.80E-04
2.78852×10^{1}	9.3427E-02 $\pm$ 3.40E-04	9.3426E-02 $\pm$ 2E-04	4.93E-06
5.17847×10^{1}	6.2150E-02 $\pm$ 4.00E-04	6.2166E-02 $\pm$ 2E-04	-2.60E-04
1.54176×10^{2}	6.9574E-02 $\pm$ 3.10E-04	6.9591E-02 $\pm$ 2E-04	-2.43E-04
5.39204×10^{2}	5.3979E-02 $\pm$ 3.00E-04	5.3974E-02 $\pm$ 2E-04	8.96E-05
2.08410×10^{3}	3.9441E-02 $\pm$ 2.80E-04	3.9447E-02 $\pm$ 2E-04	-1.57E-04
9.11881×10^{3}	2.8120E-02 $\pm$ 2.40E-04	2.8114E-02 $\pm$ 2E-04	1.91E-04
2.26994×10^{4}	1.2877E-02 $\pm$ 2.50E-04	1.2877E-02 $\pm$ 1E-04	-2.41E-05
1.40000×10^{5}	1.8064E-02 $\pm$ 1.30E-04	1.8064E-02 $\pm$ 1E-04	-1.18E-06
2.00000×10^{7}	9.2920E-02 $\pm$ 1.03E-04	9.2915E-02 $\pm$ 1E-04	5.58E-05

C.3 Results for an Infinite Medium Problem

Significant errors are observed in results for 4 rings in fuel using NJOY-SHEM cross sections. This may be mainly caused by that the approximate weighting spectrum in NJOY code doesn't work for the multiple fuel rings case. In order to exclude the possibility of code bug, we further test the case for infinite homogeneous medium problem. The material has the same composition as the fuel material in CASL1E problem. The errors in k_{eff} for infinite medium problem is listed in Table C.4.

Table C.4: Errors in k_{eff} for NJOY-SHEM cross sections for an infinite medium problem

Method	Unknowns (RRR)	K_{eff}	E_{pcm}	Efficiency $\frac{1}{\lvert Error \rvert \times DOF}$	
NJOY-SHEM-166	30		0.65361	875 $\pm$1	18
NJOY-SHEM-244	108		0.65282	753 $\pm$1	4
NJOY-SHEM-361	225		0.65256	713 $\pm$1	2